PROBING THE ROLES OF RECEPTOR STRUCTURE, DRUG-RECEPTOR INTERACTIONS, AND RECEPTOR CROSSTALK IN LIGAND-GATED ION CHANNEL FUNCTION

Thesis by

Walrati Limapichat

In Partial Fulfillment of the Requirements

For the Degree of Doctor of Philosophy

California Institute of Technology

Pasadena, California

2013

(Defended October 9th, 2012)

To my Angels,

who are always by my side

Acknowledgements

I would like to thank:

- My research advisor, Professor Dennis Dougherty, for giving me the opportunity to be part of his research group, his guidance on my projects, his support on my career, Monday lunches, and for reviewing this entire dissertation with great patience.
- My collaborator, Professor Henry Lester, for his guidance & critiques on my research, his enthusiasm, his help with my career especially during the last year, and for trusting me to work on his projects.
- My thesis committee: Professor Bob Grubbs, Professor Doug Rees, and Professor Shu-ou Shan, for their advice and support throughout the years.
- My fellow Dougherty group members, past and present, for being so supportive of my progress. I specially thank Ariel Hanek who patiently trained me at the beginning. I thank Angela Blum for her understanding (of me & my broken English), for being my loyal friend (& my translator at times), and for plenty of laughter and wonderful time. I am also grateful for the friendship with Sean (& Meg) Kedrowski, Noah (& Tracy) Duffy, and Darren (& Lib) Nakamura. I thank Ethan Van Arnam and Chris Marotta for colorful scientific discussion and Kristina McCleary Daeffler for her encouraging words toward the end.

- The Lester lab for their support and helpful discussions. I especially thank Dr. Rigo Pantoja, Dr. Chris Richards, and Dr. Julie Miwa, who have been directly involved with my research.
- Professor Sarah Lummis and Mona Alqazzaz at the University of Cambridge for their helpful scientific discussion.
- My collaborators at the Rockefeller University: Professor Rod MacKinnon, Alice Lee, and Dr. Xiao Tao for giving me the opportunity to spend time in their lab and be part of their work. It was an invaluable experience to me.
- The Shan lab: Xin Xhang, Peera Jaru-Ampornpan, Sowmya Chandrasekar, Kuang Shen, and Thang Nguyen, for allowing me to use their equipment, for scientific discussion and friendship. I specially thank Peera, whom I lived with for five years, for lively discussion over dinner on a good day or just dinner on a not-so-good day.
- The Stoltz lab: Jenn Stockdill for help with chemistry many times and for her friendship. I thank Nathan Bennett for helping me with the polarimeter.
- Dr. Scott Ross for his assistance with the peptide NMR on the Phe-Pro project.
- Dr. Mona Shahgholi for her kind help with mass spectrometry.
- Tom Dunn, Linda Syme, and Eloisa Imel, without whom, my life would be so much harder.
- Dian Buchness, Laura Howe, and Agnes Tong.
- Professor Amit Basu, my undergraduate advisor, for his advice, encouragement, and optimism. The three years that I spent in his lab really influenced the way I look at science.

- Professor Matthew Zimmt, my first organic chemistry professor at Brown, for his incomparable enthusiasm and for always believing in me.
- Friends: Caltech Thai Club (Nok, Peera, Knot, Piti, Tara, Ped, etc.), my Santa Barbara friends (Nammon, Mock, etc.), my Dance Family friends, and other salsa friends for all the good times and the good wishes.
- Mr. Alan Talampas, for making the past difficult six months more *bear*able and for reminding me every day that it is still a beautiful world.
- And more than anyone else, my mother and my father, Dr. Kreaovan and Kitikiat Limapichat, for their encouragement and for always being supportive of my dreams.

Abstract

Ligand-gated ion channels are multi-subunit transmembrane proteins that play crucial roles in synaptic transmission in the nervous system. These include the Cys-loop receptor superfamily, the ionotropic glutamate receptor (iGluR) family, and the purinergic P2X receptor family. Binding of specific neurotransmitters at the ligand-binding site triggers a series of conformational changes that ultimately leads to ion channel opening. This dissertation describes three molecular-scale functional studies on these receptors.

The first project (**Chapter 2**) describes structure-function studies of the conserved Phe-Pro motif in the Cys loop of the nicotinic acetylcholine receptor (nAChR) of the Cys-loop superfamily. Both residues were substituted with natural and unnatural amino acids. A strong interaction between the Phe and Pro residues is evident, as is a preference for aromaticity at the Phe site. Hydrophobicity is preferred at both sites. A correlation between receptor function and the *cis* bias at the proline backbone suggests a significant role for the *cis* proline conformer in receptor function.

The second project (**Chapter 3**) concerns the key binding interaction of memantine, a prescribed drug for Alzheimer's disease, on the *N*-methyl-*D*-aspartate (NMDA) receptor of the iGluR family. The data suggest that the

special property of memantine as an NMDA receptor blocker stems from the presence of the two methyl groups and a proper shape-matching to the binding site. Comparing affinities of memantine and amantadine, a structurally related drug, in response to pore mutations allows an identification of the methyl group binding pockets on the NMDA channel pore.

The final project (**Chapter 4**) involves a study of inhibitory crosstalk between two families of ion channels: α6β4-containing nAChRs and P2X receptors. When these two distinct receptors are co-expressed, their properties are modulated from their normal behavior when expressed alone. The effect is constitutive and does not require channel activation. When they are co-activated by their respective agonists, the observed current is smaller than the sum of the currents evoked by individual application of their agonists. This functional interaction between these nicotinic and purinergic receptors in dorsal root ganglion neurons is proposed to be involved in pain sensation.

Table of Contents

Chapter 1

An Introduction to Ligand-Gated Ion Channels and Summary of Dissertation Work

1.1 Synaptic Transmission

The basis of information processing in the nervous system involves both electrical and chemical signaling. Neurons function by propagation of electrical signals across their membranes, called an action potential, traveling down a neuron's axon. Each neuron connects with one- to ten-thousand (10^3–10^4) other neurons through specialized junctions, called synapses. To communicate with another neuron, the signal from the first neuron, called the pre-synaptic neuron, must move towards an axon terminal that has formed a synapse with the dendrite of the second neuron, called the post-synaptic neuron. Communication between neurons at synapses primarily involves a chemical signal — the information is encoded as small molecules called neurotransmitters. When the electrical signal in a pre-synaptic neuron reaches a synapse, the neurotransmitter is released. The binding of neurotransmitters to their specific receptors on the post-synaptic neuron causes ion channels to open. Ion conduction through the channels consequently alters the electrical potential across the membrane of the post-synaptic neuron, regenerating an electrical signal.

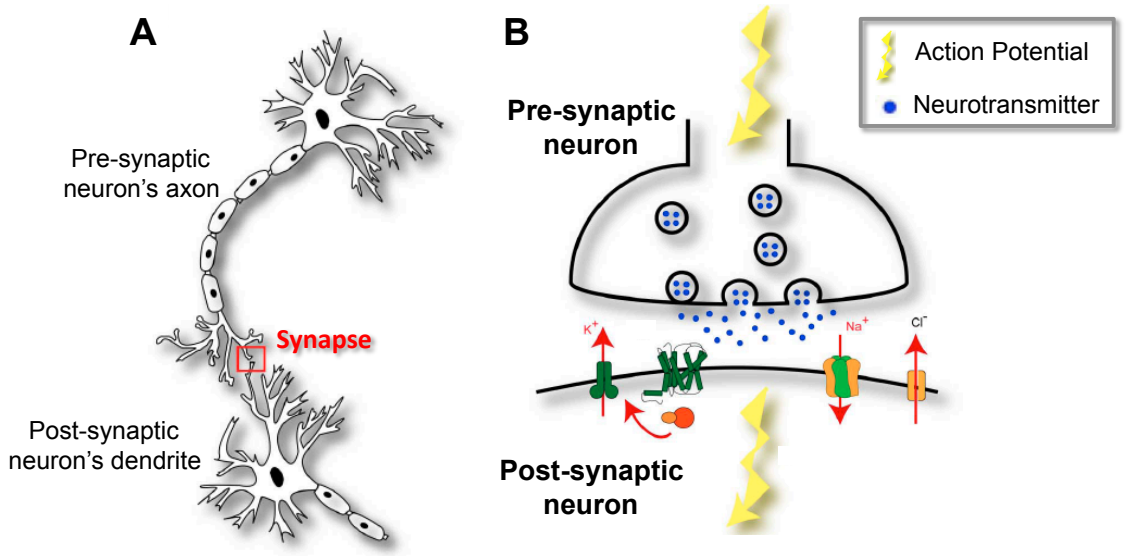

Figure 1.1. Synaptic transmission (**A)** Two neurons connect to form a synapse. **(B)** Propagation of information in the nervous system involves both electrical signal (an action potential) and chemical signal (a release of neurotransmitters)

Activated neuroreceptors either directly or indirectly produce electrical signals in the post-synaptic cell. The majority of neuroreceptors fall into two main classes, the metabotropic receptors and the ionotropic receptors. Metabotropic receptors couple to intracellular second-messenger systems through heterotrimeric G-proteins, and as such, they are known as G-Protein coupled receptors (GPCRs). In contrast, ionotropic receptors, also known as ligand-gated ion channels (LGICs), contain intrinsic pores that switch conformation from closed to open upon neurotransmitter binding, allowing ions to flow. GPCRs mediate slow synaptic transmission, acting through second-messenger pathways, whereas LGICs mediate fast synaptic transmission. In LGICs, binding of the neurotransmitter induces a conformational change in the protein that opens an ion-permeable pore that spans the cell membrane. Ion flow

upon channel opening either encourages or discourages the firing of an action potential in the post-synaptic neuron, depending on whether the LGIC is excitatory (cation selective) or inhibitory (anion selective).

1.2 Ligand-Gated Ion Channels (LGICs)

In vertebrates, the term LGICs specifically refers to three families of ionotropic receptors: Cys-loop receptors, ionotropic glutamate receptors (iGluRs), and P2X receptors (P2XRs). The Cys-loop family constitutes the largest class of LGICs. This family includes the nicotinic acetylcholine receptor (nAChR), 5-hydroxytryptamine-3 receptor (5-HT_3R), γ-aminobutyric acid receptor type A and C ($GABA_{A/C}$R), and glycine receptor (GlyR). The nAChR and 5-HT_3R are excitatory while the $GABA_{A/C}$R and GlyR are inhibitory. iGluRs are activated by the neurotransmitter glutamate, mediating most fast excitatory transmission in the central nervous system (CNS). Only in the case of NMDA receptors, glycine or *D*-serine is also required for activation. Finally, the most recently discovered ionotropic P2X receptors are activated by ATP.

All three families of LGICs are multimeric integral membrane proteins that incorporate extracellular ligand-binding sites and a transmembrane ion-permeable channel. A conformational change directly and very rapidly couples the binding of neurotransmitters to the opening of the channel, which activates within a few microseconds. The process that links neurotransmitter binding to the open conductance state of the receptor is termed "gating." The result is an

excitatory or inhibitory change in the electrical properties of the membrane, and in the case of channels that conduct Ca^{2+}, the entry of a second messenger. The structural rearrangement associated with activation of the ion channel poses important concerns in drug-receptor interactions and molecular recognition.

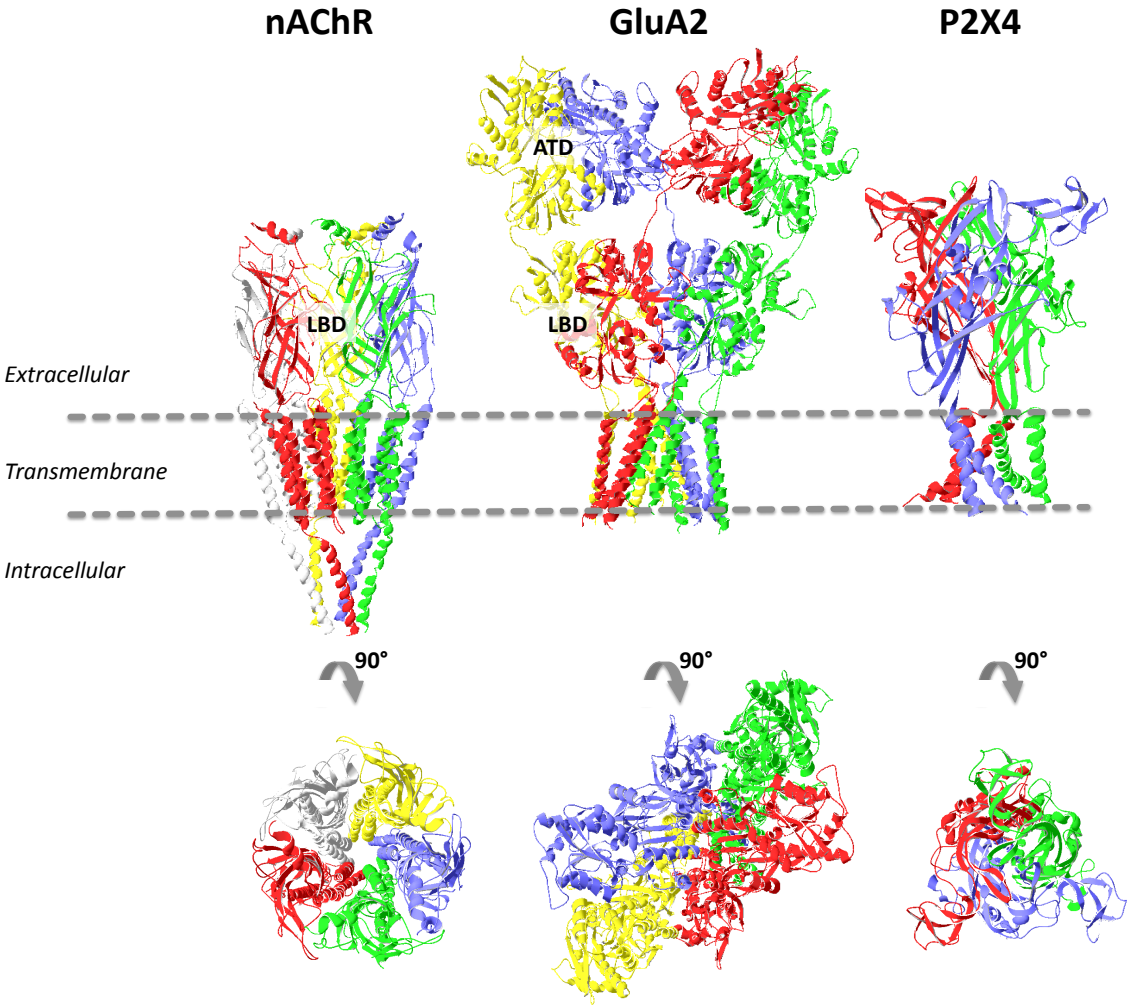

Figure 1.2. Examples of structures for the three families of LGICs: *Torpedo* nAChR (Protein Data Bank code 2BG9) for Cys-loop receptors, rat homomeric GluA2 receptor (Protein Data Bank code 3KG2) for iGluRs, and zebrafish P2X4 receptor (Protein Data Bank code 4DW0) for P2X receptors

An agonist of a receptor is a ligand that mimics the endogenous neurotransmitter by producing the same conformational change and the same biological response upon binding to the receptor. Receptors can be activated by endogenous agonists, such as neurotransmitters, or exogenous agonists, such as drugs. *Efficacy* of an agonist refers to the relative ability of the agonist-receptor complex to produce a maximum functional response. *Full agonists* bind and activate a receptor, displaying full efficacy at that receptor, while *partial agonists* also bind and activate a given receptor, but have only partial efficacy at the receptor relative to a full agonist. Receptor binding to an *antagonist* results in the inhibition of a biological response. An *antagonist* is a ligand that does not provoke a biological response itself upon binding to a receptor, but blocks or dampens agonist-mediated responses.

1.2.1 Cys-loop superfamily

The Cys-loop receptors are pentamers composed of five subunits arranged around a central ion-conducting pore (Figure 1.2, *left*). Subunits share a common structure consisting of a large, *N*-terminal extracellular domain that contains the agonist-binding site and also the signature disulfide loop, four transmembrane α-helices (M1–M4) that line the ion pore, and a short extracellular *C*-terminus. Nicotinic acetylcholine receptors (nAChRs) are the best-characterized members of the family and are therefore generally considered the prototypical Cys-loop receptor (*1*–*3*). The works described in this dissertation primarily focus on nAChRs.

The nAChRs mediate rapid synaptic transmission in the central and peripheral nervous systems (*1*, *4*, *5*). They are activated endogenously by the neurotransmitter acetylcholine. Nicotine, the active compound of tobacco, coincidentally activates these receptors. To date, seventeen nAChR subunits have been cloned: α1–α10, β1–β4, γ, δ, and ε (*3*). These subunits arrange as homo- or hetero-pentamers to form more than 20 active and pharmacologically distinct nAChR subtypes in humans. Of these subtypes, the *muscle-type* $(\alpha1)_2\beta1\gamma\delta$ is the best studied owing to its precise subunit stoichiometry.

No high-resolution structure of a nAChR exists, but a significant amount of relevant structural information is currently available. The identification and structural characterization of a family of snail acetylcholine-binding proteins (AChBPs) was the major advance in the early 2000s (*6*–*11*). The AChBPs are soluble, pentameric proteins that share 20–25% sequence identity with the extracellular ligand-binding domain of the nAChRs. Their high-resolution x-ray crystallography structures have served as structural templates for many functional studies of the residues involved in ligand binding in the nAChRs, including agonists, antagonists, and allosteric modulators. However, the AChBPs are simply soluble proteins that evolved to contain a binding site and do *not* contain an ion channel. As such, they offer little information about the activation/gating pathway of the nAChRs.

A structure of the full-length receptor at medium 4.0 Å resolution has been achieved by electron microscopy (EM) studies of the nAChR from *Torpedo* electric ray (*12*–*14*). Many amino acid side chains cannot be resolved in this cryo-

EM structure, but it does provide a general picture of the overall topology and secondary structures of a full-length protein. In 2007, a crystal structure of the extracellular domain of the nAChR α1 solved at 1.94 Å resolution was published (*15*). The glycosylation patterns are well resolved at this resolution, but the key agonist-binding Trp residue is missing from this structure.

The most recent advances in Cys-loop receptor research are the publications of x-ray crystal structures of orthologous pentameric receptors from bacteria and archaea, which belong to the same extended family as the vertebrate Cys-loop receptors called the pentameric ligand-gated ion channel (pLGIC). The x-ray structure of a prokaryotic pLGIC from the bacterium *Erwinia chrysanthemi* (ELIC) at 3.3 Å resolution in the presumed close conformation was published in 2008 (*16*). A year later in 2009, two x-ray crystal structures of a proton-gated pLGIC from the bacterial *Gloeobacter violaceus* (GLIC) appeared at 2.9 Å and 3.1 Å resolutions, and both are believed to be in the open conformation (*17*, *18*). The expression of these bacterial channels yielded functional cationic ion channels (*19*, *20*). The first structure of a eukaryotic member of pLGIC, the *anionic* glutamate receptor from *C. elegans* (GluCl), was recently solved at 3.3Å resolution (*21*).

From the available structural information, it is now well accepted that agonists bind at the interface of adjacent subunits in the nAChR pentamer (*1*, *4*, *5*). The agonist-binding site is a compact pocket comprised of amino acids from several noncontiguous regions from the *principal* (always an α subunit) and *complementary* subunits (such as the γ, δ, or ε subunits in the muscle subtype and

the β2 or β4 subunits in the neuronal nAChRs). Five conserved aromatic residues form what is known as the *aromatic binding box*; e.g., α1Y93 (loop A), α1W149 (loop B), α1Y190 (loop C), α1Y198 (loop C), and ϒW55/δW57 (loop D) of the muscle type. There are two agonist-binding sites in a receptor, and it is known that both must be occupied to optimally activate the receptor. The fifth subunit that is not involved in the binding site formation is termed the *accessory subunit*; e.g., the β1 subunit of the muscle nAChR.

The ion channel pore is lined by the M2 helix from each subunit of the pentamer. Each M2 helix contributes several highly conserved hydrophobic residues that constitute the channel gate. The leucine-9′ residue (where 9′ represents the ninth residue from the cytoplasmic end of the transmembrane helix) comprises the narrowest constriction point in the *Torpedo* cryo-EM structure and is located at the approximate midpoint of the M2 helix (*14*). This residue has been shown to play a critical role in channel gating, and when mutated to a more polar amino acid, the pore is stabilized in an open, ion-conducting conformation (*22*, *23*).

1.2.2 Glutamate-gated ion channels (iGluRs)

Tetrameric iGluRs are widely expressed in the central nervous system where they mediate fast excitatory synaptic transmission in the brain of vertebrates. Eighteen human iGluR genes were cloned, and 4 major classes of iGluRs have been identified to date. The NMDA receptors that play key roles in

synaptic plasticity are obligate heteromers formed by co-assembly of different combinations of the GluN1, GluN2A–GluN2D, GluN3A and GluN3B subunits. Their ion channels are Ca^{2+} permeable ion and are blocked by extracellular Mg^{2+}. Other subfamilies of iGluRs are not sensitive to Mg^{2+} block. GluA1–GluA4 are co-assembled to form homomeric or heteromeric AMPA receptors that mediate fast excitatory synaptic transmission at the majority of central synapses. Kainate receptors regulate neuronal excitability and are formed by co-assembly of GluK1–GluK5. GluD1 and GluD2 have not been shown to form functional channels.

The first crystal structure for a *full-length* iGluR is the structure of the GluA2 homotetramer, solved at a resolution of 3.6 Å (*24*). The crystal structure of the full-length AMPA receptor reveals that each AMPA receptor subunit is organized into four discrete regions: the amino terminal domain (ATD), the ligand-binding domain (LBD), the transmembrane ion channel pore domain (TMD), and the cytoplasmic domain (Figure 1.2, *middle*). The transmembrane segments are organized in the expected 4-fold symmetry found in voltage-gated ion channels, but with inverted topology. Each subunit has 3 membrane-spanning helices plus a pore helix. The third transmembrane helix from the four subunits forms a bundle crossing, which acts as a barrier to ion permeation and forms the lining of the pore. The extracellular domains form 85% of the mass of an iGluR core. The extracellular domains are loosely packed assemblies with two clearly distinct layers of ATDs and LBDs, each of which has both local and global 2-fold axes of symmetry. Different subunit pairs form dimer assemblies in

the ATD and LBD layers — this subunit crossover was entirely unexpected prior to the publication of this crystal structure.

In addition to the full-length structure, it is possible to express the extracellular domains of iGluRs, both ATD and LBD, as soluble proteins genetically excised form the ion channels. Several x-ray crystal structures of the ATD and LBD are currently available at high resolution. The LBD appears to have a clamshell-like shape that is formed by two domains, D1 and D2, and the ligands bind in the cleft between the two domains (*25*). Because of the difficulty of expression and crystallization of a full-length receptor, the crystal structures derived from these soluble proteins continue to provide valuable structural insights into binding of ligands, mechanism of activation, as well as allosteric modulation by drugs and endogenous ions.

1.2.3 P2X receptor family

P2X receptors are non-selective cation channels gated by extracellular ATP. They are widely expressed in many tissues and are believed to play key roles in various physiological processes such as nerve transmission, pain sensation, and the response to inflammation (*26*–*31*). There are seven P2X receptor subunits in mammals: P2X1–P2X7. They co-assemble into a homomeric or heteromeric trimer (Figure 1.2, *right*). The ATP sensitivity and functional properties of P2X receptors vary widely, including the ATP affinity, ion permeability, and desensitization kinetics (*32*).

Crystal structures of P2X receptors only became available very recently. The first publication of the x-ray crystal structure of zebrafish P2X4 in 2009 represents the greatest breakthrough (*33*). Very recently, a structure for P2X4 in the ATP-bound form was published (*34*). The structures confirm several findings from previous mutational studies. The ATP-binding site is identified to be interfacial between two subunits (*35*–*40*), and the channel gate is located at the external portion of the second transmembrane helix (*41*, *42*).

No P2X-receptor related protein has been identified in the genomes of *D. melanogaster*, *C. elegans*, yeast or prokaryotes (*43*), unlike the other two families of LGICs, which makes their evolutionary origins a mystery.

1.2.4 Crosstalk between LGICs

Fast neurotransmitters such as GABA–Glycine (*44*), ATP–GABA (*45*, *46*), and ATP–acetylcholine (*47*–*49*) are co-released during synaptic transmission. Interaction between their respective receptor channels is likely to play a critical role in shaping the synaptic responses. In fact, cross interaction between two structurally and functionally different LGICs has been demonstrated in the form of non-independent receptor function, both in cultured neurons and heterologous expression systems. Co-activation of both receptors in an interacting pair typically leads to a cross-inhibitory interaction that translates into non-additivity of the recorded currents. For example, a number of P2XR subtypes were shown to interact with members of the Cys-loop receptor family,

including nAChRs, 5-HT_3R, and $GABA_{A/C}$ receptors (*50*–*63*). Furthermore, interactions between GlyR and $GABA_A$ receptors (*64*, *65*), as well as between AMPA receptors and NMDA receptors (*66*), have been reported. Evidence supporting physical association between these receptors is also available (*52*–*54*).

1.3 Methods for Investigation of Ion Channel Function

1.3.1 Two-electrode voltage-clamp recordings on *Xenopus* oocytes

We used *Xenopus* oocytes, egg cell precursors from an African frog, for expressing and investigating the function of LGICs. These cell are very large in size, ~ 1 mm in diameter, which allows a physical injection of RNA and other materials into the cells. Upon mRNA injection, the cell synthesizes, folds, assembles, and transports the protein to the surface of the cell membrane.

When an agonist is applied to an oocyte expressing an LGIC, ion pores open, allowing current to flow across the cell membrane. Current recordings on oocytes are conducted in a whole cell two-electrode voltage-clamp mode (Figure 1.3). In this setup, one electrode measures the voltage difference across the cell membrane, and the other electrode injects current into the cell to hold it at a particular voltage, typically at −60 mV. A feedback circuit connected to the voltage electrode is used to determine the current required to maintain this potential. The current electrode must inject current equal to that passing through the open channels, and therefore, the required current is a direct measure of the sum of all ion channel gating in the cell.

Functions of wild-type and mutant LGICs are evaluated in this setup by measuring the current response to agonists or antagonists applied to the cell. Increasing concentrations of agonists induce increasing current magnitudes (up to saturation) because more ion channels are open. Increasing concentrations of antagonists produce the opposite effect. Across wild-type and mutant receptors, we use EC_{50} as a convenient metric to compare ion channel functions and IC_{50} to compare receptor sensitivity to antagonists. Agonist EC_{50} and antagonist IC_{50} are determined by fitting the dose-response data to the Hill equation, and these values are the effective concentrations at the midpoint of the dose-response curves.

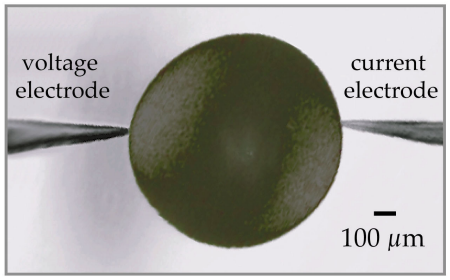

Xenopus oocyte

Figure 1.3. Current recording from a *Xenopus* oocyte on a whole-cell two-electrode voltage-clamp setup

1.3.2 Unnatural amino acid mutagenesis

Unnatural amino acids (UAAs) are synthetic amino acids that are not found in nature. Site-specific incorporation of unnatural amino acids permits systematic probing for structure-function correlations at the chemical scale. This technique offers much greater precision compared to the conventional

mutagenesis technique, which is limited by the natural twenty amino acids, because one has a rational control over the modification introduced into the protein of interest.

Several methods are available for incorporation of unnatural amino acids into proteins. In the present work, we employed the *in vivo* nonsense-suppression methodology (*67–70*). This method allows for the site-specific incorporation of a synthetic amino acid into a protein expressed in a living *Xenopus* oocyte. The procedure begins with replacing the amino acid position of interest with a non-coding codon (nonsense codon), usually a stop codon, by conventional site-directed mutagenesis (Figure 1.4). This would typically result in the premature termination of the protein's biosynthesis, but it is not the case here because we supply the translation system with a suppressor tRNA, a tRNA whose anticodon recognizes the nonsense codon. We pre-couple the suppressor tRNA with a desired unnatural amino acid enzymatically. The suppressor tRNA is designed to be orthogonal, which means it is not recognized by any of the endogenous aminoacyl-tRNA synthetases.

Once we inject both the mRNA and the tRNA-UAA into *Xenopus* oocytes, the translation then proceeds with the unnatural amino acid incorporated into the protein at the site of interest. Two different stop codons are utilized for site-specific incorporation of two unnatural amino acids into a receptor, as demonstrated in **Chapter 2** of this thesis. Alternatively, one may employ a closely related strategy for unnatural amino acid incorporation in *Xenopus*

oocytes, which is known as *frameshift suppression* (*71*, *72*). This technique utilizes a four-base codon (GGGT or CGGG) instead of a nonsense codon.

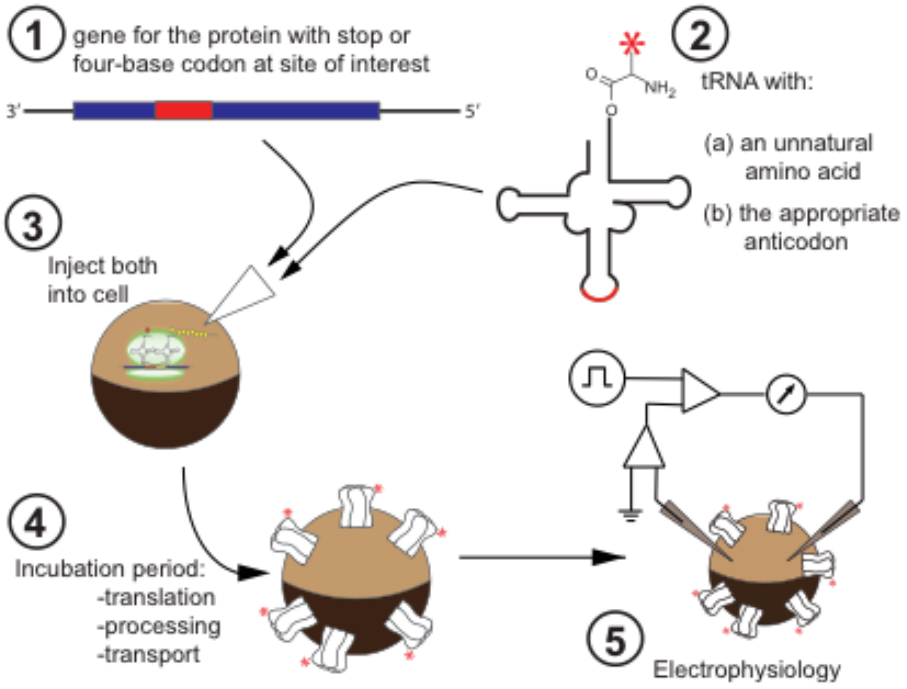

Figure 1.4. The nonsense-suppression methodology for incorporating unnatural amino acids into ligand-gated ion channels expressed in *Xenopus* oocytes

1.4 Summary of Dissertation Work

This dissertation describes three studies involving all three families of the LGICs. We demonstrated that the intrinsic receptor structures, drug-receptor interactions, and receptor-receptor crosstalk are determinants of receptor function and ion channel activities.

Chapter 2 describes a detailed structure-function investigation of the conserved Phe-Pro motif in the Cys loop of the muscle-type nAChR. This motif is universally conserved among the pentameric receptor channels. Both residues were substituted with natural and unnatural amino acids. In the receptor, a strong interaction between the Phe and Pro residues is evident, as is a strong preference for aromaticity and hydrophobicity at the Phe site. A similar influence of hydrophobicity is observed at the proline site. We also observed a correlation between receptor function and *cis* bias at the proline backbone across a simple homologous series of proline analogs, which could suggest a significant role for the *cis* proline conformer at this site in receptor function.

Chapter 3 concerns the key binding interaction of memantine, a prescribed drug for Alzheimer's disease, on the NMDA receptor. The data suggest that the special property of memantine as a potent NMDA receptor blocker stems from the presence of the two methyl groups and a proper shape-matching to the binding site. Comparing affinities of memantine and amantadine, a structurally related drug but lacking the methyl groups, in response to pore mutations enables us to identify the methyl group binding pockets for memantine on the NMDA channel pore.

Chapter 4 describes an investigation of the inhibitory crosstalk between α6β4-containing nAChRs of the Cys-loop superfamily and P2X2, P2X3, and P2X2/3 receptors. When the two distinct receptors are co-expressed in *Xenopus* oocytes, their biophysical properties are modulated from their normal behavior when expressed alone. The effect is constitutive and does not require channel

activation. When they are co-activated by their respective agonists, the observed current is smaller than the sum of the currents evoked by individual application of their agonists. Proposed molecular mechanisms for the cross interaction are also discussed.

1.5 References

(1) Corringer, P. J.; Le Novère, N.; Changeux, J. P. Nicotinic receptors at the amino acid level. *Annu. Rev. Pharmacol. Toxicol.* **2000**, *40*, 431–458.

(2) Romanelli, M. N.; Gratteri, P.; Guandalini, L.; Martini, E.; Bonaccini, C.; Gualtieri, F. Central nicotinic receptors: structure, function, ligands, and therapeutic potential. *ChemMedChem* **2007**, *2*, 746–767.

(3) Jensen, A. A.; Frølund, B.; Liljefors, T.; Krogsgaard-Larsen, P. Neuronal nicotinic acetylcholine receptors: structural revelations, target identifications, and therapeutic inspirations. *J. Med. Chem.* **2005**, *48*, 4705–4745.

(4) Grutter, T.; Changeux, J. P. Nicotinic receptors in wonderland. *Trends Biochem. Sci.* **2001**, *26*, 459–463.

(5) Karlin, A. Emerging structure of the nicotinic acetylcholine receptors. *Nat. Rev. Neurosci.* **2002**, *3*, 102–114.

(6) Brejc, K.; van Dijk, W. J.; Klaassen, R. V.; Schuurmans, M.; van Der Oost, J.; Smit, A. B.; Sixma, T. K. Crystal structure of an ACh-binding protein reveals the ligand-binding domain of nicotinic receptors. *Nature* **2001**, *411*, 269–276.

(7) Celie, P. H. N.; van Rossum-Fikkert, S. E.; van Dijk, W. J.; Brejc, K.; Smit, A. B.; Sixma, T. K. Nicotine and carbamylcholine binding to nicotinic acetylcholine receptors as studied in AChBP crystal structures. *Neuron* **2004**, *41*, 907–914.

(8) Rucktooa, P.; Smit, A. B.; Sixma, T. K. Insight in nAChR subtype selectivity from AChBP crystal structures. *Biochem. Pharmacol.* **2009**, *78*, 777–787.

(9) Hansen, S. B.; Sulzenbacher, G.; Huxford, T.; Marchot, P.; Bourne, Y.; Taylor, P. Structural characterization of agonist and antagonist-bound acetylcholine-binding protein from Aplysia californica. *J. Mol. Neurosci.* **2006**, *30*, 101–102.

(10) Hansen, S. B.; Sulzenbacher, G.; Huxford, T.; Marchot, P.; Taylor, P.; Bourne, Y. Structures of Aplysia AChBP complexes with nicotinic agonists and antagonists reveal distinctive binding interfaces and conformations. *EMBO J.* **2005**, *24*, 3635–3646.

(11) Taylor, P.; Talley, T. T.; Radic, Z.; Hansen, S. B.; Hibbs, R. E.; Shi, J. Structure-guided drug design: conferring selectivity among neuronal nicotinic receptor and acetylcholine-binding protein subtypes. *Biochem. Pharmacol.* **2007**, *74*, 1164–1171.

(12) Unwin, N. Structure and action of the nicotinic acetylcholine receptor explored by electron microscopy. *FEBS Lett.* **2003**, *555*, 91–95.

(13) Miyazawa, A.; Fujiyoshi, Y.; Unwin, N. Structure and gating mechanism of the acetylcholine receptor pore. *Nature* **2003**, *423*, 949–955.

(14) Unwin, N. Refined structure of the nicotinic acetylcholine receptor at 4Å resolution. *J. Mol. Biol.* **2005**, *346*, 967–989.

(15) Dellisanti, C. D.; Yao, Y.; Stroud, J. C.; Wang, Z.-Z.; Chen, L. Crystal structure of the extracellular domain of nAChR alpha1 bound to alpha-bungarotoxin at 1.94 Å resolution. *Nat. Neurosci.* **2007**, *10*, 953–962.

(16) Hilf, R. J. C.; Dutzler, R. X-ray structure of a prokaryotic pentameric ligand-gated ion channel. *Nature* **2008**, *452*, 375–379.

(17) Bocquet, N.; Nury, H.; Baaden, M.; Le Poupon, C.; Changeux, J.-P.; Delarue, M.; Corringer, P.-J. X-ray structure of a pentameric ligand-gated ion channel in an apparently open conformation. *Nature* **2009**, *457*, 111–114.

(18) Hilf, R. J. C.; Dutzler, R. Structure of a potentially open state of a proton-activated pentameric ligand-gated ion channel. *Nature* **2009**, *457*, 115–118.

(19) Bocquet, N.; Prado de Carvalho, L.; Cartaud, J.; Neyton, J.; Le Poupon, C.; Taly, A.; Grutter, T.; Changeux, J.-P.; Corringer, P.-J. A prokaryotic proton-gated ion channel from the nicotinic acetylcholine receptor family. *Nature* **2007**, *445*, 116–119.

(20) Zimmermann, I.; Dutzler, R. Ligand activation of the prokaryotic pentameric ligand-gated ion channel ELIC. *PLoS Biol* **2011**, *9*, e1001101.

(21) Hibbs, R. E.; Gouaux, E. Principles of activation and permeation in an anion-selective Cys-loop receptor. *Nature* **2011**, *474*, 54–60.

(22) Filatov, G. N.; White, M. M. The role of conserved leucines in the M2 domain of the acetylcholine receptor in channel gating. *Mol. Pharmacol.* **1995**, *48*, 379–384.

(23) Labarca, C.; Nowak, M. W.; Zhang, H.; Tang, L.; Deshpande, P.; Lester, H. A. Channel gating governed symmetrically by conserved leucine residues in the M2 domain of nicotinic receptors. *Nature* **1995**, *376*, 514–516.

(24) Sobolevsky, A. I.; Rosconi, M. P.; Gouaux, E. X-ray structure, symmetry and mechanism of an AMPA-subtype glutamate receptor. *Nature* **2009**, *462*, 745–756.

(25) Armstrong, N.; Sun, Y.; Chen, G. Q.; Gouaux, E. Structure of a glutamate-receptor ligand-binding core in complex with kainate. *Nature* **1998**, *395*, 913–917.

(26) Young, M. T. P2X receptors: dawn of the post-structure era. *Trends Biochem. Sci.* **2010**, *35*, 83–90.

(27) Basbaum, A. I.; Bautista, D. M.; Scherrer, G.; Julius, D. Cellular and molecular mechanisms of pain. *Cell* **2009**, *139*, 267–284.

(28) Wirkner, K.; Sperlagh, B.; Illes, P. P2X3 receptor involvement in pain states. *Mol. Neurobiol.* **2007**, *36*, 165–183.

(29) Khakh, B. S.; North, R. A. P2X receptors as cell-surface ATP sensors in health and disease. *Nature* **2006**, *442*, 527–532.

(30) Khakh, B. S. Molecular physiology of P2X receptors and ATP signalling at synapses. *Nat. Rev. Neurosci.* **2001**, *2*, 165–174.

(31) Lemoine, D.; Jiang, R.; Taly, A.; Chataigneau, T.; Specht, A.; Grutter, T. Ligand-gated ion channels: new insights into neurological disorders and ligand recognition. *Chem. Rev.* **2012**.

(32) Egan, T. M.; Samways, D. S. K.; Li, Z. Biophysics of P2X receptors. *Pflugers Arch. EJP* **2006**, *452*, 501–512.

(33) Kawate, T.; Michel, J. C.; Birdsong, W. T.; Gouaux, E. Crystal structure of the ATP-gated $P2X_4$ ion channel in the closed state. *Nature* **2009**, *460*, 592–598.

(34) Hattori, M.; Hibbs, R. E.; Gouaux, E. A fluorescence-detection size-exclusion chromatography-based thermostability assay for membrane protein precrystallization screening. *Structure* **2012**, *20*, 1293–1299.

(35) Ennion, S.; Hagan, S.; Evans, R. J. The role of positively charged amino acids in ATP recognition by human $P2X_1$ receptors. *J. Biol. Chem.* **2000**, *275*, 29361–29367.

(36) Jiang, L.-H. Identification of amino acid residues contributing to the atp-binding site of a purinergic P2X receptor. *J. Biol. Chem.* **2000**, *275*, 34190–34196.

(37) Wilkinson, W. J.; Jiang, L.-H.; Surprenant, A.; North, R. A. Role of ectodomain lysines in the subunits of the heteromeric P2X2/3 receptor. *Mol. Pharmacol.* **2006**, *70*, 1159–1163.

(38) Zemkova, H.; Yan, Z.; Liang, Z.; Jelinkova, I.; Tomić, M.; Stojilkovic, S. S. Role of aromatic and charged ectodomain residues in the $P2X_4$ receptor functions. *J. Neurochem.* **2007**, *102*, 1139–1150.

(39) Fischer, W.; Zadori, Z.; Kullnick, Y.; Gröger-Arndt, H.; Franke, H.; Wirkner, K.; Illes, P.; Mager, P. P. Conserved lysin and arginin residues in the extracellular loop of $P2X_3$ receptors are involved in agonist binding. *Eur. J. Pharmacol.* **2007**, *576*, 7–17.

(40) Roberts, J. A.; Digby, H. R.; Kara, M.; Ajouz, El, S.; Sutcliffe, M. J.; Evans, R. J. Cysteine substitution mutagenesis and the effects of methanethiosulfonate reagents at P2X2 and P2X4 receptors support a core common mode of ATP action at P2X receptors. *J. Biol. Chem.* **2008**, *283*, 20126–20136.

(41) Li, M.; Kawate, T.; Silberberg, S. D.; Swartz, K. J. Pore-opening mechanism in trimeric P2X receptor channels. *Nat. Commun.* **2010**, *1*, 44.

(42) Kracun, S.; Chaptal, V.; Abramson, J.; Khakh, B. S. Gated access to the pore of a P2X receptor: structural implications for closed-open transitions. *J. Biol. Chem.* **2010**, *285*, 10110–10121.

(43) Fountain, S. J.; Burnstock, G. An evolutionary history of P2X receptors. *Purinergic Signal.* **2009**, *5*, 269–272.

(44) Jonas, P.; Bischofberger, J.; Sandkühler, J. Corelease of two fast neurotransmitters at a central synapse. *Science* **1998**, *281*, 419–424.

(45) Jo, Y.-H.; Role, L. W. Coordinate release of ATP and GABA at in vitro synapses of lateral hypothalamic neurons. *J. Neurosci.* **2002**, *22*, 4794–4804.

(46) Jo, Y. H.; Schlichter, R. Synaptic corelease of ATP and GABA in cultured spinal neurons. *Nat. Neurosci.* **1999**, *2*, 241–245.

(47) Galligan, J. J.; Bertrand, P. P. ATP mediates fast synaptic potentials in enteric neurons. *J. Neurosci.* **1994**, *14*, 7563–7571.

(48) Redman, R. S.; Silinsky, E. M. ATP released together with acetylcholine as the mediator of neuromuscular depression at frog motor nerve endings. *J. Physiol. (London)* **1994**, *477 (Pt 1)*, 117–127.

(49) Silinsky, E. M.; Redman, R. S. Synchronous release of ATP and neurotransmitter within milliseconds of a motor nerve impulse in the frog. *J. Physiol. (London)* **1996**.

(50) Toulmé, E.; Blais, D.; Léger, C.; Landry, M.; Garret, M.; Séguéla, P.; Boué-Grabot, E. An intracellular motif of $P2X_3$ receptors is required for functional cross-talk with $GABA_A$ receptors in nociceptive DRG neurons. *J. Neurochem.* **2007**, *102*, 1357–1368.

(51) Boué-Grabot, E.; Toulmé, E.; Emerit, M. B.; Garret, M. Subunit-specific coupling between gamma-aminobutyric acid type A and P2X2 receptor channels. *J. Biol. Chem.* **2004**, *279*, 52517–52525.

(52) Boué-Grabot, E.; Emerit, M. B.; Toulmé, E.; Séguéla, P.; Garret, M. Cross-talk and co-trafficking between rho1/GABA receptors and ATP-gated channels. *J. Biol. Chem.* **2004**, *279*, 6967–6975.

(53) Boué-Grabot, E.; Barajas-López, C.; Chakfe, Y.; Blais, D.; Bélanger, D.; Emerit, M. B.; Séguéla, P. Intracellular cross talk and physical interaction between two classes of neurotransmitter-gated channels. *J. Neurosci.* **2003**, *23*, 1246–1253.

(54) Khakh, B. S.; Fisher, J. A.; Nashmi, R.; Bowser, D. N.; Lester, H. A. An angstrom scale interaction between plasma membrane ATP-gated P2X2 and alpha4beta2 nicotinic channels measured with fluorescence resonance energy transfer and total internal reflection fluorescence microscopy. *J. Neurosci.* **2005**, *25*, 6911–6920.

(55) Khakh, B.; Zhou, X.; Sydes, J.; Galligan, J.; Lester, H. State-dependent cross-inhibition between transmitter-gated cation channels. *Nature* **2000**, *406*, 405–410.

(56) Nakazawa, K. ATP-activated current and its interaction with acetylcholine-activated current in rat sympathetic neurons. *J. Neurosci.* **1994**, *14*, 740–750.

(57) Sokolova, E.; Nistri, A.; Giniatullin, R. Negative cross talk between anionic $GABA_A$ and cationic P2X ionotropic receptors of rat dorsal root ganglion neurons. *J. Neurosci.* **2001**, *21*, 4958–4968.

(58) Decker, D. A.; Galligan, J. J. Cross-inhibition between nicotinic acetylcholine receptors and P2X receptors in myenteric neurons and HEK-293 cells. *Am. J. Physiol. Gastrointest. Liver Physiol.* **2009**, *296*, G1267–76.

(59) Decker, D. A.; Galligan, J. J. Molecular mechanisms of cross-inhibition between nicotinic acetylcholine receptors and P2X receptors in myenteric neurons and HEK-293 cells. *Neurogastroenterol. Motil.* **2010**, *22*, 901–8, e235.

(60) Karanjia, R.; García-Hernández, L. M.; Miranda-Morales, M.; Somani, N.; Espinosa-Luna, R.; Montaño, L. M.; Barajas-López, C. Cross-inhibitory interactions between $GABA_A$ and P2X channels in myenteric neurones. *Eur. J. Neurosci.* **2006**, *23*, 3259–3268.

(61) Barajas-López, C.; Montaño, L. M.; Espinosa-Luna, R. Inhibitory interactions between 5-HT_3 and P2X channels in submucosal neurons. *Am. J. Physiol. Gastrointest. Liver Physiol.* **2002**, *283*, G1238–48.

(62) Barajas-López, C.; Espinosa-Luna, R.; Zhu, Y. Functional interactions between nicotinic and P2X channels in short-term cultures of guinea-pig submucosal neurons. *J. Physiol. (London)* **1998**, *513 (Pt 3)*, 671–683.

(63) Zhou, X.; Galligan, J. J. Non-additive interaction between nicotinic cholinergic and P2X purine receptors in guinea-pig enteric neurons in culture. *J. Physiol. (London)* **1998**, *513 (Pt 3)*, 685–697.

(64) Li, Y.; Wu, L.-J.; Legendre, P.; Xu, T.-L. Asymmetric cross-inhibition between $GABA_A$ and glycine receptors in rat spinal dorsal horn neurons. *J. Biol. Chem.* **2003**, *278*, 38637–38645.

(65) Li, Y.; Xu, T. L. State-dependent cross-inhibition between anionic $GABA_A$ and glycine ionotropic receptors in rat hippocampal CA1 neurons. *Neuroreport* **2002**.

(66) Bai, D.; Muller, R. U.; Roder, J. C. Non-ionotropic cross-talk between AMPA and NMDA receptors in rodent hippocampal neurones. *J. Physiol. (London)* **2002**, *543*, 23–33.

(67) Nowak, M. W.; Gallivan, J. P.; Silverman, S. K.; Labarca, C. G.; Dougherty, D. A.; Lester, H. A. In vivo incorporation of unnatural amino acids into ion channels in Xenopus oocyte expression system. *Methods Enzymol.* **1998**, *293*, 504–529.

(68) Rodriguez, E. A.; Lester, H. A.; Dougherty, D. A. Improved amber and opal suppressor tRNAs for incorporation of unnatural amino acids in vivo. Part 1: minimizing misacylation. *RNA* **2007**, *13*, 1703–1714.

(69) Rodriguez, E. A.; Lester, H. A.; Dougherty, D. A. Improved amber and opal suppressor tRNAs for incorporation of unnatural amino acids in vivo. Part 2: evaluating suppression efficiency. *RNA* **2007**, *13*, 1715–1722.

(70) Saks, M. E.; Sampson, J. R.; Nowak, M. W.; Kearney, P. C.; Du, F.; Abelson, J. N.; Lester, H. A.; Dougherty, D. A. An engineered Tetrahymena tRNAGln for in vivo incorporation of unnatural amino acids into proteins by nonsense suppression. *J. Biol. Chem.* **1996**, *271*, 23169–23175.

(71) Pantoja, R.; Rodriguez, E. A.; Dibas, M. I.; Dougherty, D. A.; Lester, H. A. Single-molecule imaging of a fluorescent unnatural amino acid incorporated into nicotinic receptors. *Biophys. J.* **2009**, *96*, 226–237.

(72) Rodriguez, E. A.; Lester, H. A.; Dougherty, D. A. In vivo incorporation of multiple unnatural amino acids through nonsense and frameshift suppression. *Proc. Natl. Acad. Sci. U.S.A.* **2006**, *103*, 8650–8655.

Chapter 2

Chemical-Scale Studies of the Phe-Pro Conserved Motif in the Cys Loop of Cys-Loop Receptors[1]

2.1 Introduction

The Cys-loop superfamily of neurotransmitter-gated ion channels includes the nicotinic acetylcholine receptor (nAChR)[2], the 5-HT_3 serotonin receptor, the $GABA_A$ and $GABA_C$ receptors, and the glycine receptor (*1*, *2*). Together, these receptors mediate both excitatory and inhibitory fast synaptic transmission throughout the central and peripheral nervous systems. The eponymous Cys loop, a disulfide-linked sequence Cys-Xaa_{13}-Cys, is located at the interface between the extracellular and transmembrane domains of the receptor (Figure 2.1A), and many studies have established that the Cys loop is essential for receptor function. Not part of the agonist binding-site, the Cys loop probably

[1] This chapter is a reproduced excerpt, with minor editing, from Limapichat, W.; Lester, H. A.; Dougherty, D. A. Chemical scale studies of the Phe-Pro conserved motif in the Cys loop of Cys loop receptors. *J. Biol. Chem.* **2010**, *285*, 8976–8984.

[2] The abbreviations used are: nAChR, nicotinic acetylcholine receptor; ACh, acetylcholine; SuCh, succinylcholine; Pip, pipecolic acid; Aze, azetedine-2-carboxylic acid; Dhp = 3,4-dehydroproline; Mor, morpholine-3-carboxylic acid; *c*-4F-Pro, *cis* 4-fluoro-proline, *t*-4F-Pro, *trans* 4-fluoro-proline; 3-Me-Pro, *trans* 3-methyl-proline; 2-Me-Pro, 2-methyl-proline; Cha, cyclohexylalanine; F-Phe, 4-fluorophenylalanine; F_3-Phe, 3,4,5-trifluorophenylalanine; Me-Pro, 4-Me-phenylalainine; Me_2-Phe, 3,5-dimethyl-phenylalanine; Fmoc, *N*-(9- fluorenyl)methoxycarbonyl; NVOC, *O*-nitroveratryloxycarbonyl; MS, mass spectrometry

plays a key role in receptor gating, transmitting structural changes initiated by agonist binding to the ion channel region of the receptor (*3*–*7*).

The intervening residues of the Cys loop show considerable conservation across the family (Figure 2.1B). Specifically, a completely conserved Phe-Pro motif (followed by Phe or Met) lies at the apex of the Cys loop. (These are residues 135 and 136 in the α1 subunit of the muscle-type nAChR, which is the system studied here.) Proline residues are unique among the 20 natural amino acids in several ways. Of particular interest here is the much greater tendency of prolyl peptide bonds to exist in the *cis* conformation (*8*–*12*). The presence of the Phe in the Phe-Pro motif makes this possibility more enticing. It is well established that an aromatic amino acid *N*-terminal of a proline enhances the likelihood of a *cis* conformation, roughly doubling the contribution of the *cis* peptide in the conformational equilibrium (*12*). Indeed, previous studies of the analogous motif in the 5-HT_3 receptor using conventional mutagenesis led to a postulation that the Pro was in a *cis* conformation (*13*).

Currently available structural information related to Cys-loop receptors adds to the intrigue (Figure 2.2). (Note that the acetylcholine-binding protein, arguably the most valuable structural model for the extracellular domain, does not contain a Cys loop and does not contain the Phe-Pro sequence (*14*).) In the medium resolution electron microscopic structure of the *Torpedo* nAChR (Protein Data Bank code 2BG9), the proline of the α1 subunit is in the *trans* conformation, and there is clearly no structural interaction at all between the side chains of Phe135 and Pro136 (*15*). In contrast, in the high-resolution x-ray crystal structure

of the mouse muscle nAChR α1-subunit extracellular domain complexed to α-bungarotoxin (Protein Data Bank code 2QC1), the proline is in its *cis* form, and the Phe-Pro rings are stacked (*16*). (The *Torpedo* and mouse muscle receptors show very high sequence identity/similarity throughout their structures). Additionally, an NMR study of the isolated Cys loop of the nAChR found a roughly 1:1 mixture of *cis* and *trans* conformers, a ratio that can be modulated by glycosylation (*17*).

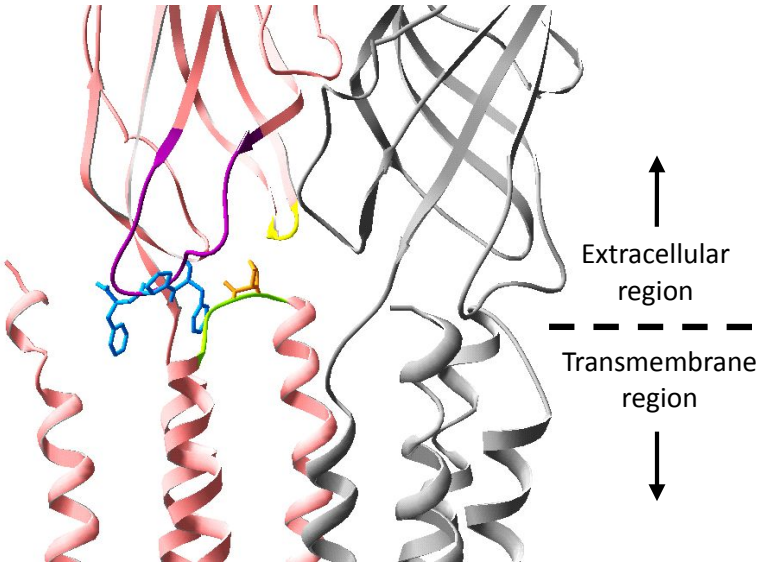

B

	Cys Loop Sequence
nAChR α1	CEIIVTH**FP**FDEQNC
nAChR α2	CSIDVTF**FP**FDQQNC
nAChR α3	CKIDVTY**FP**FDYQNC
nAChR α4	CSIDVTF**FP**FDQQNC
nAChR α5	CTIDVTF**FP**FDLQNC
nAChR α6	CPMDITF**FP**FDHQNC
nAChR α7	CYIDVRW**FP**FDVQHC
nAChR α9	CVVDVTY**FP**FDNQQC
nAChR α10	CRVDVAA**FP**FDAQHC
5-HT$_{3A}$R	CSLDIYN**FP**FDVQNC
pLGIC (ELIC)	NDMDFRL**FP**FDRQQF
pLGIC (GLIC)	SPLDFRR**YP**FDSQTL
GABAR α1	CPMHLED**FP**MDAHAC
GABAR α2	CPMHLED**FP**MDAHSC
GABAR α3	CPMHLED**FP**MDVHAC
GABAR α4	CPMRLVD**FP**MDGHAC
GABAR α5	CPMQLED**FP**MDAHAC
GABAR α6	CPMRLVN**FP**MDGHAC
GlyR α1	CPMDLKN**FP**MDVQTC
GlyR α2	CPMDLKN**FP**MDVQTC
GlyR α3	CPMDLKN**FP**MDVQTC
GluCl	CPMYLQY**YP**MDVQQC

Figure 2.1. Topology of the Cys loop. **(A)** Structure of the extracellular and the transmembrane interface of the *Torpedo* nAChR (Protein Data Bank code 2BG9). Only the α-subunit (red) and the γ-subunit (grey) are shown. The Cys loop is highlighted in purple, β1-β2 in yellow, and M2-M3 in green. The Phe-Pro-Phe motif in the Cys loop are shown in blue, and the Pro8* in the M2-M3 loop is shown in orange. **(B)** Sequence alignment of the Cys loop from various subunits of the Cys-loop superfamily

In recent years, several pentameric prokaryotic channels that are clearly related to the Cys-loop receptors have been discovered and crystallized. The prokaryotic channels contain a Phe/Tyr-Pro motif although they lack the cysteines of the Cys loop, and x-ray crystal structures confirm that the loop is still clearly in place. In a structure of the ELIC bacterial channel, which is believed to be a closed state (Protein Data Bank code 2VL0), the proline is in the *trans* conformation, and the Phe-Pro side chains are stacked (*18*). Two structures of the GLIC bacterial channel have appeared, and both are thought to be an open state of the channel. Both structures contain a completely stacked Tyr-Pro motif, but in one (Protein Data Bank code 3EAM), the proline is *cis* (*19*), and in the other (3EHZ) the proline is *trans* (*20*). The most recent crystal structure of the invertebrate glutamate-gated chloride channel from *C. elegans* (GluCl channel) reveals the Cys loops with a Tyr-Pro motif, and the proline appears to have the *trans* conformation (*21*).

Together, the structural data strongly indicate that (i) in the highly conserved Phe-Pro motif at the apex of the Cys loop of Cys-loop receptors, both *cis* and *trans* conformations around the prolyl amide bond are viable, and (ii) an interaction between the Phe and Pro side chains is possibly involved in the conformational preference. Although it is true that the three-dimensional fold of a protein may influence the *cis* preference of any given residue, the intrinsic conformational bias of the residue itself can still be expected to play an important role in determining structure and thus function of the protein (*12*).

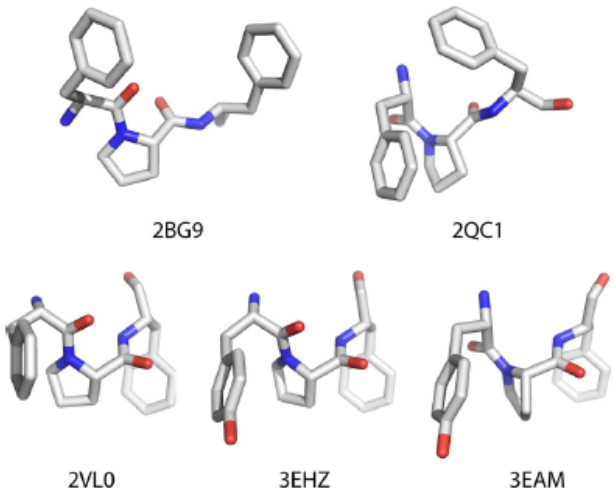

Figure 2.2. Images of the Phe/Tyr-Pro-Phe unit from five different relevant structures. Pro136 appears to have the *trans* conformation in the *Torpedo* nAChR (Protein Data Bank code 2BG9), ELIC bacterial channel (Protein Data Bank code 2VL0), and one GLIC bacterial channel (Protein Data Bank code 3EHZ) structures. However, crystal structures of the mouse muscle nAChR α1-subunit extracellular domain (Protein Data Bank code 2QC1) and the other GLIC bacterial channel (Protein Data Bank code 3EAM) show Pro136 in the *cis* conformation.

The feasibility of both *cis* and *trans* conformations at Pro136 presents the tantalizing opportunity that *cis-trans* isomerization of this conserved proline in the Cys loop, facilitated by the adjacent Phe, might be involved in the receptor gating mechanism. Such a *cis-trans* isomerization at a different proline has been shown to be essential to channel gating in the 5-HT_3 receptor (*5*).

In the present work, we have used a variety of tools to probe the Phe-Pro motif of the muscle-type nAChR, including unnatural amino acid mutagenesis, electrophysiology, and NMR spectroscopy of model peptides. We find evidence for a strong interaction between the two residues and an important role for the aromatic nature of the Phe. At both sites, side-chain hydrophobicity is favorable

to the receptor function. In addition, the results reveal a correlation between receptor function and *cis* bias at the proline backbone across a simple homologous series of proline analogs. This suggests a significant role for the *cis* proline conformer at this site in receptor function.

2.2 Results

2.2.1 Mutational Studies at Pro136

A previous study of the muscle-type nAChR in HEK293 cells showed that P136G mutations in the β and γ subunits prevented receptor assembly, whereas analogous mutations in the α or δ subunits prevented trafficking of receptors to the cell surface (*22*). Similarly, in previous studies of the analogous proline in the homopentameric 5-HT_3 receptor, the P136A mutant revealed no surface expression in HEK293 cells (*13*). In the more permissive *Xenopus* oocyte expression system, the muscle-type nAChR containing the αP136A mutation produces < 10% of the current levels seen for wild type. Surprisingly, this mutant receptor has an ACh EC_{50} value similar to that of the wild type. As discussed below, this result can be interpreted in several different ways; we therefore anticipated that the more subtle mutations enabled by unnatural amino acid mutagenesis would provide a more revealing analysis of the role of this residue.

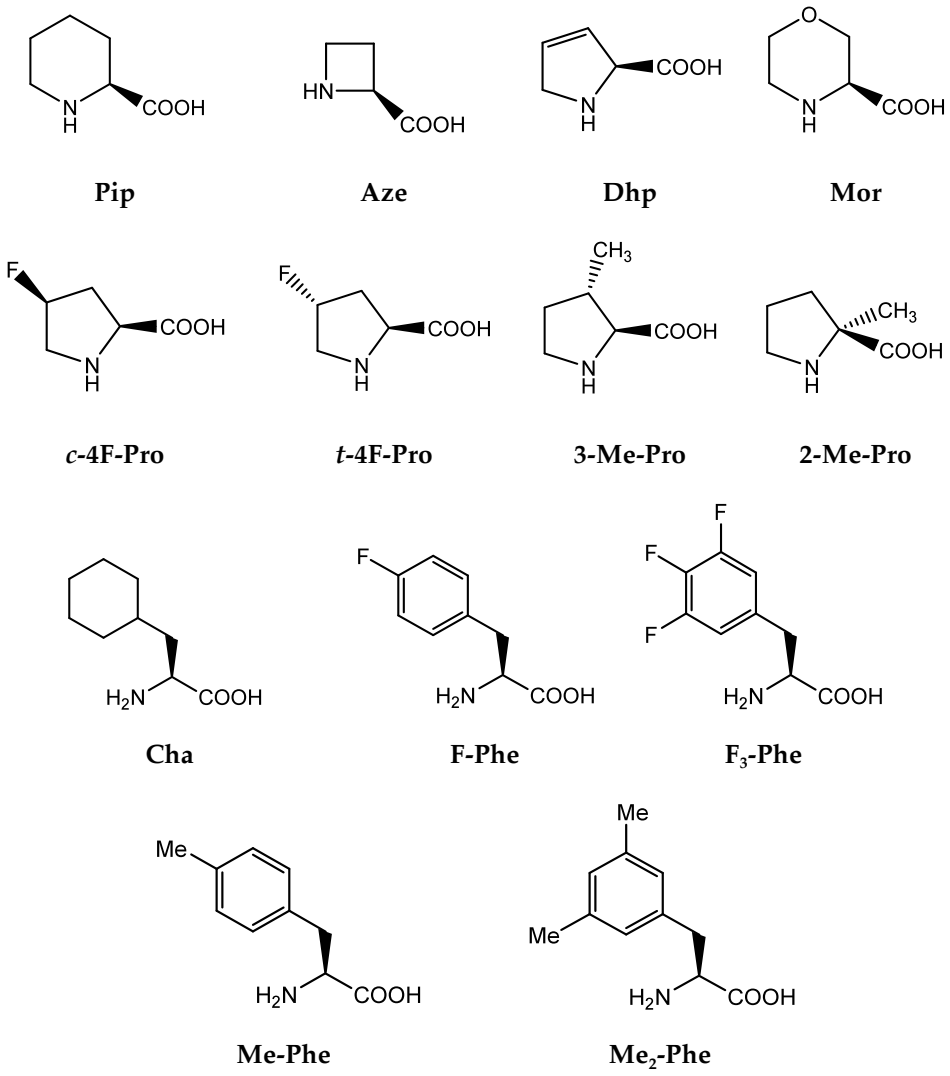

Figure 2.3. Structures of unnatural amino acids used in this study

Several unnatural analogs of proline (Figure 2.3) (*5*) were incorporated into the receptor using the *in vivo* nonsense-suppression method. These unnatural proline analogs have varying ring size, side-chain substitution, and intrinsic preferences for the *cis* conformer when probed in model systems (Table 2.1). The wild-type rescue experiment (i.e., incorporating Pro by nonsense suppression) displays the full phenotype of the wild-type receptor, including

ACh EC_{50} value, Hill coefficient, and current traces. This indicates that the nonsense suppression methodology is viable at the 136 site. Interestingly, Pro analogues at position 136 are generally gain-of-function (lower EC_{50}), the sole exception being 2-Me-Pro, which gives essentially wild-type behavior. Similar to the Ala mutation mentioned above, the current levels from experiments involving 2-Me-Pro are < 10% of those seen in comparable experiments with other mutations. Despite the relative subtlety of the mutations, the gain-of-function effects can be substantial, as seen with Pip and 3-Me-Pro, which show 13- and 22-fold decreases in EC_{50}, respectively, relative to wild type.

Table 2.1. EC_{50} and Hill constant values of mutant receptors containing unnatural amino acid at α136

Residue α136	**Reported percentage cis**[a]	**ACh EC_{50}**	**EC_{50}(mutant)/ EC_{50}(wild type)**	**Hill Constant**	***n***
	%	μM			
Pro	5	23 ± 0.2	1	1.5 ± 0.02	35
Pro[b]	5	22 ± 0.2	1	1.6 ± 0.03	8
Pip	12	1.8 ± 0.1	0.1	1.7 ± 0.08	7
Aze	18	5.8 ± 0.2	0.3	1.7 ± 0.07	10
c-4F-Pro	~5	12 ± 0.2	0.5	1.5 ± 0.04	6
t-4F-Pro	~5	10 ± 0.2	0.5	1.7 ± 0.04	7
3-Me-Pro	~5	1.0 ± 0.02	0.04	1.7 ± 0.04	7
2-Me-Pro	0	25 ± 0.7	1	1.6 ± 0.06	10
Dhp	NR[c]	18 ± 0.3	0.8	1.6 ± 0.03	10
Mor	NR[c]	8.7 ± 0.4	0.4	1.7 ± 0.05	9

[a] Ref. (5,8)
[b] Data obtained by suppression mutation
[c] NR, percentage *cis* values for these residues have not been reported in the literature.

Correlation between the *cis-trans* energy gap and the energy of channel activation could be expected if the receptor gating mechanism involves *cis-trans* isomerization of Pro136. However, no simple correlation is found (Table 2.1). For example, although both Pip and Aze show a stronger inherent *cis* preference than Pro and a lower EC_{50}, 3-Me-Pro shows a conformational bias very similar to that of Pro but a greatly diminished EC_{50}. Before analyzing these results in greater detail, however, we must consider the role of Phe135.

2.2.2 Mutational Studies at Phe135

Previous single channel studies have shown that the F135A mutation in the nAChR alters the gating mechanism, leading to two uncoupled open states that produce independent gating reactions from the diliganded closed state (*23*). In our studies of the nAChR, we found that the F135A mutation nearly obliterates receptor function; only very weak ACh-induced currents are observed despite normal surface expression levels (Figure 2.4).

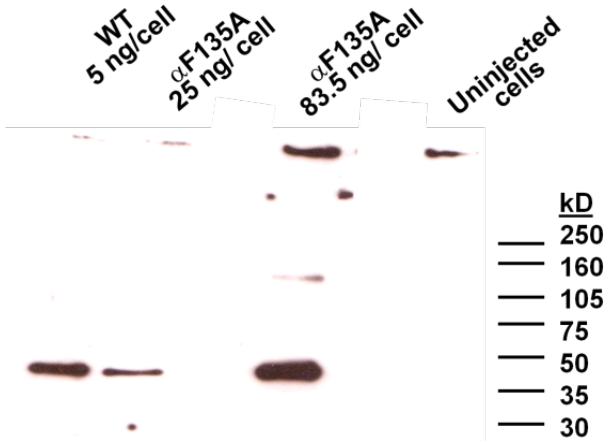

Figure 2.4. A Western blot analysis of Phe135Ala mutant receptor surface expression levels in comparison to the wild type. The experiment allowed visualization of the hemagglutinin epitope (HA) tag that had been incorporated into the α-subunit.

Seeking a more insightful analysis of the role of this residue, we probed the Phe135 site with an extensive series of Phe analogs. Again, the wild-type rescue experiment displays the full characteristics of the wild-type receptor. The Phe135 site is sensitive to even very subtle mutations, as shown in Table 2.2. Similar to what is observed with Pro136, Phe analogs consistently produce gain-of-function mutants. ACh sensitivity increases with the volume and number of hydrophobic substituents on the aromatic ring. For example, Me-Phe has a lower EC_{50} than F-Phe, and Me_2-Phe has a lower EC_{50} than Me-Phe. Surprisingly, cyclohexylalanine (Cha), which is similar to Phe in size and shape but is not aromatic (*24*), produces functional receptors with a small perturbation; EC_{50} is near the wild-type value. Given that the F135Cha mutant receptor is functional, aromaticity at position 135 is not an absolute requirement for the receptor to function.

To further explore the possible role of Phe135 in receptor gating, wild-type and mutant receptors were probed with the partial agonist succinylcholine (SuCh). Compared with ACh, SuCh produces only 14% of the maximal current under saturating drug concentrations in the wild-type receptor (Table 2.2). This indicates that upon receptor activation by SuCh, the channel open-closed equilibrium is shifted toward the open state, but to a much lesser extent relative to ACh activation. If a mutation produces a gain-of-function effect as a result of enhanced receptor gating, one could expect the mutation to improve the efficacy of a partial agonist like SuCh.

Table 2.2. EC_{50} and Hill constant values of mutant receptors containing unnatural amino acid at α135

Residue α135	ACh			SuCh			Efficacy[a]
	EC_{50}	Hill Constant	*n*	EC_{50}	Hill Constant	*n*	
	μM			μM			
Phe	23 ± 0.2	1.5 ± 0.02	35	59 ± 1	1.3 ± 0.03	13	0.14 ± 0.01
Phe[b]	23 ± 0.4	1.5 ± 0.03	8	NA[c]	NA[c]	NA[c]	NA[c]
F-Phe	2.6 ± 0.03	1.6 ± 0.02	7	32 ± 0.8	1.4 ± 0.04	9	0.54 ± 0.02
F_3-Phe	1.0 ± 0.02	1.5 ± 0.05	15	8.1 ± 0.2	1.6 ± 0.05	8	0.86 ± 0.02
Me-Phe	1.0 ± 0.02	1.6 ± 0.04	12	11 ± 0.2	1.5 ± 0.04	11	0.82 ±0.02
Me_2-Phe	0.22 ± 0.01	1.6 ± 0.07	9	1.6 ± 0.06	1.5 ± 0.07	7	0.93 ± 0.04
Cha	16 ± 0.2	1.6 ± 0.02	15	60 ± 1	1.6 ± 0.03	9	0.10 ± 0.01

[a] Determined by the average of I_{max}(SuCh)/I_{max}(ACh)

[b] Data obtained by suppression mutation.

[c] NA, data not available.

The EC_{50} trend of SuCh (Table 2.2) parallels that of ACh, implying that the mutants respond to both drugs in the same way. As anticipated, all of the Phe

analogs that show a lowered EC_{50} do increase the relative efficacy of SuCh with respect to ACh. This suggests that mutations at position 135 primarily affect receptor gating. Note that the non-aromatic analog Cha shows essentially wild-type EC_{50} for both ACh and SuCh and that this mutation has no strong effect on the relative efficacy.

2.2.3 Interaction between Phe135 and Pro136

There is considerable evidence supporting a specific interaction in a Phe-Pro sequence that stabilizes the *cis* form of the Pro. This could possibly involve a polar–π interaction in which polarized C–H bonds ($C^{\delta-}$–$H^{\delta+}$) on the proline interact favorably with the negative electrostatic potential on the face of the Phe side chain stacked on the Pro (*9*, *11*). We investigated the possibility of a Phe-Pro interaction in this system by testing double mutant receptors in which Phe135 was substituted with the non-aromatic Cha and Pro136 was substituted with either Pip or 3-Me-Pro, the two mutations that cause the largest EC_{50} shifts. These experiments required consecutive incorporation of two different unnatural amino acids, an unprecedented experiment for receptors expressed in a living cell that was made possible by recent advances in tRNA design (*25*, *26*). The resulting current signals (1–4 μA) were quite sufficient for quantitative analysis.

The F135Cha mutation substantially diminishes the large effects of the mutations at Pro136. As shown in Figure 2.5, the 13- and 22-fold drops in EC_{50} for Pip and 3-Me-Pro, respectively, seen in a wild-type Phe background fall to ~

2.5-fold in the presence of F135Cha. A standard evaluation of double mutants employs a mutant cycle analysis, which has been used successfully with EC_{50} values for Cys-loop receptors in several instances (*27*–*30*). For the interaction of F135Cha with P136Pip and P136(3-Me-Pro), we find coupling parameters (Ω) of 5 and 10, respectively, which correspond to coupling energies (RTln(Ω)) of 1.0 and 1.3 kcal/mol, respectively. These energies are significant for such subtle mutations and are indicative of a strong interaction between these two residues.

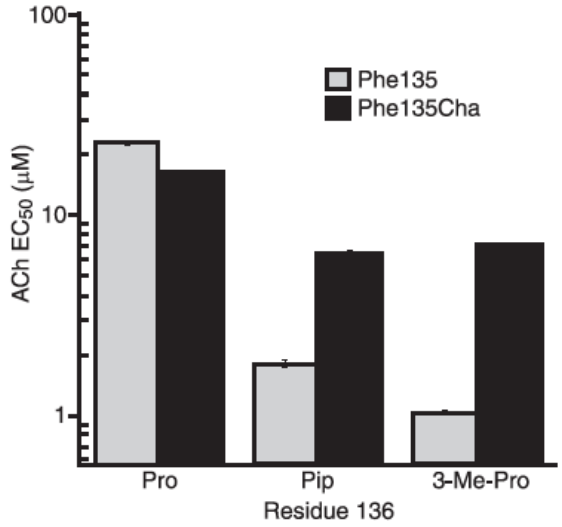

Figure 2.5. ACh EC_{50} results from single and double mutation experiments at residues 135 and 136 in comparison with the wild-type value. For F135Cha/P136Pip, EC_{50} = 6.5 ± 0.2 μM, Hill constant = 1.7 ± 0.07 μM, n = 9. For F135Cha/P135(3-Me-Pro), EC_{50} = 6.9 ± 0.2 μM, Hill constant = 1.5 ± 0.06 μM, n = 12.

Having established a strong interaction between Phe135 and Pro136, we considered whether the intrinsic *cis-trans* equilibrium reported for proline and the proline analogs would be altered because of the preceding Phe. This would indicate that the percentage *cis* values used previously (*31*) and reported in Table

2.1 may not be appropriate for the present system because no aromatic amino acid was involved. As such, we set out to determine percentage *cis* values that are more appropriate to the Phe-Pro motif.

2.2.4 Determination of Inherent cis Preferences of Model Peptides Containing Proline Analogs Preceded by Phe

In order to determine whether the data in Table 2.1 reflect the innate *cis* preference of residue Pro136, it is necessary to measure the *cis-trans* energy gap (ΔG(*c*-*t*)) for each unnatural amino acid substituted at this site, taking into account the aromatic–proline interaction. In fact, ΔG(*c*-*t*) for the Gly-Phe-Pro-Gly and Gly-Phe-Pip-Gly peptides have been reported (*32*). Using a similar solution NMR technique, it should be possible to determine ΔG(*c*-*t*) values for our series of unnatural analogs of proline following a Phe residue in model peptides.

Model peptides Gly-Phe-X_{Pro}-Gly, where X_{Pro} represents Pro, Pip, Aze, *c*-4F-Pro, Mor, 3-Me-Pro, and 2-Me-Pro, were synthesized via standard solid-phase peptide synthesis methods. These peptides were then subjected to solution NMR experiments similar to those in Ref. (*32*). Protons were assigned by two-dimensional gCOSY and/or TOCSY experiments. The proportion of each of the two conformers in solution was measured by integration of a corresponding, well-resolved peak after base-line correction. Representative sample spectra are shown in Figure 2.6. Conformational assignments were based on known chemical shifts of the Gly-Phe-Pip-Gly peptide reported in Ref. (*32*).

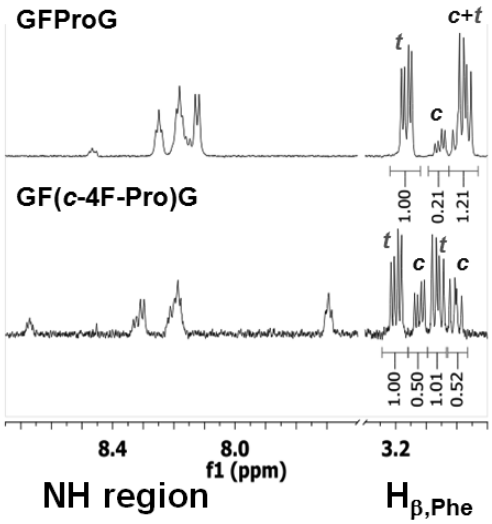

Figure 2.6. Samples of one-dimensional ^{1}H NMR spectra of Gly-Phe-Pro-Gly (*top*) and Gly-Phe-(*c*-4FPro)-Gly (*bottom*) peptides showing the amide and $C^{\beta}_{Phe}H_2$ regions. *t* denotes peaks from *trans* peptide. *c* denotes peaks from the *cis* peptide.

The results from the solution NMR experiments (Table 2.3) show that the *cis* preferences are indeed higher than the reported values in model peptides lacking the aromatic residue (Table 2.1). Note that for the Gly-Phe-(2-Me-Pro)-Gly peptide, the *cis* form was not observed. The model peptide containing Mor has a very high *cis* propensity; nearly 50% of the peptide is in the *cis* form. Moreover, one of the protons attached to the C^{β} of the Mor ring displays a large upfield shift in the *cis* peptide compared with that of the *trans* peptide (Table 2.4), as has also been reported with the structurally similar Pip (32). In the Pip-containing peptide, the chemical shifts of C^{β} protons are 1.72 and 2.15 ppm in the *trans* conformation and 0.35 and 1.90 ppm in the *cis* conformation. Likewise, for the Mor-containing peptide, the chemical shifts change from 3.74 and 4.37 ppm in the *trans* conformation to 2.10 and 3.74 ppm in the *cis* conformation. Most importantly, the

Phe residue can alter the trends in *cis*-*trans* preferences, as shown for the simple homologous series Aze, Pro, Pip (Table 2.1 compared with Table 2.3).

Table 2.3. ΔΔG(*c*-*t*) calculated from the percentage of *cis* results of solution NMR experiments for each amino acid and the ΔΔG(EC_{50}) calculated from electrophysiology results of mutant receptors containing the corresponding amino acid at α136

X_{Pro}	Percentage *cis*	ΔΔG(*c*-*t*)[a]	ΔΔG(EC_{50})[b]
	%	(kcal.mol^{-1})	(kcal.mol^{-1})
Pro	17	0	0
Pip	39	0.65	1.5
Aze	30	0.42	0.81
c-4F-Pro	32	0.49	0.38
3-Me-Pro	12	-0.24	1.8
2-Me-Pro	0	-	-0.056
Mor	48	0.87	0.57

[a] ΔΔG(*c*-*t*) = RTln(% *cis*(Pro analogue)/% *cis*(Pro)).

[b] ΔΔG(EC_{50}) = RTln(EC_{50}(Pro analogue)/EC_{50}(Pro)).

Table 2.4. Proton chemical shift assignments in 90% H_2O/10% D_2O at pH 5, 298K for both the *trans* and the *cis* conformers of $GAX_{Pro}G$ peptides

X_{pro}		*trans*	*cis*
Pro	α	4.43	3.81
	β	1.96, 2.28	1.74, 1.93
	γ	2.00, 2.03	1.70, 1.73
	δ	3.58, 3.86	3.37, 3.53
Aze	α	NA[a,b]	3.96
	β	2.25, 2.60	2.10, 2.27
	γ	4.01, 4.36	3.73, 3.87
c-4F-Pro	α	4.68	3.91
	β	2.44, 2.54	1.70, 2.38
	γ	5.40	5.24
	δ	3.96, 4.05	3.66, 3.80
2-Me-Pro	$-C^{\alpha}CH_3$	1.51	NA[a]
	β	1.98, 2.13	NA[a]
	γ	2.00, 2.03	NA[a]
	δ	3.71, 3.92	NA[a]
3-Me-Pro	α	4.00	3.54
	β	2.31	2.30
	$-C^{\beta}CH_3$	1.15	0.75
	γ	1.70, 2.17	1.31, 1.92
	δ	3.55, 3.90	3.26, 3.45
Pip	α	5.11	4.61
	β	1.72, 2.15	0.35, 1.90
	γ	1.46, 1.68	1.22, 1.44
	δ	1.55, 1.68	1.10, 1.58
	ε	3.20, 3.93	2.46, 4.32
Mor	α	5.00	4.40
	β	3.74, 4.37	2.10, 3.74
	δ, ε[c]	3.90, 3.95	3.76, 4.06
		3.47, 3.62	2.95, 3.10

[a] NA, data not available
[b] Possibly overlapping with the suppressed water peak
[c] Unable to make a definite assignment

2.3 Discussion

Cys-loop neurotransmitter-gated ion channels are remarkable molecular machines. In response to the binding of a small-molecule ligand, these large proteins undergo a global conformational change, opening a selective ion channel and thereby converting a chemical event (i.e., ligand binding) to an electrical signal. The precise mechanism of this process is a central issue in molecular neurobiology. Recently, chemical-scale studies have provided valuable insights into the structure and function of these receptors, yet significant challenges still remain.

Here we have evaluated the highly conserved and structurally intriguing Phe135-Pro136 motif of the prototypic Cys-loop receptor, the nAChR. Proline is well appreciated to display novel conformational behaviors compared with all other natural amino acids. Additionally, it has been proposed that prolines might play a key role in the conformational changes that are essential to the function of many types of receptors (*33*). Several lines of evidence establish that local amino acids flanking proline can influence proline conformational preferences (*9*, *11*, *12*, *34*). In particular, an aromatic residue preceding the proline is found to enhance the fraction of the *cis* isomer for peptides in solution (*12*). As shown in Figure 2.2, Pro136 can exist in both *cis* and *trans* conformations, and the two crystal structures with a *cis* peptide bond — the α1 extracellular domain (Protein Data Bank code 2QC1) and the GLIC bacterial channel (Protein Data Bank code 3EAM) — show stacking of the Phe-Pro side chains. Given the complete conservation of the Phe-Pro motif and the available

structural data, it seemed reasonable to speculate that the *cis* conformer of Pro136 could be involved in receptor function.

Our primary measure of receptor function is EC_{50}, the effective concentration of agonist required to achieve half-maximal response. Agonist binding to a receptor induces step-by-step conformational changes that lead to opening of the ion channel; therefore, EC_{50} is a value that reflects the composite effect of the agonist-binding affinity and the sequential gating events. The Phe-Pro motif is remote from the agonist-binding site, and the Cys loop is firmly established to play an essential role in gating (*35*). In addition, we find that a number of mutations at residue 135 greatly increase the efficacy of the partial agonist SuCh, supporting the notion that this residue participates in the gating mechanism. As such, we interpret changes in EC_{50} to reflect primarily, if not exclusively, changes in receptor gating.

The involvement of the Phe-Pro motif in gating is further supported by a previous single channel study on the F135A mutation, which indicated that the gating mechanism is modified as a result of this mutation (*23*). The new mechanism appears to be much less efficient at coupling agonist binding to channel opening, consistent with our macroscopic observations of greatly reduced current for this mutant.

Conventional mutations at Pro136 also have strong effects on the receptor. When expressed in HEK293 cells, both Gly mutants in the nAChR subunits and an Ala mutant in the related 5-HT_3 receptor (*13*) gave receptors that were substantially impaired in the ability to assemble and/or traffic to the surface. In

the *Xenopus* oocyte system, we find that the P136A mutant gave < 10% of the current levels seen from wild type, again suggesting a disruption of assembly and/or trafficking or a disruption of gating.

Similarly, in an earlier study of Pro308 in the M2-M3 loop of the 5-HT_3 receptor, in which a compelling correlation between *cis* propensity of incorporated proline analogs and receptor function was demonstrated, structural disruption by conventional mutagenesis produced ambiguous results (*5*). In that study, Ala, Cys, Gly, Lys, Val, and Gln conventional mutants gave nonfunctional receptors. More recently, studies of an orthologous 5-HT_3 receptor showed that His and Trp mutants did give functional receptors (*36*). We note that aromatic amino acids, such as His and Trp, are more than twice as likely to be in a *cis* conformation as other non-proline natural amino acids (*37*). Again, the implications of the conventional mutagenesis results are open to debate.

Using conventional mutagenesis to probe the role of the *cis* conformation of a highly conserved proline is, in our view, unlikely to produce compelling results. Such studies frequently assume that simply seeing a functional receptor with a non-proline natural amino acid incorporated rules out a role for the *cis* conformer. However, previous studies have demonstrated that in some cases, when a *cis* proline is mutated to an alanine, the main-chain *cis* bond is preserved, presumably because the three-dimensional structure favors the *cis* conformation (*11*). In such cases, the Pro to Ala mutation often reduces the stability of the protein, which could manifest as lower expression levels, as we see with the P136A mutant. In addition, as with Pro, the presence of an aromatic amino acid

(such as Phe) *N*-terminal to an aliphatic residue (such as Ala) doubles the probability of a *cis* conformation (*37*). Alternatively, replacement of a proline with another natural amino acid could produce functional receptors via a different gating path that has become more energetically accessible, parallel to what is seen with the F135A mutation (*23*).

When studying such a structurally distinctive motif as Phe-Pro, the benefits of unnatural amino acid mutagenesis are amplified. The subtle perturbations allow one to maintain the essential motif while probing its intrinsic features. We have used unnatural amino acids to probe several aspects of the Phe-Pro motif, including the importance of Phe aromaticity, the roles of side-chain hydrophobicity and volume, and the possibility of *cis-trans* isomerization at the proline backbone.

Several intriguing observations emerge from the unnatural amino acid mutagenesis studies. Considering Pro136, subtle mutations produce noticeable changes in EC_{50}. For example, simply adding a methyl group (3-Me-Pro) can lower EC_{50} 22-fold, and adding a single CH_2 group to the ring (Pip) can lower EC_{50} 13-fold. Mutations are generally gain-of-function; EC_{50} decreases. The only residue that is not gain-of-function but instead gives nearly wild-type EC_{50} is 2-Me-Pro. Similar to Ala, 2-Me-Pro also produces much smaller whole cell currents.

As with the proline, subtle mutations of Phe135 can produce substantial changes in EC_{50}; a 100-fold shift arises from just the addition of two methyl groups fairly remote from the protein backbone (Me_2-Phe). Paralleling the

proline results, all of the unnatural amino acid mutants are gain-of-function. Moreover, an interesting trend is evident; Figure 2.7 shows a plot of log(EC_{50}) for the receptor versus the side-chain logP, a measure of its hydrophobicity. Although the cyclohexyl compound (Cha) is clearly an outlier, a significant correlation is seen among the aromatic side chains. These results indicate that hydrophobicity is an important determinant at position 135, with an increase in hydrophobicity making the channel easier to open. This is consistent with a molecular dynamics simulation of the α7 nAChR that places Phe135 in a hydrophobic pocket in an open state (*38*). In addition, the logP analysis (Figure 2.7) highlights the role of aromaticity at residue 135 because Cha has essentially the same hydrophobicity as both Me-Phe and F_3-Phe but a much higher EC_{50}. As such, the F135Cha mutant, being more hydrophobic than the wild-type Phe but lacking the aromaticity, appears to have a nearly wild-type ACh EC_{50}. From these data, we conclude that both hydrophobicity and aromaticity at position 135 are important in receptor function.

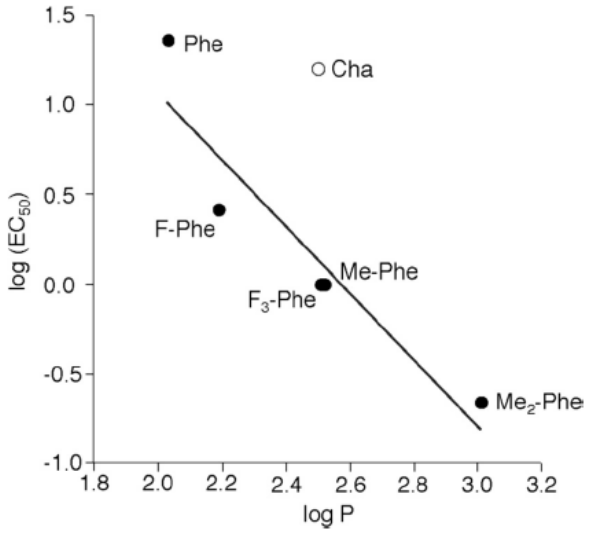

Figure 2.7. Correlation between EC_{50} and logP for mutations at Phe135. Note that the Cha point was not included in the linear fit.

The results of our double mutant studies have confirmed an important interaction between residues 135 and 136; the large effects caused by mutation at Pro136 are attenuated when Phe135 is simultaneously mutated to the non-aromatic Cha (Figure 2.5). Mutant cycle analysis shows significant coupling energies between residues 135 and 136.

We noted above the intriguing possibility that *cis-trans* isomerization at Pro136 is involved in receptor gating. In the present work, we did not see a simple correlation between EC_{50} and previously reported innate percentage *cis* values of the Pro analogs. However, there is ample precedent showing a deviation of percentage *cis* from the innate value when the preceding residue is aromatic (*12*). To probe the impact of the Phe residue on the present system, we used NMR spectroscopy to evaluate the *cis-trans* preference in the model peptides Gly-Phe-X_{Pro}-Gly, where X_{Pro} represents Pro, Pip, Aze, *c*-4F-Pro, Mor, 3-

Me-Pro, and 2-Me-Pro. Because the *cis* form of the Gly-Phe(2-Me-Pro)-Gly peptide was not observed, we cannot comment on the role of Phe in this system. In all other cases, comparisons are possible, and the Phe does increase the percentage *cis* at the adjacent Pro analog. The substantial upfield chemical shift of the C^{β} proton in the *cis* conformer supports the existence of the putative interaction between the proline ring and the aromatic ring of the phenylalanine residue (Table 2.4).

In Table 2.3, we report $\Delta\Delta G(c\text{-}t)$, the extent to which the proline analog shows an increased bias for the *cis* form relative to proline. To facilitate comparisons, we also convert each EC_{50} shift into an energy term, $\Delta\Delta G(EC_{50})$. We first considered the homologous series of unsubstituted rings Aze, Pro, and Pip, in which the ring size expands from 4 to 5 to 6. The percentage *cis* and EC_{50} values track each other; EC_{50} is Pip < Aze < Pro, whereas percentage *cis* is Pip > Aze > Pro (Figure 2.8, solid line). Note that in this simple series, the Phe substituent is critical because the inherent percentage *cis* sequence absent the Phe is Aze > Pip > Pro (Figure 2.8, dotted line). Having an aromatic residue adjacent to the proline alters the *cis* bias differentially across this homologous series, and the EC_{50} values for the receptor mirror this effect. These data suggest that proline *cis-trans* isomerization at this site may play a role in receptor gating.

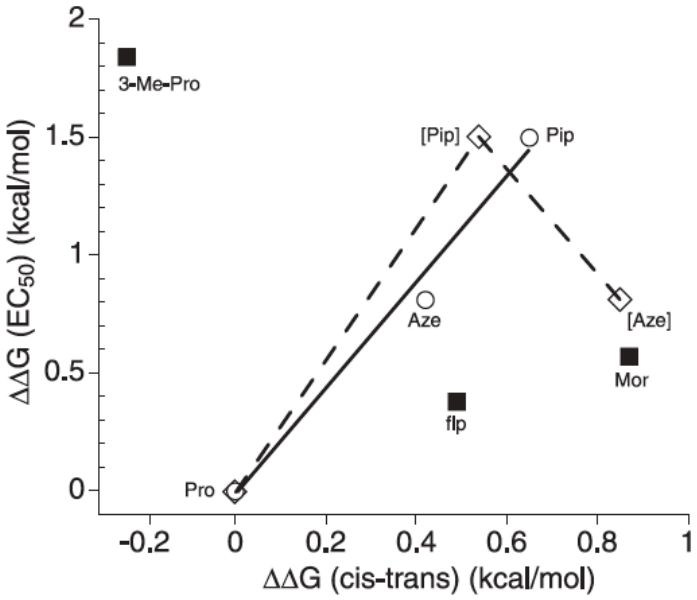

Figure 2.8. Relationship between EC_{50} values and *cis-trans* preferences for Pro and analogs at position 136. All values are relative to Pro. Solid line and open circles, Pro, Aze, and Pip using *cis-trans* values determined in the present study for the Gly-Phe-Xaa-Gly sequence (Table 2.3). Dashed line and open diamonds, Pro, Aze, and Pip using *cis-trans* values previously determined for sequences that do not have an aromatic *N*-terminal to the Pro analog. Solid squares, data points (*c*-4F-Pro, Mor, and 3-Me-Pro) that deviate from the trend set by the solid line

Concerning the more dramatic proline mutations, a simple percentage *cis* correlation is not evident. It is clear from the Phe135 mutational studies that receptor function is highly sensitive to side-chain polarity at the 135 site (Figure 2.7), with increased side-chain hydrophobicity lowering EC_{50}. It seems reasonable to expect a similar effect at the adjacent Pro136 because Phe and Pro interact, as shown by the mutant cycle analysis. Indeed, our results suggest a preference for side-chain hydrophobicity at the Pro136 site as well. Mor is structurally very similar to Pip, but it does not fit into the Aze-Pro-Pip correlation. We propose that EC_{50} for Mor is anomalously high because of the increased polarity relative to Pip. Similarly, *c*-4F-Pro has a significantly higher percentage *cis* than Pro but

only a modest decrease in EC_{50}, apparently due to the increased polarity of the fluorine substituent. In fact, a second linear correlation can be seen in Figure 2.8 involving the Pro-(*c*-4F-Pro)-Mor series, although the structural variation across this series is less consistent than in the Aze-Pro-Pip trio. 3-Me-Pro shows a smaller percentage *cis* than Pro but the lowest EC_{50} among the amino acids at the 136 sites. Interestingly, adding a single CH_3 group to Pro136 has the same effect on EC_{50} as adding a single CH_3 group to Phe135 (3-Me-Pro and Me-Phe show the same EC_{50}). Inspection of simple molecular models leads to an observation that the two CH_3 groups could point into nearly the same region of the receptor when the proline is in the *cis* form. Perhaps each CH_3 fits into a hydrophobic pocket, stabilizing the open state of the receptor and lowering EC_{50}.

As shown Figure 2.8, in the most conservative structural series (Pro, Pip, and Aze), we do find a trend that is suggestive of *cis-trans* isomerization at Pro136. Importantly, this trend is seen only when the perturbing effect of the Phe residue is included, justifying the consideration of the Phe-Pro unit as a single motif. Residues that involve more complex changes do not fit the correlation, but generally the deviation is consistent with the notion that increasing side-chain hydrophobicity lowers EC_{50}. From our data, we propose that both *cis* propensity and side-chain hydrophobicity at Pro136 simultaneously are determinants of nAChR function. Moreover, the possibility of *cis-trans* isomerization at Pro136 being involved in gating cannot be ruled out.

In summary, the subtle mutations enabled by unnatural amino acid mutagenesis have allowed a detailed study of the Phe-Pro motif in the Cys loop

of a Cys-loop receptor. Mutant cycle analysis reveals a strong interaction between the two residues and a strong preference for an aromatic residue at position 135. In addition, a clear trend is evident whereby increasing hydrophobicity at either Phe135 or Pro136 lowers EC_{50}. Although the analysis of residue Pro136 is complex, the data provide evidence supporting a role of the *cis* conformer in receptor function.

2.4 Materials and Methods

Synthesis of dCA-amino acids

The preparations of amino acids coupled to the dinucleotide (dCA) have been described previously (*39*) with the exception of dCA-Dhp and dCA-Mor. (*S*)-3-morpholinecarboxylic acid HCl was purchased from Tyger Scientific, Inc. (Ewing, NJ), and 3,4-dehydro-*L*-proline (Dhp) from Chem-Impex International Inc. (Wood Dale, IL). The amino groups were protected as the *O*-nitroveratryloxycarbonyl (NVOC) group. NVOC-Cl was purchased from Aldrich. (NVOC)-3,4-dehydroproline cyanomethyl ester and (NVOC)-morpholine cyanomethyl ester were prepared according to the representative protocol reported in Ref. (*40*). Products were characterized by NMR spectroscopy. The NMR spectra, both ^{1}H and ^{13}C, are complicated because each compound shows two distinct conformations in the solution.

(NVOC)-3,4-Dehydroproline cyanomethyl ester. ^{1}H NMR (500 MHz, $CDCl_3$) δ3.95–4.03 (m, 6H), 4.34–4.43 (m, 2H), 4.69–4.87 (m, 2H), 5.20–5.21 (m, 2H), 5.43–

5.67 (m, 2H), 5.76–5.83 (m, 1H), 7.01 (s, 1H), 7.71 (m, 1H). ^{13}C NMR (125 MHz, $CDCl_3$) δ49.20, 49.23, 53.57, 54.20, 56.54, 56.57, 56.87, 64.66, 65.08, 65.92, 66.28, 108.34, 108.37, 110.07, 111.25, 113.96, 113.98, 123.46, 123.71, 127.44, 127.85, 130.37, 130.49, 139.88, 139.92, 148.32, 148.43, 153.39, 153.76, 153.81, 153.96, 168.41, 168.83. High-resolution MS analysis (FAB^+) calcd for $C_{17}H_{18}N_3O_8$ m/z = 392.1094, found 392.1109.

(NVOC)-Morpholine cyanomethyl ester. ^{1}H NMR (500 MHz, $CDCl_3$) δ3.24–3.48 (m, 1H), 3.51 (dt, 1H), 3.69–3.75 (m, 1H), 3.83–3.95 (m, 2H), 3.94–3.95 (m, 3H), 3.99–4.02 (m, 3H), 4.33–4.41 (m, 1H), 4.63–4.85 (m, 3H), 5.41 (dd, 1H), 5.69 (dd, 1H), 6.88–6.97 (m, 1H), 7.66–7.70 (m, 1H). ^{13}C NMR (125 MHz, $CDCl_3$) δ41.22, 41.73, 49.39, 49.45, 54.53, 55.05, 56.53, 56.60, 56.81, 64.91, 65.31, 66.29, 66.73, 66.99, 67.34, 108.32, 108.36, 109.91, 111.13, 113.84, 113.89, 126.93, 127.66, 139.78, 140.11, 148.32, 148.53, 153.66, 153.81, 155.14, 156.04, 168.69, 168.89. High-resolution MS analysis (FAB^+) calcd for $C_{17}H_{20}N_3O_9$ m/z = 410.1199, found 410.1180.

Dhp and Mor cyanomethyl esters were coupled to dCA following the protocol in Ref. (*40*).

dCA-Dhp. ES-MS calcd for $C_{34}H_{40}N_{10}O_{20}P_2$ m/z 970.2; found $(M - H)^-$ m/z 969.0, $(M+Na-2H)^-$ m/z 991.1, and $(M+Na-H)^-$ m/z 992.0.

dCA-Mor. ES-MS calcd for $C_{34}H_{42}N_{10}O_{21}P_2$ m/z 988.2; found $(M - H)^-$ m/z 987.0, $(M+Na-2H)^-$ m/z 1009.0, and $(M+Na-H)^-$ m/z 1010.0.

Molecular Biology

Subunits of embryonic mouse muscle nAChR were in pAMV vectors. The α subunit contains the hemagglutinin epitope (HA) tag in the M3-M4 loop. There is no significant shift in EC_{50} caused by the insertion of the HA tag at this location. Site-directed mutagenesis was performed using the Stratagene QuikChange protocol. For single unnatural amino acid incorporation, the site of interest was mutated to an amber stop codon. For double unnatural acid incorporation, the 135 site was mutated to the opal stop codon and the 136 site was mutated to the amber stop codon. Circular cDNA was linearized with NotI or KpnI. After purification (Qiagen), linearized DNA was used as a template for runoff *in vitro* transcription using T7 mMessage mMachine kit (Ambion). The resulting mRNA was purified (RNAeasy Mini Kit, Qiagen) and quantified by UV-visible spectroscopy.

THG73 (*41*) and TQOpS′ (*25*, *26*) were used as amber suppressor tRNA and opal suppressor tRNA, respectively. Conjugated dCA-amino acid was ligated to 74-nucleotide tRNA as previously reported (*39*). Crude tRNA-amino acid product was used without desalting, and the product was confirmed by MALDI-TOF MS on 3-hydroxypicolinic acid (3-HPA) matrix. Deprotection of the NVOC group on tRNA-amino acid was carried out by 5-minute photolysis immediately prior to injection.

Microinjection

Stage V–VI *Xenopus laevis* oocytes were employed. For wild-type receptor and receptors containing conventional mutations, quantified mRNA of all subunits were mixed in a ratio of α:β:γ:δ = 2:1:1:1 by mass. If an unnatural amino acid was to be incorporated into the α subunit, the mRNA stoichiometry was α:β:γ:δ = 10:1:1:1 by mass. Total amount of injected mRNA was 0.5–5 ng per cell for the wild type, 5–50 ng per cell for conventional mutations, and 25–125 ng per cell for suppression mutations. More mRNA was used in the double mutation experiments and with some mutations that gave abnormally low expression level. Equal volumes of the mRNA mixture and unprotected tRNA-amino acid were mixed prior to injection. Approximately 15ng of tRNA per cell was used in the single suppression experiments and 50 ng in the double suppression experiments. Each oocyte was injected with 50 nL of RNA solution, and cells were incubated for 18–72 hours at 18 °C in culture media ($ND96^+$ with 5% horse serum). In the case of low-expressing mutant receptors, a second injection was required. As a negative control for all suppression experiments, 76-nucleotide tRNA (dCA ligated to 74-nucleotide tRNA) was co-injected with mRNA in the same manner as fully charged tRNA.

Western blot analysis

The injected oocytes were incubated for 48 hours in $ND96^{+}$ with 5% horse serum. The vitelline/plasma membranes were isolated by physical dissection after the oocytes were incubated in hypotonic solution (5 mM HEPES, 5 mM NaCl) with 50 µL membrane solubilization solution (50 mM Tris, pH 7.5, 10 mM EDTA, 4% SDS w/v, 1mM phenanthroline, 10 µM pepstatin A) for 10 minutes. Following 5-minute centrifugation at 4 ºC and removal of the supernatant, the pellets were mixed with 10 µL smashing buffer (4.7 µL of exchange buffer (100 mM NaCl, 50 mM Tris, pH 7.9), 300 µL 10% SDS, 89 mg DDM, and 1 protease inhibitor tablet) and 10 µL of 2x loading buffer. The experiment was performed using SDS-PAGE with 15% Tris-Cl ReadyGels (BioRad Laboratories). 10 oocytes were used in each lane. The samples were subjected to a Western blot analysis using antihemagglutinin antibody, and visualized using an ECL detection kit (Amersham).

Electrophysiology

Acetylcholine chloride and succinylcholine dihydrate were purchased from Sigma-Aldrich/RBI. Drug dilutions were prepared from 1M stock solutions in the calcium-free ND96 buffer.

Ion channel function in oocytes was assayed by current recording in two-electrode voltage-clamp mode using the OpusXpress 6000A (Axon Instruments). For dose-response experiments, 1 mL of each drug solution was applied to the

cells, and between 12 and 16 concentrations of drug were used. Oocytes were clamped at −60 mV. Cells were perfused in calcium-free ND96 solution at flow rates of 1 mL/min before agonist application, 4 mL/min during agonist application, and 3 mL/min during wash. Drug application was 15 seconds in duration. Data were sampled at 125 Hz and filtered at 50 Hz.

Data Analysis

All dose-response data were obtained from at least 5 cells and at least two batches of oocytes. Data were normalized ($I_{max} = 1$) and averaged. EC_{50} and Hill coefficient (n_H) were determined by fitting averaged, normalized dose-response relations to the Hill equation. Dose-responses of individual oocytes were also examined and used to determine outliers. Individual dose-response data with $n_H > 2$ or $n_H < 1$ were discarded.

Coupling parameter (Ω) between any two mutations at residue 135 and 136 was calculated from Equation 1,

$$\Omega = [EC_{50}(\text{double mutation}) \times EC_{50}(\text{wild type})] / [EC_{50}(135 \text{ mutation}) \times EC_{50}(136 \text{ mutation})] \quad \text{(Eq.1)}$$

Side chain logP values were obtained using the ChemDraw program (CambridgeSoft Corporation).

Synthesis of Fmoc-Protected Amino Acid

Fmoc-Cl was purchased from Fluka. (*S*)-3-morpholinecarboxylic acid HCl was purchased from Tyger Scientific, Inc. (Ewing, NJ), (2*S*,3*S*)-3-methylpyrrolidine-2-carboxylic acid (3-Me-Pro) from Acros Organics USA (Morris Plains, NJ), α-methyl-*L*-proline (2-Me-Pro) from Fluka, and 3,4-dehydro-*L*-proline (Dhp) from Chem-Impex International, Inc. (Wood Dale, IL). The amino acids were coupled to the Fmoc protecting group using the following protocol.

L-amino acid (0.06 mmol) was dissolved in 10% Na_2CO_3 in water (2 mL), resulting in a solution with pH ~ 9. To this solution was added Fmoc-Cl (1.5 eq) in dioxane (2 mL) at room temperature. DIPEA was added dropwise while the reaction was stirred. Typically, the reaction was complete within 6 hours. The reaction mixture was diluted by addition of brine (20 mL). This was extracted with ether (5 mL) 5 times. The aqueous layer was acidified with 6 N HCl to pH of ~ 1 (solution became cloudy), and extracted with ether (5 mL) 3 times or until the organic layer was clear. The combined organic layers were dried over Na_2SO_4, and the solvent was removed under reduced pressure. Crude product was dried under vacuum overnight and was used in the next step (solid-phase peptide synthesis) without further purification.

***N*-Fmoc-2-methyl-proline.** ^{1}H NMR (500 MHz, $CDCl_3$) δ1.26–1.62 (m, 3H), 1.75–1.98, (m, 3H), 2.15–2.42 (m, 1H), 3.51–3.63 (m, 2H), 4.13–4.56 (m, 3H), 7.27–7.41 (m, 4H), 7.55–7.61 (m, 2H), 7.70–7.77 (m, 2H). ^{13}C NMR (125 MHz, $CDCl_3$) δ22.31, 22.72, 22.83, 23.42, 39.23, 41.11, 47.48, 47.58, 48.28, 48.91, 65.00, 66.28, 67.25, 67.65,

120.12, 120.20, 124.92, 124.95, 125.30, 125.35,127.27, 127.29, 127.30, 127.74, 127.78, 127.93, 141.54, 141.56, 141.60, 141.62, 144.05, 144.17, 144.21, 144.43, 154.86, 155.35, 178.42, 179.54. High-resolution MS analysis (FAB^+) calcd for $C_{21}H_{22}NO_4$ m/z = 352.1549, found 352.1534.

***N*-Fmoc-3-methyl-proline.** ^1H NMR (500 MHz, $CDCl_3$) δ1.17–1.28 (m, 3H), 1.49–1.63 (m, 1H), 2.01–2.15 (m, 1H), 2.40–2.49 (m, 1H), 3.50–3.68 (m, 2H), 3.85–3.97 (m, 1H), 4.12–4.28 (m, 1H), 4.33–4.46 (m, 2H), 7.27–7.40 (m, 2H), 7.53–7.62 (m, 2H), 7.69–7.77 (m, 2H). ^{13}C NMR (125 MHz, $CDCl_3$) δ18.65, 18.91, 31.58, 32.50, 38.24, 39.70, 45.92, 46.29, 47.27, 47.30, 65.59, 66.07, 67.72, 67.77, 119.94, 119.97, 120.04, 125.05, 125.11, 125.16, 125.24, 127.10, 127.13, 127.15, 127.68, 127.78, 127.79, 141.27, 141.34, 141.36, 141.39, 143.80, 143.84, 144.07, 144.12, 154.75, 155.46, 176.79, 177.69. ESI MS on an LCQ ion trap mass spectrometer (positive ion mode) calcd for $C_{21}H_{21}NO_4$ m/z = 351.1, found 351.9.

***N*-Fmoc-morpholine.** ^1H NMR (500 MHz, $CDCl_3$) δ3.04–3.92 (m, 6H), 4.20–4.68 (m, 5H), 7.27–7.34 (m, 2H), 7.36–7.42 (m, 2H), 7.48–7.60 (m, 2H), 7.71–7.77 (m, 2H). ^{13}C NMR (125 MHz, $CDCl_3$) δ41.16, 41.73, 47.27, 54.45, 54.84, 66.37, 66.75, 67.32, 67.72, 67.77, 68.12, 120.11, 120.14, 124.79, 124.89, 125.13, 127.19, 127.25, 127.27, 127.86, 127.90, 141.37, 141.42, 141.45, 141.48, 143.78, 143.82, 143.94, 155.91, 156.58, 174.83, 175.02. ESI MS on an LCQ ion trap mass spectrometer (positive ion mode) calcd for $C_{20}H_{19}NO_5Na$ m/z = 376.1, found 376.3.

Solid-phase peptide synthesis

All peptides were synthesized by solid-phase methods from Fmoc-protected amino acids using HBTU (Fluka) as a coupling reagent. Fmoc-*L*-proline (Fmoc-Pro) was purchased from Sigma, Fmoc-*L*-pipecolic acid (Fmoc-Pip) from Peptech Corporation (Burlington, MA), Fmoc-*L*-Azetidine-2-carboxylic acid (Fmoc-Aze) from Fluka, Fmoc-*cis*-2-fluoro-*L*-proline (Fmoc-*c*-4F-Pro) from AnaSpec, Inc. (San Jose, CA), *N*-Fmoc-glycine (Fmoc-Gly) from Aldrich, and Fmoc-*L*-phenylalanine (Fmoc-Phe) from Sigma. All chemicals were used as purchased without purification.

PAL resin (Sigma-Aldrich, estimated 0.4–0.8 mmol/g loading, 1 % cross-linked with divinylbenzene, 100–200 mesh) was used to afford carboxy terminal primary amides. For conventional amino acids, couplings were performed with 3 equivalents of Fmoc amino acid, 3 equivalents of HBTU, and 6 equivalents of diisopropylethylamine (DIPEA). For unnatural amino acids, couplings were performed with 2 equivalents of Fmoc amino acid, 2 equivalents of HBTU, and 4 equivalents of DIPEA. The reaction time for each coupling step was 1-2 hours. Kaiser test was performed to monitor the progress of the reaction. After each coupling step, unreacted free amine was acetylated (5% acetic anhydride and 5% pyridine, and 90% DMF) for 8 minutes, followed by deprotection of Fmoc-protected amine groups (20% piperidine/DMF, 15 minutes). In the last step, after Fmoc deprotection, the peptides were acetylated at the *N*-termini on the resin using a solution of 5% pyridine, 5% acetic anhydride, and 90% DMF. Peptides were cleaved from the resin by treatment with trifluoroacetic acid (TFA)

and water (95:5) for 2 hours. After filtration to collect the filtrate, solvents were removed as much as possible under reduced pressure. Following addition of 5% acetic acid solution, this solution was lyophilized to dryness. The peptides were purified by preparative-scale reversed-phase high-pressure liquid chromatography (HPLC) with gradient elution using an A-B gradient (buffer A 0.05% TFA in water; buffer B 20% water and 0.05% TFA in acetonitrile) and the flow rate of 15 mL/min. Peptide identity was characterized by ESI MS on an LCQ ion trap mass spectrometer (positive ion mode).

GFProG $(M+Na)^+$ expected 440.2, observed 440.3.

GF(2-Me-Pro)G $(M+Na)^+$ expected 454.2, observed 454.3.

GF(3-Me-Pro)G $(M+Na)^+$ expected 454.2, observed 454.4.

GF(*c*-4F-Pro)G $(M+Na)^+$ expected 458.2, observed 458.4.

GFAzeG $(M+Na)^+$ expected 426.2, observed 426.2.

GFPipG $(M+Na)^+$ expected 454.2, observed 454.3.

GFMorG $(M+Na)^+$ expected 456.2, observed 456.2.

Note that the synthesis of Gly-Phe-Dhp-Gly peptide did not give the desired product in the first trial, and no further attempt has been made to obtain the product.

NMR Spectroscopy of Model Peptides

The peptide samples were dissolved in 5mM phosphate buffer with 25 mM NaCl in 90% H2O/10% D2O at pH 5. Samples for NMR experiments were between 2 and 5 mM. NMR spectra were acquired on a Varian 600 MHz spectrometer, and the temperature was set to 298 K. The water signal was suppressed by presaturation. Sequential assignments were achieved using gradient selected correlated spectroscopy (gCOSY) and total correlation spectroscopy (TOCSY) experiments. Spectra were all internally referenced to 3-(trimethylsilyl) propionic-2,2,3,3-d_4 acid sodium salt (TSP, ~ 200 μM final concentration) at 0.0 ppm. The fraction of *cis* conformer was determined by integrating well-resolved peaks in the one-dimensional ^{1}H NMR spectra. NMR data were processed using the MestReNova software version 5.1.0 (Mestrelab Research S. L.).

2.6 Supplemental Figure

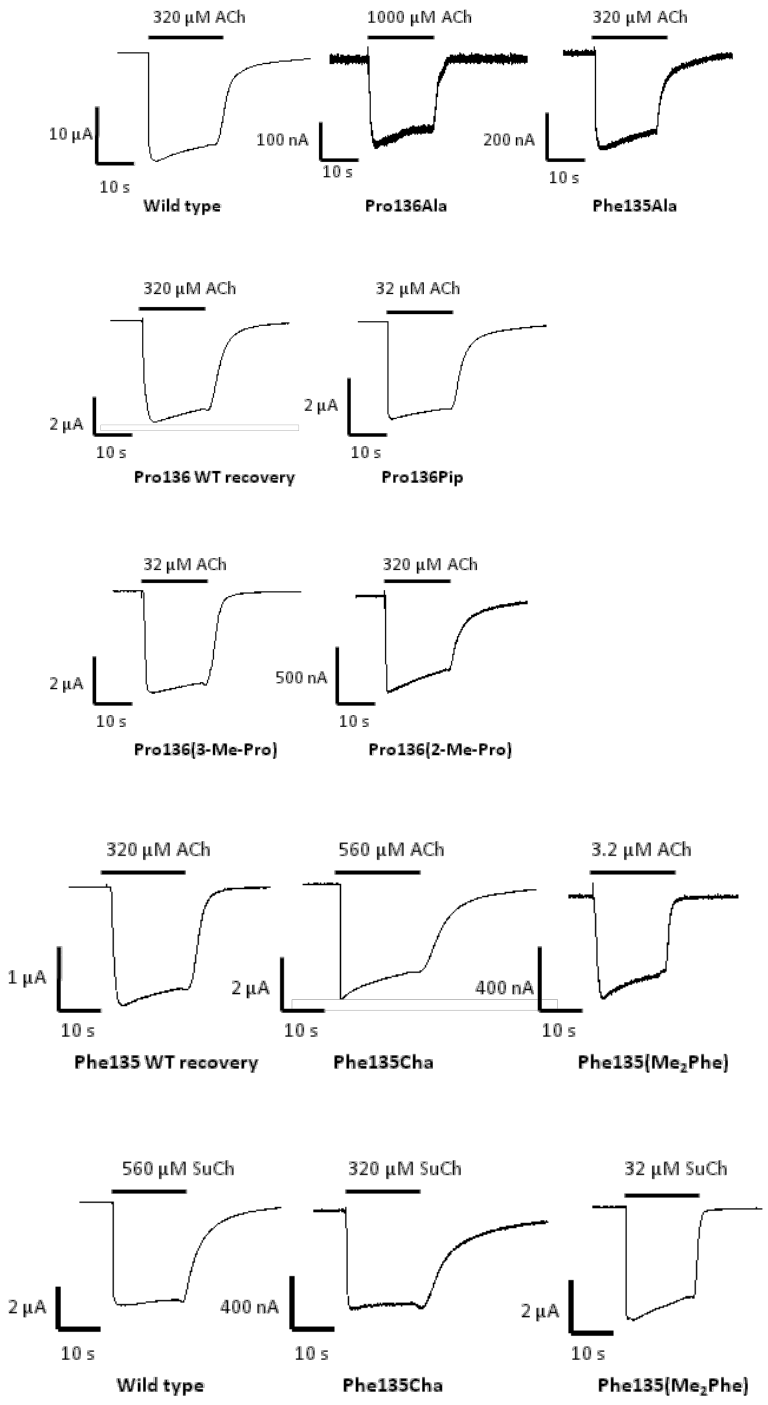

Figure 2.S1. Sample current traces from wild-type and mutant nAChR at saturating doses of ACh or SuCh

2.7 Acknowledgments

We thank Dr. Scott A. Ross for help with the NMR experiments and Professor Sarah C. R. Lummis for helpful discussion.

2.8 References

(1) Corringer, P. J.; Le Novère, N.; Changeux, J. P. Nicotinic receptors at the amino acid level. *Annu. Rev. Pharmacol. Toxicol.* **2000**, *40*, 431–458.

(2) Grutter, T.; Changeux, J. P. Nicotinic receptors in wonderland. *Trends Biochem. Sci.* **2001**, *26*, 459–463.

(3) Bouzat, C.; Gumilar, F.; Spitzmaul, G.; Wang, H. L.; Rayes, D.; Hansen, S. B.; Taylor, P.; Sine, S. M. Coupling of agonist binding to channel gating in an ACh-binding protein linked to an ion channel. *Nature* **2004**, *430*, 896–900.

(4) Karlin, A. Emerging structure of the nicotinic acetylcholine receptors. *Nat. Rev. Neurosci.* **2002**, *3*, 102–114.

(5) Lummis, S. C. R.; Beene, D. L.; Lee, L. W.; Lester, H. A.; Broadhurst, R. W.; Dougherty, D. A. Cis-trans isomerization at a proline opens the pore of a neurotransmitter-gated ion channel. *Nature* **2005**, *438*, 248–252.

(6) Millar, N. S. Assembly and subunit diversity of nicotinic acetylcholine receptors. *Biochem. Soc. Trans.* **2003**, *31*, 869–874.

(7) Jha, A.; Cadugan, D. J.; Purohit, P.; Auerbach, A. Acetylcholine receptor gating at extracellular transmembrane domain interface: the cys-loop and M2-M3 linker. *J. Gen. Physiol.* **2007**, *130*, 547–558.

(8) Dugave, C.; Demange, L. Cis-trans isomerization of organic molecules and biomolecules: implications and applications. *Chem. Rev.* **2003**, *103*, 2475–2532.

(9) Bhattacharyya, R.; Chakrabarti, P. Stereospecific interactions of proline residues in protein structures and complexes. *J. Mol. Biol.* **2003**, *331*, 925–940.

(10) MacArthur, M. W.; Thornton, J. M. Influence of proline residues on protein conformation. *J. Mol. Biol.* **1991**, *218*, 397–412.

(11) Pal, D.; Chakrabarti, P. Cis peptide bonds in proteins: residues involved, their conformations, interactions and locations. *J. Mol. Biol.* **1999**, *294*, 271–288.

(12) Reimer, U.; Scherer, G.; Drewello, M.; Kruber, S.; Schutkowski, M.; Fischer, G. Side-chain effects on peptidyl-prolyl cis/trans isomerisation. *J. Mol. Biol.* **1998**, *279*, 449–460.

(13) Deane, C. M.; Lummis, S. C. The role and predicted propensity of conserved proline residues in the 5-HT_3 receptor. *J. Biol. Chem.* **2001**, *276*, 37962–37966.

(14) Brejc, K.; van Dijk, W. J.; Klaassen, R. V.; Schuurmans, M.; van Der Oost, J.; Smit, A. B.; Sixma, T. K. Crystal structure of an ACh-binding protein reveals the ligand-binding domain of nicotinic receptors. *Nature* **2001**, *411*, 269–276.

(15) Unwin, N. Refined structure of the nicotinic acetylcholine receptor at 4Å resolution. *J. Mol. Biol.* **2005**, *346*, 967–989.

(16) Dellisanti, C. D.; Yao, Y.; Stroud, J. C.; Wang, Z.-Z.; Chen, L. Crystal structure of the extracellular domain of nAChR alpha1 bound to alpha-bungarotoxin at 1.94 Å resolution. *Nat. Neurosci.* **2007**, *10*, 953–962.

(17) Rickert, K. W.; Imperiali, B. Analysis of the conserved glycosylation site in the nicotinic acetylcholine receptor: potential roles in complex assembly. *Chem. Biol.* **1995**, *2*, 751–759.

(18) Hilf, R. J. C.; Dutzler, R. X-ray structure of a prokaryotic pentameric ligand-gated ion channel. *Nature* **2008**, *452*, 375–379.

(19) Bocquet, N.; Nury, H.; Baaden, M.; Le Poupon, C.; Changeux, J.-P.; Delarue, M.; Corringer, P.-J. X-ray structure of a pentameric ligand-gated ion channel in an apparently open conformation. *Nature* **2009**, *457*, 111–114.

(20) Hilf, R. J. C.; Dutzler, R. Structure of a potentially open state of a proton-activated pentameric ligand-gated ion channel. *Nature* **2009**, *457*, 115–118.

(21) Hibbs, R. E.; Gouaux, E. Principles of activation and permeation in an anion-selective Cys-loop receptor. *Nature* **2011**, *474*, 54–60.

(22) Fu, D. X.; Sine, S. M. Asymmetric contribution of the conserved disulfide loop to subunit oligomerization and assembly of the nicotinic acetylcholine receptor. *J. Biol. Chem.* **1996**, *271*, 31479–31484.

(23) Chakrapani, S.; Bailey, T. D.; Auerbach, A. Gating dynamics of the acetylcholine receptor extracellular domain. *J. Gen. Physiol.* **2004**, *123*, 341–356.

(24) McMenimen, K. A.; Dougherty, D. A.; Lester, H. A.; Petersson, E. J. Probing the Mg^{2+} blockade site of an N-methyl-D-aspartate (NMDA) receptor with unnatural amino acid mutagenesis. *ACS Chem. Biol.* **2006**, *1*, 227–234.

(25) Rodriguez, E. A.; Lester, H. A.; Dougherty, D. A. Improved amber and opal suppressor tRNAs for incorporation of unnatural amino acids in vivo. Part 1: minimizing misacylation. *RNA* **2007**, *13*, 1703–1714.

(26) Rodriguez, E. A.; Lester, H. A.; Dougherty, D. A. Improved amber and opal suppressor tRNAs for incorporation of unnatural amino acids in vivo. Part 2: evaluating suppression efficiency. *RNA* **2007**, *13*, 1715–1722.

(27) Kash, T. L.; Jenkins, A.; Kelley, J. C.; Trudell, J. R.; Harrison, N. L. Coupling of agonist binding to channel gating in the $GABA_A$ receptor. *Nature* **2003**, *421*, 272–275.

(28) Price, K. L.; Millen, K. S.; Lummis, S. C. R. Transducing agonist binding to channel gating involves different interactions in 5-HT_3 and $GABA_C$ receptors. *J. Biol. Chem.* **2007**, *282*, 25623–25630.

(29) Venkatachalan, S. P.; Czajkowski, C. A conserved salt bridge critical for $GABA_A$ receptor function and loop C dynamics. *Proc. Natl. Acad. Sci. U.S.A.* **2008**, *105*, 13604–13609.

(30) Gleitsman, K. R.; Kedrowski, S. M. A.; Lester, H. A.; Dougherty, D. A. An intersubunit hydrogen bond in the nicotinic acetylcholine receptor that contributes to channel gating. *J. Biol. Chem.* **2008**, *283*, 35638–35643.

(31) Lummis, S. C.; Beene, D. L.; Lee, L. W.; Lester, H. A.; Broadhurst, R. W.; Dougherty, D. A. Cis-trans isomerization at a proline opens the pore of a neurotransmitter-gated ion channel. *Nature* **2005**, *438*, 248–252.

(32) Wu, W.-J.; Raleigh, D. P. Conformational heterogeneity about pipecolic acid peptide bonds: conformational, thermodynamic, and kinetic aspects. *J. Org. Chem.* **1998**, *63*, 6689–6698.

(33) Sansom, M. S.; Weinstein, H. Hinges, swivels and switches: the role of prolines in signalling via transmembrane alpha-helices. *Trends Pharmacol. Sci.* **2000**, *21*, 445–451.

(34) Thomas, K. M.; Naduthambi, D.; Zondlo, N. J. Electronic control of amide cis-trans isomerism via the aromatic-prolyl interaction. *J. Am. Chem. Soc.* **2006**, *128*, 2216–2217.

(35) Sine, S. M.; Engel, A. G. Recent advances in Cys-loop receptor structure and function. *Nature* **2006**, *440*, 448–455.

(36) Paulsen, I. M.; Martin, I. L.; Dunn, S. M. J. Isomerization of the proline in the M2-M3 linker is not required for activation of the human 5-HT_{3A} receptor. *J. Neurochem.* **2009**, *110*, 870–878.

(37) Jabs, A.; Weiss, M. S.; Hilgenfeld, R. Non-proline cis peptide bonds in proteins. *J. Mol. Biol.* **1999**, *286*, 291–304.

(38) Cheng, X.; Ivanov, I.; Wang, H.; Sine, S. M.; McCammon, J. A. Nanosecond-timescale conformational dynamics of the human alpha7 nicotinic acetylcholine receptor. *Biophys. J.* **2007**, *93*, 2622–2634.

(39) Nowak, M. W.; Gallivan, J. P.; Silverman, S. K.; Labarca, C. G.; Dougherty, D. A.; Lester, H. A. In vivo incorporation of unnatural amino acids into ion channels in Xenopus oocyte expression system. *Methods Enzymol.* **1998**, *293*, 504–529.

(40) Cashin, A. L.; Torrice, M. M.; McMenimen, K. A.; Lester, H. A.; Dougherty, D. A. Chemical-scale studies on the role of a conserved aspartate in preorganizing the agonist binding site of the nicotinic acetylcholine receptor. *Biochemistry* **2007**, *46*, 630–639.

(41) Saks, M. E.; Sampson, J. R.; Nowak, M. W.; Kearney, P. C.; Du, F.; Abelson, J. N.; Lester, H. A.; Dougherty, D. A. An engineered Tetrahymena tRNAGln for in vivo incorporation of unnatural amino acids into proteins by nonsense suppression. *J. Biol. Chem.* **1996**, *271*, 23169–23175.

Chapter 3

Key Binding Interactions for Memantine in the *N*-Methyl-*D*-Aspartate Receptor[1]

3.1 Introduction

N-Methyl-*D*-aspartate (NMDA) receptors are members of the ionotropic glutamate receptor (iGluR) family, which also includes AMPA and kainate receptors (*1*-*3*). These are fast, excitatory, ligand-gated ion channels activated by the agonist glutamate and, only in the case of NMDA receptors, a co-agonist such as glycine or *D*-serine (*4*, *5*). The NMDA ion channel is highly permeable to Ca^{2+} and is blocked by Mg^{2+} in a voltage-dependent manner (*1*, *6*). The NMDA receptor is thought to play a central role in learning and memory and is essential to the normal function of the central nervous system (*7*, *8*). Overactivation of the receptor has been implicated in many neurological disorders, such as Alzheimer's disease, Parkinson's disease, Huntington's disease, amyotrophic lateral sclerosis, schizophrenia, epilepsy, and neurodegeneration following stroke (*2*, *9*–*11*). Several neuroprotective drugs have been developed to block the NMDA receptor, preventing overactivation. However, most of them cause

[1] This work was performed in collaboration with Wesley Yu and Emma Branigan as part of their Summer Undergraduate Research Fellowships at Caltech. A version of this chapter has been submitted for publication.

debilitating side effects due to the critical roles that NMDA receptors play in brain function (*12*).

Memantine (Namenda®) is the unique exception and is currently approved for use in moderate to severe Alzheimer's (*13*–*15*). Memantine is thought to function by preferentially blocking open NMDA channels (an uncompetitive antagonist) (*16*, *17*), and hence, a balance between open and closed channels can be achieved by adjusting dosage (*12*, *14*, *18*). The interaction between NMDA receptors and memantine is reversible, and the mechanism of block has not been fully elucidated (*19*).

In this study, we prepared mutants in the pore loop and the third transmembrane (TM3) domain of the GluN1/GluN2B NMDA receptor and measured how these side-chain modifications affect memantine block. Side-by-side comparison of the IC_{50} for memantine and amantadine (Figure 3.1), a structurally related drug, enabled us to identify the hydrophobic binding pockets for the two methyl groups on memantine. While adding two methyl groups to amantadine to produce memantine improved affinity greatly, we also found that adding a third methyl group to produce the symmetrical trimethylamantadine (TMAm) diminished affinity (Figure 3.1). Our results provide a better understanding of chemical-scale interactions between memantine and the ion pore of NMDA receptor, which will potentially benefit the development of new drugs for neurodegenerative diseases involving NMDA receptors.

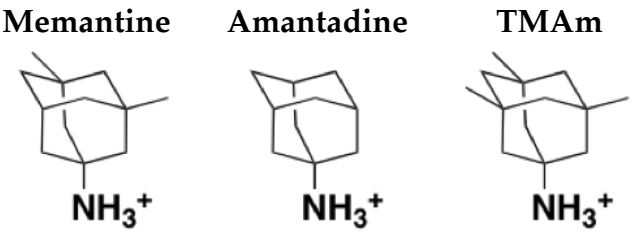

Figure 3.1. Structures of memantine, amantadine, and trimethylamantadine (TMAm)

3.2 Results

3.2.1 Homology models of GluN1 and GluN2B transmembrane domains

The structure of the transmembrane domain of the NMDA receptor is not currently available. It was proposed some time ago that the transmembrane domain of iGluRs is homologous to the pore region of potassium channels, but with the opposite orientation with respect to the membrane (*20*, *21*). This has been confirmed by a crystal structure of a full-length AMPA receptor (*22*), but unfortunately, the image is of a closed channel and is missing a significant number of residues in the pore loop. Therefore, we created a homology model of GluN1 and GluN2B transmembrane domains, based on the crystal structure of the open-form Kv2.1 paddle–Kv1.2 chimera potassium channel (Protein Data Bank code 2R9R) without any optimization (Figure 3.2) (*23*).

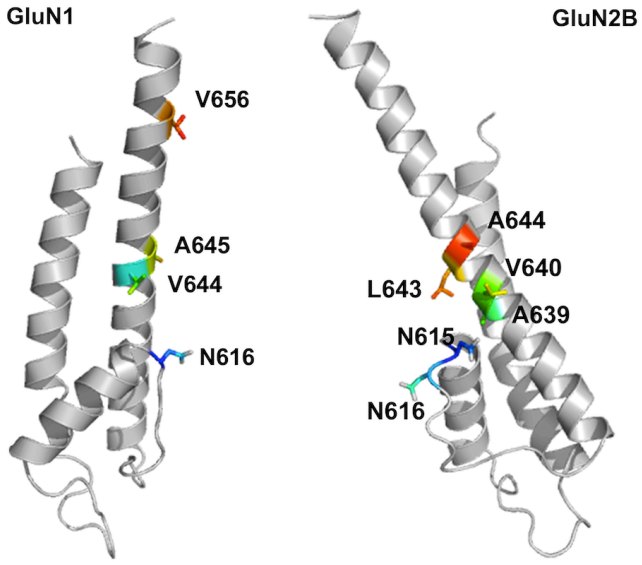

Figure 3.2. Homology model of the transmembrane region of GluN1 (*left*) and GluN2B (*right*) subunits of NMDA receptor. The relative position of the two subunits are currently unknown.

3.2.2 Mutational scanning

We first performed a mutational scanning on the pore loop, TM3, and post-TM3 regions of the GluN1/2B NMDA receptor using both conventional and unnatural amino acid mutagenesis. Mutations that shift the IC_{50} greater than 5 folds are deemed significant. The data suggest that no point mutation deeper in the pore than residue GluN1-N616 had a significant effect on memantine blockade, and only mutations at residues V644, A645, and V656 in the TM3/post-TM3 regions of GluN1 had a meaningful impact on the memantine block (Figure 3.3). These preliminary results provided the groundwork for further investigation.

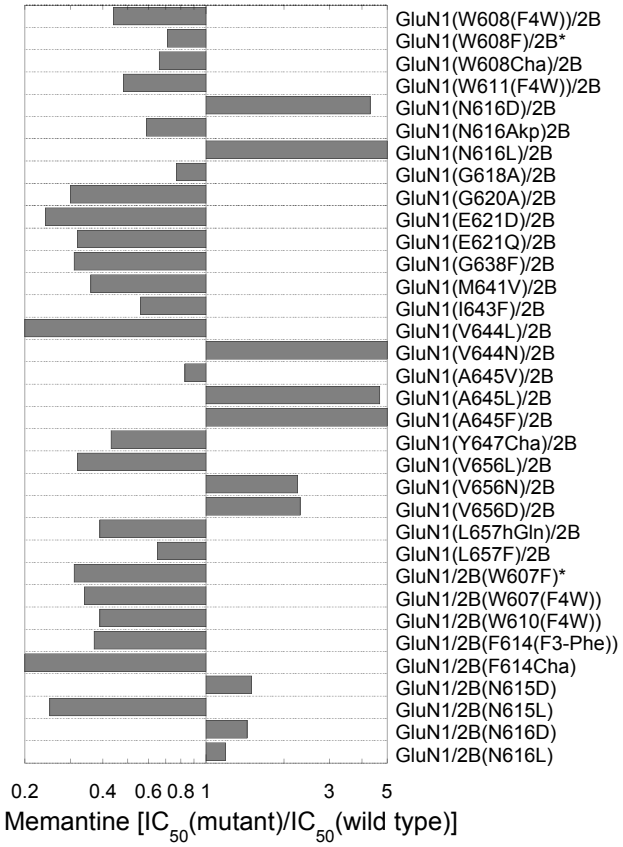

Figure 3.3. Memantine fold shifts (IC_{50}(mutant)/IC_{50}(wild type)) of mutant NMDA receptors containing a conventional or an unnatural mutation in the transmembrane region. Abbreviation used are F4W, 2,3,4,5-fluoro-Trp; Cha, cyclohexylalanine; hGln, homoglutamine; F3-Phe, 3,4,5-fluoro-Phe.
*, Conventional mutations performed through the nonsense-suppression method.

3.2.3 Comparison of memantine and amantadine block

In the present study, we sought to define the scope of the memantine primary binding site by identifying the residues that directly contact the two methyl groups (Figure 3.1). To probe for the methyl group binding pockets of memantine on the NMDA receptor, we considered amantadine, a common antiviral agent that is known to block the channel of NMDA receptors, but with a

lower affinity than memantine (*24*–*30*). Amantadine has the same basic core structure as memantine (Figure 3.3), the only difference being that amantadine lacks the two methyl groups present on memantine. Comparing memantine to amantadine, the affinity gained from the presence of the methyl groups is evaluated by IC_{50}(amantadine)/IC_{50}(memantine), referred to as the *methyl effect* throughout this chapter. In spite of the small structural difference, the affinity of memantine is 75-fold higher than amantadine in the wild-type receptor (Table 3.3, Figure 3.4), indicating that the two additional methyl groups play an important role in antagonism.

If these two antagonists bind at the same location and orientation in the NMDA channel pore, mutations at residues that interact with the methyl groups are expected to cause a larger IC_{50} shift for memantine than amantadine, thus, reducing the methyl effect. Smaller methyl effect means the mutant receptor is *less* sensitive toward the methyl group. Other mutations should affect binding of the two antagonists in a similar way. In fact, memantine and amantadine show similar responses to the GluN1(N616Q) and the GluN1(N616D) mutations (Figure 3.4) — a residue that is thought to anchor the ammonium group through an electrostatic interaction (*12*, *31*). Mutations at the analogous residues in GluN2, N615D and N616D, produce relatively modest effects (Figure 3.4). The GluN2(N615D) mutation is unique in that it affects amantadine binding more than memantine. All the data are consistent with the notion that the two drugs block the channel at the same general location.

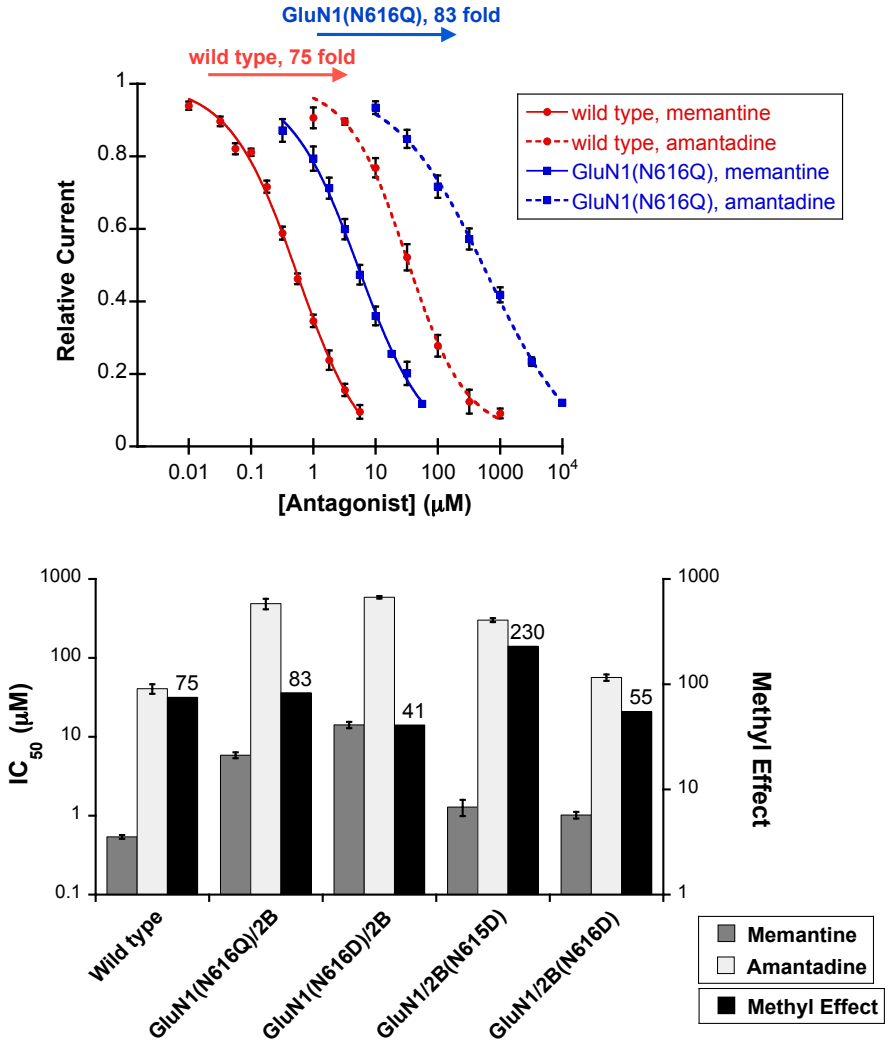

Figure 3.4. Memantine and amantadine dose response curves for the wild-type and the GluN1(N616Q) mutant NMDA receptors (*top*). The respective methyl effects are shown above the curves. Memantine IC_{50}, amantadine IC_{50}, and the methyl effect for wild-type and mutant NMDA receptors containing a mutation at GluN1-N616, GluN2B-N615, or GluN2B-N616 (*bottom*). The values for IC_{50} ± s.e.m. are shown in Table 3.3. The methyl effect values are shown above the corresponding columns.

3.3.4 Mapping the methyl group binding site on GluN1

Since we are probing for a hydrophobic binding pocket for the methyl groups, our strategy was to make hydrophobic side chains more hydrophilic.

Therefore, we mutated these three residues to Asn. The impact of mutations in the GluN1 subunit on IC_{50} values of both memantine and amantadine are shown in Figure 3.5 and Table 3.3.

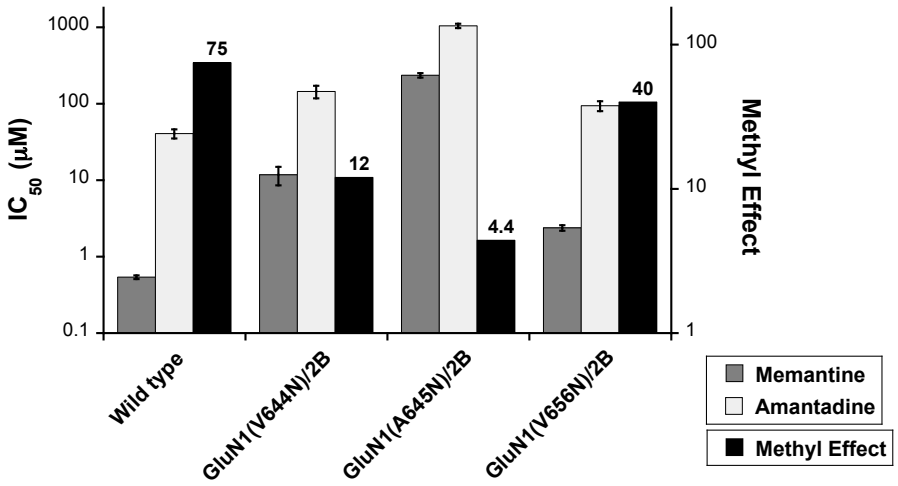

Figure 3.5. Memantine IC_{50}, amantadine IC_{50}, and the methyl effect for wild-type and mutant NMDA receptors containing a mutation at the residue V644, A645, or V656 in GluN1. The values for IC_{50} ± s.e.m. are shown in Table 3.3. The methyl effect values are shown above the corresponding columns.

The mutation V644N impacted the binding of memantine significantly more than amantadine. The IC_{50} ratio between the two drugs decreased to 12-fold, compared to the 75-fold effect seen in the wild-type receptor (Figure 3.5). The adjacent A645N mutation showed an even larger effect, with only a 4.4-fold difference between memantine and amantadine IC_{50}. The mutation V656N causes only a moderate 4.4-fold shift in IC_{50} for memantine and a modest 2.3-fold shift for amantadine. Interestingly, this mutation causes a nearly 10-fold shift in glutamate EC_{50} (Table 3.1), which may imply a strong perturbation to receptor gating.

Although the effects of Asn mutations at GluN1 residue 644 and 645 on glutamate EC_{50} were much smaller than the effects on blockage, the A645N mutation did show the significant reduction in Glu EC_{50}, approximately 6-fold (Table 3.1). In order to determine whether the V644N and A645N data in Figure 3.5 resulted from an unwanted structural perturbation, we tested V644T, V644L, A645V, and A645L mutations. All of these mutations shift glutamate EC_{50} less than A645N (Table 3.1). The additional mutations at residue 644 did not have a considerable impact on memantine IC_{50}, amantadine IC_{50}, or the ratio between the two (Table 3.3). Neither did the Val mutation at residue 645 (Figure 3.6, Table 3.3). In contrast, the A645L mutation had a significant impact on memantine IC_{50}, while essentially no effect is seen with amantadine IC_{50} (Figure 3.6, Table 3.3).

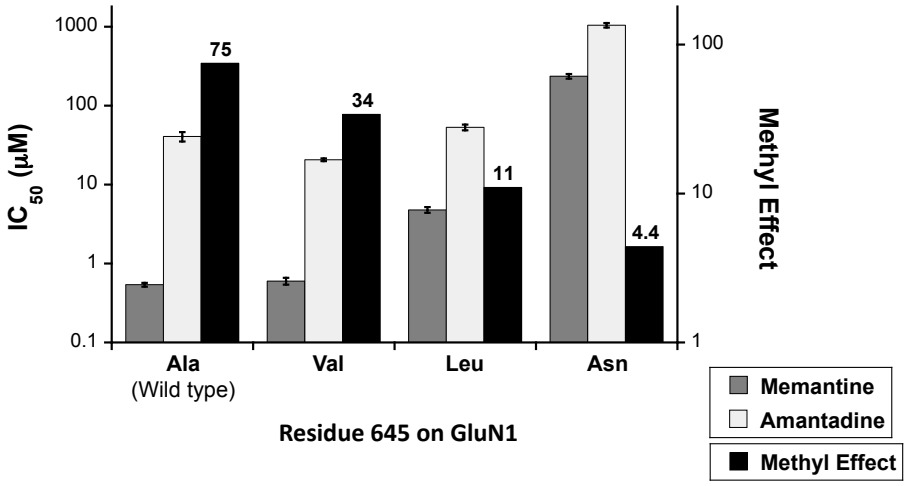

Figure 3.6. Memantine IC_{50}, amantadine IC_{50}, and the methyl effect for wild-type and mutant NMDA receptors containing a mutation at the residue GluN1-A645. The values for IC_{50} ± s.e.m. are shown in Table 3.3. The methyl effect values are shown above the corresponding columns.

A trend is seen in which the methyl effect is reduced with increasing the side-chain volume (Ala > Val > Leu) and side-chain polarity (Leu > Asn) at residue 645 (Figure 3.6). These results suggest that the residue A645 on GluN1 contributes to the methyl group binding site of memantine, while the residue V644 is located in close proximity.

3.3.5 Mapping the methyl group binding site on GluN2

Models of the NMDA receptor heterotetramer indicate that both GluN1 and GluN2 contribute to the channel region being probed. To probe for contributions to a methyl group binding site by GluN2B, however, it is not safe to assume that the residue GluN2-A644, which would typically be considered to align with GluN1-A645 (*21*, *32*), also contributes to a methyl group binding site. A previous study by the substituted cysteine accessibility method (SCAM) on GluN1/GluN2C suggests that there may be an offset by four residues in the TM3 regions between the GluN1 and GluN2C (*21*, *32*, *33*). Accordingly, we considered the aligning residues, L643 and A644, as well as the residues A639 and V640 which are one helix turn lower in the structure (Figure 3.2). The A639N and V640N mutations had a negligible effect on memantine and amantadine binding (Figure 3.7). In contrast, L643N and A644N substantially impaired memantine blockade. Similar to what is seen with GluN1, GluN2(L643N) shows a modest differentiation between memantine and amantadine, while GluN2(A644N) shows a quite substantial effect (Figure 3.7).

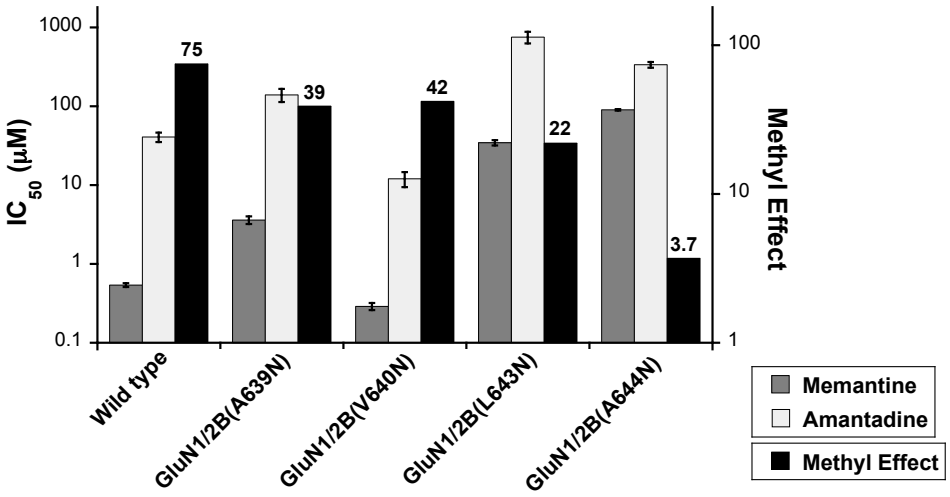

Figure 3.7. Memantine IC_{50}, amantadine IC_{50}, and the methyl effect for wild-type and mutant NMDA receptors containing an Asn mutation at the residue A639, A640, L643, and A644 in GluN2B. The values for IC_{50} ± s.e.m. are shown in Table 3.3. The methyl effect values are shown above the corresponding columns.

Parallel to the study in GluN1 subunit, we also mutated GluN2-A644 to the hydrophobic side chains Leu and Val. All these mutations resulted in minimal changes to glutamate EC_{50} (Table 3.1). Adding volume to this side chain (Ala > Val > Leu) lowered amantadine IC_{50} while leaving the memantine IC_{50} unaltered (Figure 3.8). Thus, the trend in the methyl effects is similar to that seen for mutations at GluN1-A645, in which there is a reduction in the methyl effect as the side-chain volume or the side-chain polarity is increased (Figure 3.8). Overall, these results suggest these two residues — GluN1-A645 and GluN2-A644 — play similar roles in shaping the memantine methyl binding site.

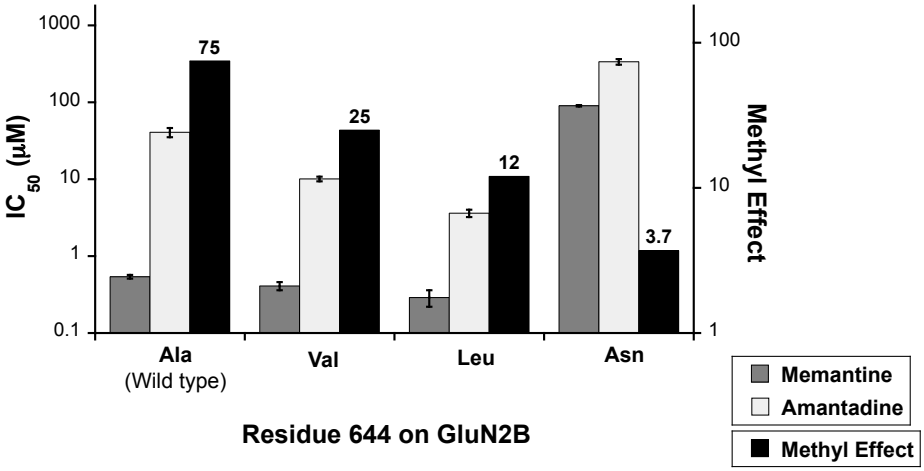

Figure 3.8. Memantine IC_{50}, amantadine IC_{50}, and the methyl effect for wild-type and mutant NMDA receptors containing a mutation at the residue GluN2B-A644. The values for IC_{50} ± s.e.m. are shown in Table 3.3. The methyl effect values are shown above the corresponding columns.

Table 3.1. Glutamate EC_{50} ± s.e.m. and Hill constant of wild-type and mutant NMDA receptors

NMDA Receptor	Glutamate EC_{50}	Hill Constant	*n*	EC_{50}(mutant)/EC_{50}(wild type)
	μM			
Wild type	1.94 ± 0.04	1.7	8	1.00
GluN1 Mutants				
N616Q	0.47 ± 0.01	1.6	11	0.24
N616D	1.3 ± 0.02	1.8	14	0.65
V644T	2.0 ± 0.03	1.6	11	1.01
V644L	1.3 ± 0.02	1.5	10	0.67
V644N	1.7 ± 0.03	1.6	12	0.89
A645V	0.93 ± 0.03	1.6	8	0.48
A645L	0.60 ± 0.02	1.3	9	0.31
A645N	0.33 ± 0.01	2.1	7	0.17
V656N	0.20 ± 0.01	2.3	7	0.10
GluN2B Mutants				
N615D	2.9 ± 0.06	1.7	5	1.01
N616D	2.8 ± 0.04	1.5	6	1.45
A639N	0.63 ± 0.02	1.5	9	0.32
V640N	2.8 ± 0.10	1.6	9	1.42
L643N	1.2 ± 0.03	1.5	9	0.64
A644V	0.61 ± 0.05	1.2	5	0.31
A644L	0.76 ± 0.05	1.5	11	0.39
A644N	0.73 ± 0.01	1.7	9	0.37

3.3.6 Investigating trimethylamantadine blockade

To further probe the possible role of methyl groups and asymmetry in the binding region, we considered the molecule trimethylamantadine (TMAm, Figure 3.1). The additional methyl group of TMAm introduces a 3-fold rotation axis that is absent in memantine. We found that this molecule blocks the NMDA receptor with an IC_{50} of 3.4 μM (Table 3.2), intermediate between the values for memantine (0.54 μM) and amantadine (41 μM). However, the GluN1(N616Q) mutation that displays a substantial shift in both memantine and amantadine IC_{50} does not have any effect on TMAm block (Table 3.2). Similarly, Asp mutation at GluN2-N615 or GluN2-N616 do not shift the TMAm IC_{50} from the wild-type value. TMAm is sensitive to GluN1(A645N) and GluN2(A644N) mutations, but the mutations have a significantly smaller effect on IC_{50} shifts for TMAm compared to memantine. These data imply that the TMAm molecule interacts with the ion pore in a different orientation than memantine and amantadine.

Table 3.2. TMAm IC_{50} ± s.e.m. for wild-type and mutant NMDA receptors

NMDA Receptor	TMAm IC_{50}	*n*	IC_{50}(mutant)/IC_{50}(wild type)
	μM		
Wild type	3.4 ± 0.4	10	1.0
GluN1(N616Q)/2B	2.0 ± 0.08	9	0.6
GluN1(V644T)/2B	3.1 ± 0.4	10	0.9
GluN1(A645N)/2B	180 ± 11	12	53
GluN1/2B(N615D)	5.4 ± 1.1	13	1.6
GluN1/2B(N616D)	2.9 ± 0.4	8	0.9
GluN1/2B(V640N)	0.72 ± 0.1	8	0.2
GluN1/2B(A644N)	100 ± 7.4	11	30

3.3 Discussion

Memantine is currently prescribed as a treatment for moderate to severe Alzheimer's disease (*13-15*), and the drug also displays clinical potential for treatment of other neurodegenerative disorders (*18*, *34*, *35*). Memantine is believed to function by blocking the NMDA receptor, a glutamate-gated ion channel in the brain, but the key binding interactions between drug and receptor are not fully elucidated (*16*, *17*, *19*). Further understanding of the chemical-scale interactions between the NMDA receptor and memantine will contribute some insight into the detailed mechanism of memantine blockade that underlies its high clinical potential.

Previous studies suggested that memantine can block the NMDA receptor at multiple sites, and the primary binding site (the one with the highest affinity or lowest IC_{50}) involves an interaction between the ammonium group of memantine and the side chain of an Asn residue (residue 616, the N/Q site) in the GluN1 subunit (Figure 3.2) (*12*, *31*). This residue is located at the tip of the pore loop, which forms the narrowest constriction of the NMDA pore (*1*, *20*, *21*). Our preliminary mutational scanning results suggest that no point mutation deeper in the pore than residue Asn616 had a significant effect on memantine blockade (Figure 3.3), consistent with a previous report that memantine cannot block NMDA receptors from the intracellular site (*36*). Furthermore, Kashiwagi et al. previously suggested that mutations at residues on the TM3 and post-TM3 regions of GluN1 had a considerable impact on memantine IC_{50}s (*37*). When we map these residues onto our homology model (Figure 3.2), we found some of

them to be distant from the Asn residue that anchors the ammonium of memantine. It seemed very unlikely that a small molecule like memantine would interact directly with all these residues. For these reasons, we aimed to search for the methyl group binding pockets that would serve as the definite upper boundary of the memantine primary binding site.

The highest memantine concentration used in all IC_{50} experiments was 100 μM to minimize complications involving the secondary (lower affinity) binding site (*12*, *29*, *30*, *38*) and/or antagonist trapping (*27*, *39*, *40*). Though this choice prevented completion of full dose-response curves for some mutations, meaningful IC_{50} values (unlike EC_{50} values) can be obtained from such plots. The EC_{50} for glutamate was measured for all the mutant receptors to ensure that (i) the mutant receptors are functional and (ii) a saturating dose of glutamate (4 or 10 μM) was applied to activate the mutant receptors in the IC_{50} experiments (Table 3.1).

In order to identify the residues that interact with the methyl groups, we employed a structurally related NMDA antagonist, amantadine, from which the methyl groups are absent. Mutations at the residues in contact with the methyl groups should have a larger effect on memantine affinity than amantadine, while other mutations should have a comparable effect on the two antagonists.

Probing wild-type vs. a mutant receptor with two different antagonists sets up an opportunity for a mutant cycle analysis as a way to evaluate meaningful interactions. The basic scheme is shown in Figure 3.9. The coupling parameter defines the deviation from additivity of the two "mutations": the change to the receptor and the removal of the methyl groups of memantine to

make amantadine. Significant coupling suggests an important interaction between the protein side chain being mutated and the methyl groups. The coupling parameter, Ω, can be converted to a free energy by the equation $\Delta\Delta G° = -RT\ln(\Omega)$. We consider meaningful interactions to have values of $\Omega \geq 3$ (or $\leq \frac{1}{3}$), corresponding to $|\Delta\Delta G°| > 0.6$ kcal/mol.

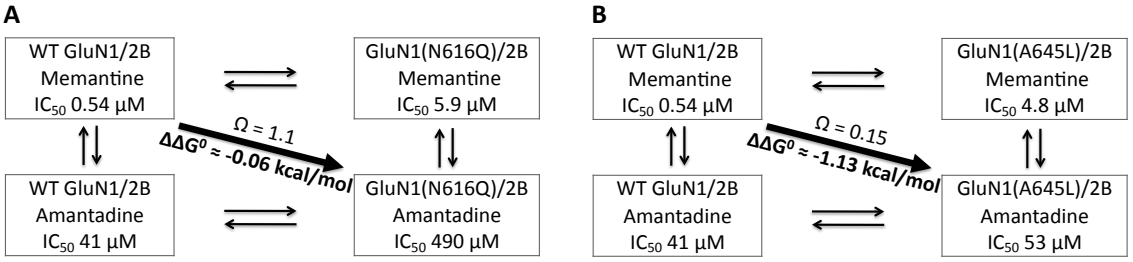

Figure 3.9. Examples of mutant-cycle analysis. **(A)** The GluN1(N616Q) mutation showed no coupling at all to the methyl groups of memantine, producing $\Omega \approx 1$ and $\Delta\Delta G° \approx 0$ kcal/mol. **(B)** The GluN1(A645L) mutation strongly coupled to the methyl groups as shown by the substantial coupling energy $\Delta\Delta G°$.

Memantine and amantadine show similar responses to the GluN1(N616Q) and GluN1(N616D) mutations, indicating that the two drugs block the channel at the same general location and with the same orientation (Figure 3.4). Stated differently, these two mutations, which are thought to probe the ammonium group binding site, show no significant coupling to the memantine/amantadine pair ($\Delta\Delta G° < 0.4$) (Table 3.3), which is a probe of methyl group binding. Therefore, comparison of the IC_{50} shifts between the two drugs is a valid strategy for probing the residues that are interacting with the methyl groups of memantine.

Table 3.3. Memantine and amantadine IC_{50} ± s.e.m., Ω, and ΔΔG° for wild-type and mutant NMDA receptors

NMDA Receptor	Memantine IC_{50}		Amantadine IC_{50}		Ω[a]	ΔΔG° [b]
	μM	*n*	μM	*n*		
Wild type	0.54 ± 0.03	18	41 ± 5.6	6		
GluN1 Mutants						
N616Q	5.9 ± 0.5	6	490 ± 73	10	1.1	−0.06
N616D	14 ± 1.3	7	590 ± 21	5	0.55	0.35
V644T	0.26 ± 0.06	13	44 ± 15	13	2.2	−0.48
V644L	0.26 ± 0.09	15	26 ± 6.5	11	1.3	−0.17
V644N	12 ± 3.2	7	150 ± 27	8	0.16	1.1
A645V	0.60 ± 0.06	9	21 ± 0.8	14	0.46	0.47
A645L	4.8 ± 0.4	9	53 ± 4.4	9	0.15	1.1
A645N	240 ± 16	11	1000 ± 68	11	0.06	1.7
V656N	2.4 ± 0.2	8	94 ± 14	7	0.53	0.38
GluN2B Mutants						
N615D	1.3 ± 0.3	7	300 ± 17	9	3.1	−0.67
N616D	1.0 ± 0.1	6	56 ± 5.3	10	0.74	0.18
A639N	3.6 ± 0.4	10	140 ± 26	11	0.51	0.39
V640N	0.29 ± 0.03	11	12 ± 2.6	8	0.55	0.35
L643N	34 ± 2.7	10	750 ± 130	13	0.29	0.73
A644V	0.41 ± 0.05	14	10. ± 0.7	11	0.33	0.66
A644L	0.29 ± 0.07	12	3.6 ± 0.4	12	0.17	1.0
A644N	90 ± 2.0	9	340 ± 29	10	0.05	1.8

[a] $\Omega = [(\text{wild-type memantine } IC_{50})*(\text{mutant amantadine } IC_{50})] / [\text{wild-type amantadine } IC_{50}) / (\text{mutant memantine } IC_{50})]$.
[b] $\Delta\Delta G° = R \bullet T \bullet \ln(\Omega)$ where R = 1.987 kcal•mol^{-1}•K^{-1} and T = 298 K.

The Asp mutation at GluN2B-N615, the residue that is considered to align with GluN1-N616, is the only mutation that affects amantadine binding more than memantine. This observation suggests an asymmetry in the region of the

ammonium group binding site such that the GluN1 subunit plays a more important role in memantine block, in agreement with previous proposals (*12*, *31*).

In GluN1, the V644N and A645N mutations, which displayed a large reduction in the methyl group effect from the wild type (Figure 3.5), produced a substantial ΔΔG° of 1.1 kcal/mol and 1.7 kcal/mol, respectively, (Table 3.3). A strong interaction between the side chain of the residue A645 and the methyl groups of memantine is indicated here, and the location of this residue relative to the residue GluN1-N616 on our homology model supports this finding (Figure 3.2). This is in an agreement with a previous study based on the SCAM showing that in the GluN1/GluN3 receptor, GluN1-A645 in the TM3 of the GluN1/GluN3 receptor is in a close proximity to the GluN1-N616 site (*41*). In contrary, the mutation V656N only produced a negligible ΔΔG° of 0.38 kcal/mol, suggesting that the effect of this mutation was not specific to the methyl groups on memantine.

The A645L mutation in GluN1, which had a significant impact on memantine IC_{50} but not amantadine IC_{50} (Figure 3.6), resulted in a significant ΔΔG° of 1.1 kcal/mol (Table 3.3). Since Leu and Ala are both hydrophobic, this could be considered a steric effect. When the methyl groups of memantine are present, a significant steric clash occurs when Ala is mutated to Leu. With amantadine, however, essentially no effect is seen. The lesser impact of the Val mutation, with ΔΔG° of 0.47 kcal/mol, is consistent with this analysis. Leu can be considered to be isosteric to Asn, and so the additional perturbation for the Asn mutation (ΔΔG° 1.7 kcal/mol) relative to Leu (ΔΔG° 1.1 kcal/mol) can be

considered a polarity effect. Both results are consistent with the notion that GluN1-A645 contributes to a hydrophobic binding pocket for the methyl groups on memantine.

To probe for contributions to a methyl group binding site by GluN2B, we considered the aligning residues, L643 and A644, as well as the residues A639 and V640 in order to address the possibility of the offset in the TM3 regions between the two subunits (Figure 3.2). Both A639N and V640N mutations resulted in a small perturbation to memantine and amantadine affinities and a negligible ΔΔG° value, whereas the L643N and A644N mutations produced a considerable effect. While GluN2B(L643N) showed a modest differentiation between memantine and amantadine and a ΔΔG° value of 0.73 kcal/mole, GluN2B(A644N) produced a large ΔΔG° value of 1.8 kcal/mol, comparable to what is seen with the GluN1(A645N) mutation. These data suggest that the offset in the TM3 region between GluN1 and GluN2B is minimal, consistent with a study of felbamate, an anticonvulsant drug that is structurally dissimilar to the antagonists studied here (*42*).

Mutating the residue GluN2B-A644 to Leu and Val produced the trend in ΔΔG° values that is very much parallel to that seen for the mutations at GluN1-A645. The large, polar residue Asn has the greatest effect; the isosteric but hydrophobic residue Leu has a smaller but still significant effect; the smaller hydrophobic residue Val has a small/negligible effect.

Overall, these results support a model in which the two residues — GluN1-A645 and GluN2-A644 — play similar roles in shaping the memantine

methyl binding site. However, there is an intriguing distinction between the two sites: the A645L mutation on GluN1 increases memantine IC_{50} and leaves amantadine IC_{50} unchanged (Figure 3.6), while the opposite is seen for the A644L mutation on GluN2B which shows no change in memantine IC_{50} and a lower amantadine IC_{50} than the wild type (Figure 3.8).

We have identified the hydrophobic binding pockets for the two methyl groups on memantine, which are located on the TM3 helices of the NMDA receptor and are formed by the residues A645 and A644 of GluN1 and GluN2B, respectively. Because these alanine residues are conserved in all the GluN2 subunits (GluN2A/B/C/D), it is possible that the methyl group binding pockets are the same for other GluN1/GluN2 receptor subtypes. These alanine residues are located immediately upstream to the SYTANLAAF motif, which has been implicated to play a crucial role in gating of the NMDA receptor (*43*–*45*).

Although we performed our experiments in a Mg^{2+}-free environment, it is worth noting that a decrease in the potencies of both memantine and amantadine has been reported in the presence of physiological concentrations of Mg^{2+} (*46*, *47*). This observation suggests a competitive behavior between memantine and Mg^{2+}, consistent with the notion that they share a common blocking location at the tip of the pore loop. The implication is that the primary binding site of memantine, including the methyl group binding pockets, possibly remains unchanged in the system with Mg^{2+}.

The two methyl groups on memantine are crucial for NMDA receptor blockade, increasing memantine affinity to the open NMDA receptor channel

and making it a much better neuroprotective drug than amantadine. We found that the molecule TMAm, which bears an additional methyl group compared to memantine, is also an antagonist to the NMDA receptor with an affinity between those of memantine and amantadine (Table 3.2). However, the TMAm block exhibited less sensitivity to the Asn mutations at GluN1-A645 or GluN2-A644 and was totally insensitive to the mutations GluN1(N616Q), GluN2(N615D), and GluN2(N616D) in the pore loop (Table 3.2). Altogether, our results suggest that the additional methyl group on TMAm prevents it from binding the receptor at the same location or orientation as memantine and amantadine.

In summary, our results indicate that the primary binding interaction of the methyl groups of memantine is formed by GluN1-A645 and GluN2-A644. Mutation at these residues had a significantly larger effect on memantine block compared to amantadine block. When coupled with the interaction between the ammonium group and GluN1-N616, a fairly precise model of memantine binding can be produced. Furthermore, the study of TMAm reveals that the special property of memantine as an NMDA receptor blocker stems not only from the presence of the additional hydrophobicity gained from the two methyl groups on the amantadine core but also a proper shape-matching to the binding site. Our findings provide further insight into the chemical-scale interaction between the NMDA receptor and memantine, hopefully contributing to efforts to understand the drug's high clinical potential and accelerate the development of other therapeutic NMDA receptor antagonists.

3.4 Materials and Methods

NMDAR Clones and Mutagenesis

The rat GluN1-1a and rat GluN2B cDNA clones were in pAMV vector. Mutant GluN1 and GluN2B subunits were prepared by site-directed mutagenesis using the standard Stratagene QuikChange protocol and verified through sequencing. All cDNA was linearized with NotI, and mRNA was synthesized by in vitro runoff transcription using the T7 mMESSAGE mMACHINE kit (Ambion).

Oocyte Expression

Stage V–VI *Xenopus* laevis oocytes (Nasco) were injected with 4–75 ng of mRNA in a total volume of 50 nL per oocyte. For some mutant receptors, second injection was necessary to attain sufficient current size, which was given 24 hours after the first injection. Oocytes were incubated in $ND96^{+}$ solution for 18 hours to 4 days after initial injection to achieve the optimal current size for the experiments.

Electrophysiological Recordings

Amantadine was purchased from Aldrich, memantine from Tocris Bioscience. Amantadine was stored as 1M stock solution and memantine as 100 mM stock solution in Millipore water at −80 °C. Glycine and *L*-glutamic acid

hydrochloride were purchased from Aldrich and were stored at −80 °C as 1M and 100 mM in Millipore water, respectively.

Macroscopic current recordings were made in two-electrode voltage-clamp mode using the OpusXpress 6000A (Molecular Devices). Voltage-sensing electrodes had a resistance of 0.3–10 MΩ, and current-injecting electrodes, 0.3–3 MΩ; all were filled with 3 M KCl. Oocytes were evaluated in a Mg^{2+} and Ca^{2+}-free saline solution (96 mM NaCl, 5 mM HEPES, 2 mM KCl, and 1 mM $BaCl_2$, pH 7.5). The receptors were activated in a Mg^{2+}- and Ca^{2+}-free solution containing 10 μM glycine and 20 μM glutamate. In the cases of GluN1(A645N) and GluN1(V656N) mutations, 10 μM glycine and 4 μM glutamate were used to activate the receptors to avoid overly saturated glutamate concentration.

To measure memantine IC_{50}, the mixture of glutamate and glycine was first applied through pump B. Memantine was then co-applied with the agonists for 50 seconds via a pipette tip, and after that, the agonists were applied again for 80 seconds through pump B. Then cells were later washed for 3 minutes in the Mg^{2+}- and Ca^{2+}-free ND96 solution. Similar protocol was used with amantadine but with different application durations: 35 seconds of the first agonist application, 30 seconds of amantadine applications, 45 seconds of the second agonist application, and 125 seconds of wash.

Up to eight oocytes were simultaneously voltage-clamped at −80 mV, and dose-response relationships were obtained by delivery of various drug concentrations in 1 mL aliquots.

Data analyses

All data were analyzed using the Clampfit 9.0 software (Axon). To determine IC_{50}, the fraction of block current (I/I_{max}) was determined for each test dose of antagonist, where I is the agonist-activated current measured in the presence of antagonist and I_{max} is the maximal current response to agonist activation. Then the I/I_{max} values were averaged for a given antagonist concentration, and the averages were fitted to the Hill equation. To determine EC_{50}, dose-response data were normalized to the maximal current (I_{max} = 1) and averaged. EC_{50} and Hill coefficient (n_H) were determined by fitting averaged, normalized dose-response relations to the Hill equation. All dose-response data were obtained from at least 5 cells and at least two batches of oocytes. Dose responses of individual oocytes were also examined and used to determine outliers.

3.5 Supplementary Figures

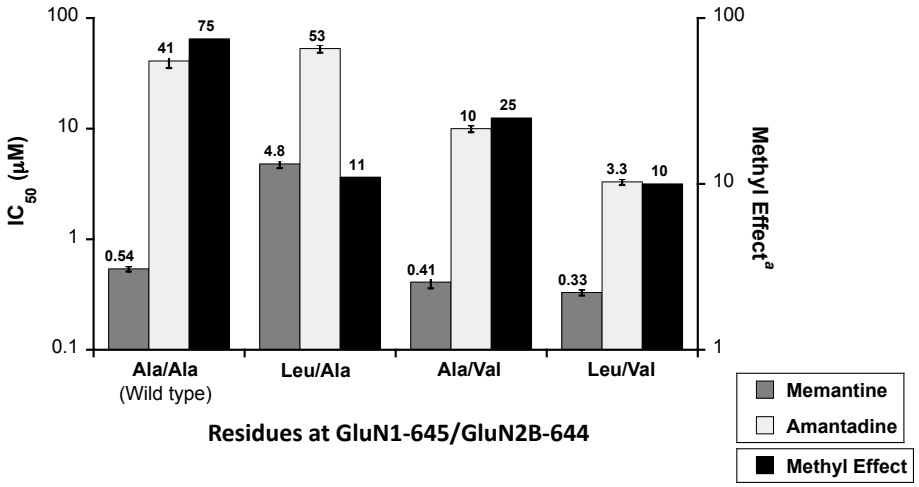

Figure 3.S1. Memantine IC_{50}, amantadine IC_{50}, and the methyl effect for double mutant GluN1(A645L)/2B(A644V) NMDA receptor in comparison with the values from the wild-type and the single-mutant receptors

3.6 References

(1) Dingledine, R.; Borges, K.; Bowie, D.; Traynelis, S. F. The glutamate receptor ion channels. *Pharmacol. Rev.* **1999**, *51*, 7–61.

(2) Madden, D. R. The structure and function of glutamate receptor ion channels. *Nat. Rev. Neurosci.* **2002**, *3*, 91–101.

(3) Traynelis, S. F.; Wollmuth, L. P.; McBain, C. J.; Menniti, F. S.; Vance, K. M.; Ogden, K. K.; Hansen, K. B.; Yuan, H.; Myers, S. J.; Dingledine, R. Glutamate receptor ion channels: structure, regulation, and function. *Pharmacol. Rev.* **2010**, *62*, 405–496.

(4) Moriyoshi, K.; Masu, M.; Ishii, T.; Shigemoto, R.; Mizuno, N.; Nakanishi, S. Molecular cloning and characterization of the rat NMDA receptor. *Nature* **1991**, *354*, 31–37.

(5) Nakanishi, N.; Axel, R.; Shneider, N. A. Alternative splicing generates functionally distinct N-methyl-D-aspartate receptors. *Proc. Natl. Acad. Sci. U.S.A.* **1992**, *89*, 8552–8556.

(6) Ascher, P.; Nowak, L. The role of divalent cations in the N-methyl-D-aspartate responses of mouse central neurones in culture. *J. Physiol. (London)* **1988**, *399*, 247–266.

(7) Kullmann, D. M.; Asztely, F.; Walker, M. C. The role of mammalian ionotropic receptors in synaptic plasticity: LTP, LTD and epilepsy. *Cell. Mol. Life Sci.* **2000**, *57*, 1551–1561.

(8) Liu, L.; Wong, T. P.; Pozza, M. F.; Lingenhoehl, K.; Wang, Y.; Sheng, M.; Auberson, Y. P.; Wang, Y. T. Role of NMDA receptor subtypes in governing the direction of hippocampal synaptic plasticity. *Science* **2004**, *304*, 1021–1024.

(9) Hollmann, M.; Heinemann, S. Cloned glutamate receptors. *Annu. Rev. Neurosci.* **1994**, *17*, 31–108.

(10) Malinow, R.; Mainen, Z. F.; Hayashi, Y. LTP mechanisms: from silence to four-lane traffic. *Curr. Opin. Neurobiol.* **2000**, *10*, 352–357.

(11) Cull-Candy, S.; Brickley, S.; Farrant, M. NMDA receptor subunits: diversity, development and disease. *Curr. Opin. Neurobiol.* **2001**, *11*, 327–335.

(12) Chen, H.-S. V.; Lipton, S. A. The chemical biology of clinically tolerated NMDA receptor antagonists. *J. Neurochem.* **2006**, *97*, 1611–1626.

(13) Witt, A.; Macdonald, N.; Kirkpatrick, P. Memantine hydrochloride. *Nat. Rev. Drug Discovery* **2004**, *3*, 109–110.

(14) Parsons, C. G.; Stöffler, A.; Danysz, W. Memantine: a NMDA receptor antagonist that improves memory by restoration of homeostasis in the glutamatergic system--too little activation is bad, too much is even worse. *Neuropharmacology* **2007**, *53*, 699–723.

(15) Wilkinson, D. A review of the effects of memantine on clinical progression in Alzheimer's disease. *Int. J. Geriatr. Psychiatry* **2012**, *27*, 769–776.

(16) Bormann, J. Memantine is a potent blocker of N-methyl-D-aspartate (NMDA) receptor channels. *Eur. J. Pharmacol.* **1989**, *166*, 591–592.

(17) Chen, H. S.; Pellegrini, J. W.; Aggarwal, S. K.; Lei, S. Z.; Warach, S.; Jensen, F. E.; Lipton, S. A. Open-channel block of N-methyl-D-aspartate (NMDA) responses by memantine: therapeutic advantage against NMDA receptor-mediated neurotoxicity. *J. Neurosci.* **1992**, *12*, 4427–4436.

(18) La Spada, A. Memantine strikes the perfect balance. *Nat. Med.* **2009**, *15*, 1355–1356.

(19) Johnson, J. W.; Kotermanski, S. E. Mechanism of action of memantine. *Curr. Opin. Pharmacol.* **2006**, *6*, 61–67.

(20) Kuner, T.; Seeburg, P. H.; Guy, H. R. A common architecture for K^+ channels and ionotropic glutamate receptors? *Trends Neurosci.* **2003**, *26*, 27–32.

(21) Wollmuth, L. P.; Sobolevsky, A. I. Structure and gating of the glutamate receptor ion channel. *Trends Neurosci.* **2004**, *27*, 321–328.

(22) Sobolevsky, A. I.; Rosconi, M. P.; Gouaux, E. X-ray structure, symmetry and mechanism of an AMPA-subtype glutamate receptor. *Nature* **2009**, *462*, 745–756.

(23) Long, S. B.; Tao, X.; Campbell, E. B.; Mackinnon, R. Atomic structure of a voltage-dependent K^+ channel in a lipid membrane-like environment. *Nature* **2007**, *450*, 376.

(24) Kornhuber, J.; Bormann, J.; Hübers, M.; Rusche, K.; Riederer, P. Effects of the 1-amino-adamantanes at the MK-801-binding site of the NMDA-receptor-gated ion channel: a human postmortem brain study. *Eur. J. Pharmacol.* **1991**, *206*, 297–300.

(25) Lupp, A.; Lücking, C. H.; Koch, R.; Jackisch, R.; Feuerstein, T. J. Inhibitory effects of the antiparkinsonian drugs memantine and amantadine on N-methyl-D-aspartate-evoked acetylcholine release in the rabbit caudate nucleus in vitro. *J. Pharmacol. Exp. Ther.* **1992**, *263*, 717–724.

(26) Parsons, C. G.; Quack, G.; Bresink, I.; Baran, L.; Przegalinski, E.; Kostowski, W.; Krzascik, P.; Hartmann, S.; Danysz, W. Comparison of the potency, kinetics and voltage-dependency of a series of uncompetitive NMDA receptor antagonists in vitro with anticonvulsive and motor impairment activity in vivo. *Neuropharmacology* **1995**, *34*, 1239–1258.

(27) Blanpied, T. A.; Boeckman, F. A.; Aizenman, E.; Johnson, J. W. Trapping channel block of NMDA-activated responses by amantadine and memantine. *J. Neurophysiol.* **1997**, *77*, 309–323.

(28) Blanpied, T. A.; Clarke, R. J.; Johnson, J. W. Amantadine inhibits NMDA receptors by accelerating channel closure during channel block. *J. Neurosci.* **2005**, *25*, 3312–3322.

(29) Antonov, S. M.; Johnson, J. W. Voltage-dependent interaction of open-channel blocking molecules with gating of NMDA receptors in rat cortical neurons. *J. Physiol. (London)* **1996**, *493 (Pt 2)*, 425–445.

(30) Sobolevsky, A. I.; Koshelev, S. G.; Khodorov, B. I. Interaction of memantine and amantadine with agonist-unbound NMDA-receptor channels in acutely isolated rat hippocampal neurons. *J. Physiol. (London)* **1998**, *512 (Pt 1)*, 47–60.

(31) Chen, H.-S. V.; Lipton, S. A. Pharmacological implications of two distinct mechanisms of interaction of memantine with N-methyl-D-aspartate-gated channels. *J. Pharmacol. Exp. Ther.* **2005**, *314*, 961–971.

(32) Sobolevsky, A. I.; Prodromou, M. L.; Yelshansky, M. V.; Wollmuth, L. P. Subunit-specific contribution of pore-forming domains to NMDA receptor channel structure and gating. *J. Gen. Physiol.* **2007**, *129*, 509–525.

(33) Sobolevsky, A. I.; Rooney, L.; Wollmuth, L. P. Staggering of subunits in NMDAR channels. *Biophys. J.* **2002**, *83*, 3304–3314.

(34) Lipton, S. A. Paradigm shift in neuroprotection by NMDA receptor blockade: Memantine and beyond. *Nat. Rev. Drug Discovery* **2006**, *5*, 160–170.

(35) Okamoto, S.-I.; Pouladi, M. A.; Talantova, M.; Yao, D.; Xia, P.; Ehrnhoefer, D. E.; Zaidi, R.; Clemente, A.; Kaul, M.; Graham, R. K.; Zhang, D.; Vincent Chen, H.-S.; Tong, G.; Hayden, M. R.; Lipton, S. A. Balance between synaptic versus extrasynaptic NMDA receptor activity influences inclusions and neurotoxicity of mutant huntingtin. *Nat. Med.* **2009**, *15*, 1407–1413.

(36) Parsons, C. G.; Gilling, K. E.; Jatzke, C. Memantine does not show intracellular block of the NMDA receptor channel. *Eur. J. Pharmacol.* **2008**, *587*, 99–103.

(37) Kashiwagi, K.; Masuko, T.; Nguyen, C. D.; Kuno, T.; Tanaka, I.; Igarashi, K.; Williams, K. Channel blockers acting at N-methyl-D-aspartate receptors: differential effects of mutations in the vestibule and ion channel pore. *Mol. Pharmacol.* **2002**, *61*, 533–545.

(38) Bresink, I.; Benke, T. A.; Collett, V. J.; Seal, A. J.; Parsons, C. G.; Henley, J. M.; Collingridge, G. L. Effects of memantine on recombinant rat NMDA receptors expressed in HEK 293 cells. *Br. J. Pharmacol.* **1996**, *119*, 195–204.

(39) Bolshakov, K. V.; Gmiro, V. E.; Tikhonov, D. B.; Magazanik, L. G. Determinants of trapping block of N-methyl-D-aspartate receptor channels. *J. Neurochem.* **2003**, *87*, 56–65.

(40) Mealing, G. A.; Lanthorn, T. H.; Small, D. L.; Murray, R. J.; Mattes, K. C.; Comas, T. M.; Morley, P. Structural modifications to an N-methyl-D-aspartate receptor antagonist result in large differences in trapping block. *J. Pharmacol. Exp. Ther.* **2001**, *297*, 906–914.

(41) Wada, A.; Takahashi, H.; Lipton, S. A.; Chen, H.-S. V. NR3A modulates the outer vestibule of the "NMDA" receptor channel. *J. Neurosci.* **2006**, *26*, 13156–13166.

(42) Chang, H.-R.; Kuo, C.-C. Molecular determinants of the anticonvulsant felbamate binding site in the N-methyl-D-aspartate receptor. *J. Med. Chem.* **2008**, *51*, 1534–1545.

(43) Chang, H.-R.; Kuo, C.-C. The activation gate and gating mechanism of the NMDA receptor. *J. Neurosci.* **2008**, *28*, 1546–1556.

(44) Yuan, H.; Erreger, K.; Dravid, S. M.; Traynelis, S. F. Conserved structural and functional control of N-methyl-D-aspartate receptor gating by transmembrane domain M3. *J. Biol. Chem.* **2005**, *280*, 29708–29716.

(45) Blanke, M. L.; VanDongen, A. M. J. The NR1 M3 domain mediates allosteric coupling in the N-methyl-D-aspartate receptor. *Mol. Pharmacol.* **2008**, *74*, 454–465.

(46) Otton, H. J.; Mclean, A. L.; Pannozzo, M. A.; Davies, C. H.; Wyllie, D. J. A. Quantification of the Mg^{2+}-induced potency shift of amantadine and memantine voltage-dependent block in human recombinant GluN1/GluN2A NMDARs. *Neuropharmacology* **2011**, *60*, 388–396.

(47) Kotermanski, S. E.; Johnson, J. W. Mg^{2+} Imparts NMDA Receptor Subtype Selectivity to the Alzheimer's Drug Memantine. *J. Neurosci.* **2009**, *29*, 2774–2779.

Chapter 4

Functional Crosstalk Between α6β4 Nicotinic Acetylcholine Receptors and P2X Receptors

4.1 Introduction

Nicotinic acetylcholine receptors (nAChRs) and P2X receptors are ligand-gated cation channels that mediate cholinergic and purinergic fast synaptic excitation in the nervous system. nAChRs are the member of the Cys-loop receptor family which includes 5-HT_3, $GABA_{A/C}$, and glycine receptors. Cys-loop receptors are composed of five subunits, and each subunit has four transmembrane domains and extracellular *N* and *C*-terminal tails (*1*). There are eight neuronal α (α2–α7, α9, α10) and three neuronal β (β2–β4) nAChR subunits in mammals (*2*). nAChRs are activated by the endogenous neurotransmitter acetylcholine (ACh) as well as nicotine, an alkaloid found in tobacco. P2X receptors belong to a different family of ligand-gated cation channels and are activated by extracellular ATP. The receptors are formed by 3 subunits, composed of one or a combination of the seven (P2X1–P2X7) subunits. Each subunit has two transmembrane domains and intracellular *N* and *C*-terminal tails (*3*).

P2X receptors and nAChRs are structurally different, and as such, they have been assumed to function independently. However, non-independent receptor function was demonstrated between ATP-gated channels and several members of the Cys-loop receptor family (*4–17*). Co-activation of P2X receptors and either nicotinic, serotonin 5-HT_3, or $GABA_{A/C}$ receptors, leads systematically to a cross-inhibitory interaction that translates into non-additivity of the recorded current (*4–17*). Because fast neurotransmitters such as ATP and ACh are co-released in the nervous system (*18–20*), the interactions between their respective receptor channels may play a critical role in shaping synaptic currents.

Dorsal root ganglia (DRG) contain neurons of the peripheral nervous system whose axons convey somatosensory information to the central nervous system (CNS). DRG neurons express a variety of nAChRs with a pharmacology consistent with α7, α3β4*, and α4β2* compositions (where the asterisks denote the possible presence of additional subunits) (*21–25*). Recently, α6β4* was found to be among the subtypes expressed by the DRG (*26*). Meanwhile, P2X2 and P2X3 subunits are heavily expressed in the DRG neurons, and three types of ATP-induced P2X currents were recorded that were consistent with the expression of the homomeric P2X3, homomeric P2X2, and heteromeric P2X2/3 receptors (*27*). The involvement of the ATP-gated receptors in the DRG neurons in nociception is well established.

Very recently, expression genetics and behavioral studies on mutant mice have revealed a negative correlation between expression of α6-nAChR subunit in the DRG neurons and allodynia (sensation of pain in response to a stimulus that

does not normally provoke pain).[1] The result suggests a functional interaction between α6-nAChRs and another pain relevant molecular target in the spinal cord or periphery. We therefore considered the hypothesis that α6β4* nAChRs interact functionally with P2X3 or P2X2/3 receptors, known to be involved in pain.

The present work is aimed to investigate the functional interactions between ATP-activated P2X receptors and α6β4* nAChRs that could potentially reveal a role of α6-nAChR in the anti-allodynic effect. Studies with recombinant nAChRs have identified only two subunit combinations of nAChRs thus far to contain a6 and β4 subunits: α6β4 and α6β4β3 (*28*–*30*). The stoichiometry of the α6β4 composition is currently unknown. β3 was found to assemble with α6 into nicotinic receptor pentamers at several locations in the brain, and only a single β3 subunit is incorporated into nAChR (*31*). β3 does not participate in forming the α:non-α interface that comprises the neuronal ligand-binding site, and other β subunits, either β2 or β4, must be present to form functional nicotinic receptors (*32*). Thus, the stoichiometry of the α6β4β3 composition is likely $(\alpha6)_2(\beta4)_2(\beta3)_1$.

Herein, we studied both the α6β4 and α6β4β3 combinations of nAChRs with three combinations of P2X receptors: homomeric P2X2, homomeric P2X3, and heteromeric P2X2/3 receptors. We report for the first time a functional crosstalk between α6β4* nAChR and P2X receptors in *Xenopus* oocytes. Further studies on the molecular mechanisms reveals two distinct classes of the interaction. The first class is inhibitory and only occurs during the receptor co-

[1] Jeffrey S. Wieskopf, Ardem Patapoutian, and Jeffrey S. Mogil. Personal Communication.

activation by both ACh and ATP. The second class of interaction is pre-organized and constitutive, in which a biophysical property of one channel is modulated by the other. Our finding supports the notion that the α6β4* nAChR may play a role in nociceptive signal transmission in DRG neurons through the cross interaction with P2X receptors.

4.2 Results

4.2.1 Expression of α6β4 and α6β4β3 nAChRs in *Xenopus* oocytes

Most α6-containing nAChRs yield very small agonist-induced currents in heterologous expression experiments, vitiating accurate measurements (*28*–*30*, *33*, *34*). We found that to be true for both α6β4* and α6β2* subtypes with human, rat and mouse α6 subunits. We overcame these problems by using a gain-of-function α6 subunit, α6(L9'S), for α6β4 expression (*35-38*), or a gain-of-function β3 subunit, β3(V13'S), for α6β4β3 expression (*31*, *38*). The wild-type α6β4 produced essentially no current when expressed in oocytes, even when co-expressed with P2X subunits (data not shown). Larger currents were observed from oocytes expressing α6β4β3(V13'S) than α6(L9'S)β4. However, the α6β4β3(V13'S) oocytes were less healthy, frequently displaying less negative resting potentials and larger leak currents when clamped at −60 mV. The leak current could be blocked by mecamylamine, a nicotinic antagonist, suggestive of constitutive activity from the α6β4β3(V13'S) receptor. The observation is

consistent with the spontaneous opening previously reported for the α6β4β3(V13'S) receptor (*38*).

4.2.2 Cross interaction between α6β4* and homomeric P2X2 receptors

While obtaining sufficient α6β4* currents from *Xenopus* oocytes was challenging, the expression of P2X2 receptor was very robust, frequently producing current > 20 μA. When we co-expressed P2X2 with α6(L9'S)β4 or α6β4β3(V13'S) in oocytes, we observed both ACh-evoked current (I_{ACh}) and ATP-evoked current (I_{ATP}) from the same cell. We found only minor (< 2-fold) changes in the EC_{50} values for both ACh and ATP when two types of receptors are co-expressed (Table 4.1). The presence of ATP had only a weak effect on the ACh dose-response relation, and *vice versa*.

As an initial step, we probed the interaction between the two types of receptors by applying a series of saturating doses of agonists in the following sequence: 100 μM ACh, 1 mM ATP, and 100 μM ACh + 1 mM ATP simultaneously. The resulting peak current observed during the co-application of ACh and ATP ($I_{ACh+ATP}$) was compared to the arithmetic sum of the individual ACh- and ATP-induced currents (I_{ACh} and I_{ATP}, respectively) at the same agonist concentrations on the same cell. If the two families of receptors are functionally independent, i.e., if there is no interaction between them, $I_{ACh+ATP}$ is expected to be identical to the predicted sum of I_{ACh} and I_{ATP} of the same cell.

Table 4.1. ACh dose-response results, with or without ATP, from oocytes expressing α6β4* alone or α6β4* with P2X2. ATP dose-response results, with or without ACh, from oocytes expressing P2X2 alone or α6β4* with P2X2

Receptor(s)	Dose-response	Additional Agonist	EC_{50}	Hill Constant	*n*
			μM		
α6(L9′S)β4	ACh		3.3 ± 0.11	1.4 ± 0.05	8
α6β4β3(V13′S)	ACh		1.3 ± 0.06	0.84 ± 0.03	10
P2X2	ATP		24 ± 1.2	1.5 ± 0.10	18
α6(L9′S)β4 + P2X2	ACh		4.3 ± 0.10	1.3 ± 0.03	11
	ACh	32μM ATP	4.5 ± 0.26	1.4 ± 0.09	14
	ACh	100μM ATP	6.0 ± 0.82	1.5 ± 0.23	14
	ATP		22 ± 1.1	1.6 ± 0.11	11
	ATP	100μM ACh	33 ± 3.6	1.3 ± 0.15	11
α6β4β3(V13′S) + P2X2	ACh		1.6 ± 0.09	0.84 ± 0.03	12
	ACh	32μM ATP	2.4 ± 1.1	0.75 ± 0.18	19
	ACh	100μM ATP	1.6 ± 0.45	0.67 ± 0.09	8
	ATP		23 ± 1.7	1.6 ± 0.15	11
	ATP	100μM ACh	24 ± 3.1	1.8 ± 0.35	12

In oocytes co-expressing P2X2−α6(L9′S)β4 or P2X2−α6β4β3(V13′S), we found that when 100 μM ACh and 1mM ATP were applied simultaneously, the total current was approximately 20% less than the sum of the currents elicited by the individual agonist at the same concentrations (Figure 4.1), which is the conventional definition of "cross inhibition." The difference between the predicted current and the observed $I_{ACh+ATP}$ is denoted Δ throughout this chapter. In the case of P2X2–α6(L9′S)β4 oocytes, the mean $I_{ACh+ATP}$ was only slightly larger than the mean I_{ATP} (Figure 4.1). Consequently, the mean Δ was nearly the size of

the average I_{ACh}. When the analogous experiments were performed on cells expressing only α6β4* or only P2X2, we found that ATP did not activate or modulate the α6(L9'S)β4 or α6β4β3(V13'S) nAChRs, and ACh did not activate or modulate the P2X2 receptors (data not shown). The current inhibition suggests that P2X2 and α6β4* receptors were functionally dependent when they were co-expressed, supporting the interaction between the two families of ligand-gated ion channels.

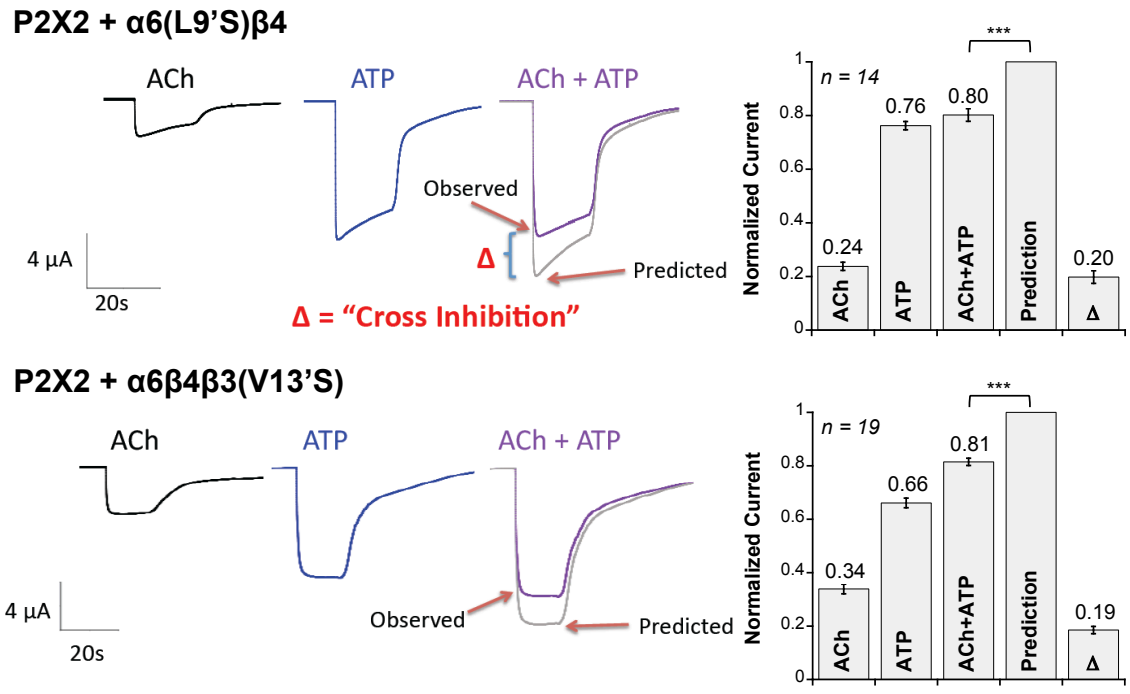

Figure 4.1. Functional interaction between α6β4* nAChRs and P2X2 receptor. Both P2X2–α6(L9'S)β4 oocytes (*top)* and P2X2–α6β4β3(V13'S) oocytes (*bottom)* displayed cross inhibition. Representative current traces from one cell in each case are shown. The predicted waveform is the point-by-point arithmetic sum of the I_{ACh} and I_{ATP} waveforms. Mean normalized currents ± s.e.m. are shown on the right. Δ is the difference between the prediction and the observed $I_{ACh+ATP}$. Currents were normalized to the prediction from the individual cell, and then averaged. ***, $p < 0.0001$.

From the current traces, we noticed that the oocytes expressing both P2X2 and α6(L9′S)β4 consistently produced ATP-evoked current with a sign of receptor desensitization unlike the oocytes expressing P2X2 alone (Figure 4.2) or the α6β4β3(V13′S)–P2X2 oocytes. This observation prompted us to speculate that the desensitized state of P2X2 could be involved in the functional interaction between α6(L9′S)β4 and P2X2 receptors. Further experiments were performed in order to investigate this hypothesis, as discussed later in this chapter.

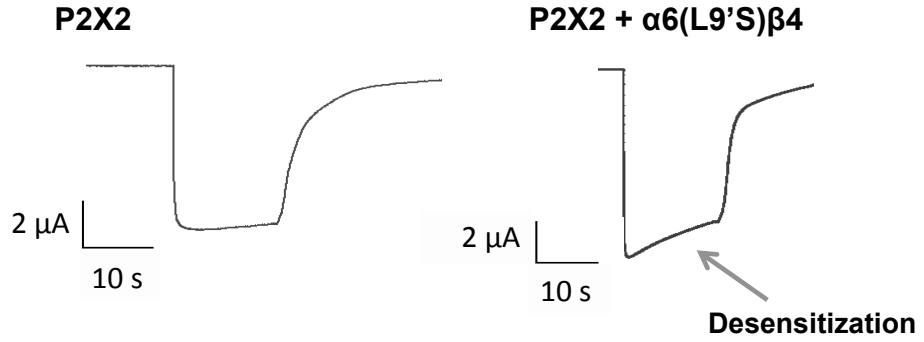

Figure 4.2. Apparent desensitization of ATP-evoked current from P2X2–α6(L9′S)β4. Representative current traces from oocyte expressing P2X2 only (*left*), and oocyte co-expressing α6(L9′S)β4 and P2X2 (*right*)

4.2.3 Cross interaction between α6β4* and homomeric P2X3 receptors

P2X3 receptor desensitizes very rapidly and recovers very slowly from the desensitized state, requiring > 30 minutes for a full recovery (*39*, *40*). Previous work reported that an arginine mutation at the Lys65 residue near the agonist-binding site slightly reduced the rate of desensitization and greatly enhanced the rate of current recovery for the P2X3 receptor expressed in HEK293 cells (*40*).

We mutated this lysine residue to Arg, Gln, Leu, and Ala, and we examined the current traces produced by these mutant receptors expressed in *Xenopus* oocytes. We finally decided to employ the K65A mutation, which produced the most consistent current level (data not shown), as a background mutation for all studies involving the P2X3 receptors. ATP EC_{50} of the P2X3(K65A) receptor was ~ 14 μM, approximately 5-fold higher than the wild-type value, which was reasonable as this residue is located near the ATP-binding site (*41*).

Even in the presence of the K65A mutation, the P2X3 receptors still open and close very rapidly. When ACh and ATP were co-applied to cells expressing α6β4* nAChR and P2X3(K65A), we observed two separate events of inward peak current, presumably arising first from P2X3(K65A) and then α6β4* nAChR openings. This means, most of the P2X3(K65A) receptors opened and desensitized before the opening of the nAChR reached its maximum. The fast desensitization kinetics of the P2X3(K65A) channels did not allow us to perform application of ACh and ATP at the same time, and therefore, the cross interaction protocol described for the P2X2 above could not be used here.

A different protocol was developed to evaluate the cross interaction between the P2X3(K65A) receptors and the α6β4* nAChR (Figure 4.3). ATP-evoked current when ATP was applied alone (I_{ATP}) was compared to the ATP-evoked current when 100 μM ACh was applied before ATP (I_{ATP}*). The difference between I_{ATP} and I_{ATP}* (Δ*) would directly indicate cross interaction between the two receptors.

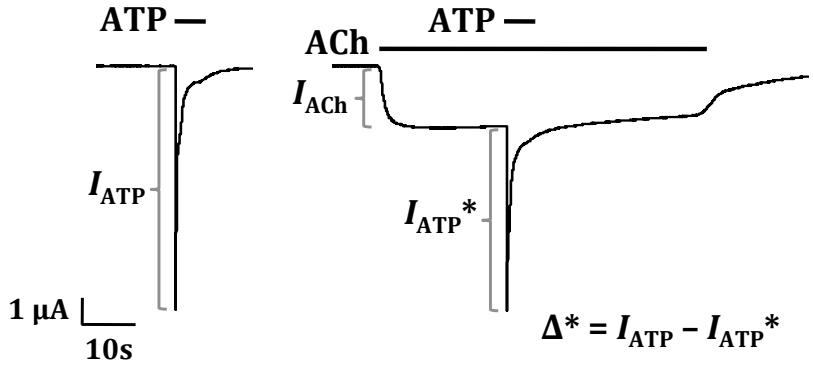

Figure 4.3. The protocol used for probing cross inhibition between α6β4* nAChR and fast-desensitizing P2X receptor. ATP was applied alone *or* after a pre-application of ACh. The resulting ATP-evoked currents from both cases were compared. Δ* is a measurement of cross inhibition.

At 100 μM ACh and 320 μM of ATP, cross inhibition was observed between α6(L9'S)β4 and P2X3(K65A) receptors, in which I_{ATP} was smaller than I_{ATP}* by 23% (Figure 4.4). Control experiments on cells injected with only P2X3(K65A) mRNA confirmed that ACh did not activate or modulate P2X3(K65A) receptors (data not shown). Cross interaction experiments between α6β4β3(V13'S) and P2X3(K65A) receptors were performed at 100 μM of both ACh and ATP. The observed inhibition was smaller than the case of P2X3(K65A)−α6(L9'S)β4, with ~ 17% current reduction from I_{ATP} to I_{ATP}* (Figure 4.4). Both the *p* value and Δ* are smaller than what we typically considered meaningful for establishing a receptor-receptor cross interaction. Thus, we cannot validate the functional interaction between α6β4β3(V13'S) and P2X3(K65A).

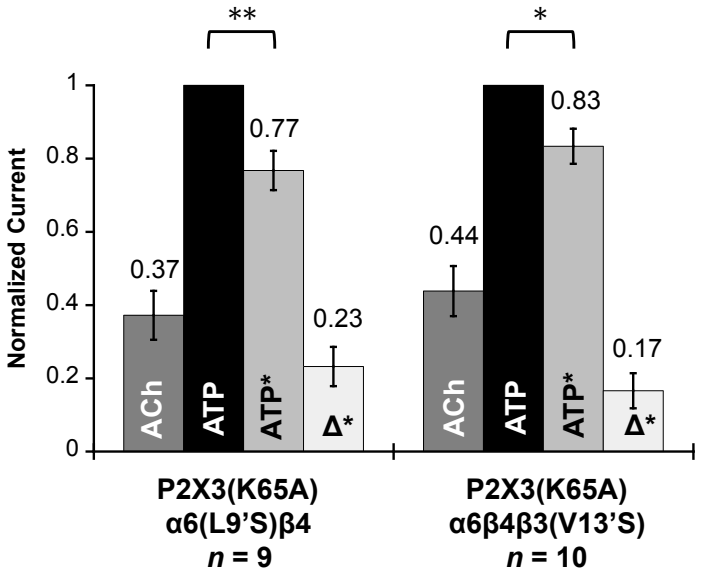

Figure 4.4. Cross inhibition between P2X3(K65A)–α6(L9′S)β4 and P2X3(K65A)–α6β4β3(V13′S). Δ* is the difference between I_{ATP} and I_{ATP}*. Currents were normalized to I_{ATP} from the individual cell, and then averaged. *, $p < 0.01$; **, $p < 0.005$.

In both P2X3(K65A)–α6(L9′S)β4 and P2X3(K65A)–α6β4β3(V13′S) cases, ACh-evoked current when ATP was pre-applied is essentially identical to the ACh-evoked current in the absence of ATP. This means the cross inhibition does not occur when P2X3(K65A) receptor is already desensitized (data not shown).

While co-expression of α6(L9′S)β4 and P2X3(K65A) did not change the ACh EC_{50}, we found that the co-expression caused a rightward shift in the ATP dose-response curve for the P2X3(K65A) receptor. The EC_{50} of the P2X3(K65A) receptor is approximately 3-fold higher, and the response has decreased apparent cooperativity, revealed by a reduced Hill coefficient (Figure 4.5). As a result, responses to ATP in the concentration range 10–100 μM are reduced by approximately half, when normalized to maximal responses. Furthermore, this

shift is independent of ACh (Figure 4.5). Co-expression of α6β4β3(V13'S) and P2X3(K65A) did not meaningfully change the EC_{50} of ACh (1.1 ± 0.10 μM, n = 7) or ATP (7.6 ± 0.33 μM, n = 11) compared to when each individual receptor was expressed alone (ACh EC_{50} 1.3 ± 0.06 μM, n = 10; ATP EC_{50} 13.6 ± 1.3 μM, n = 12).

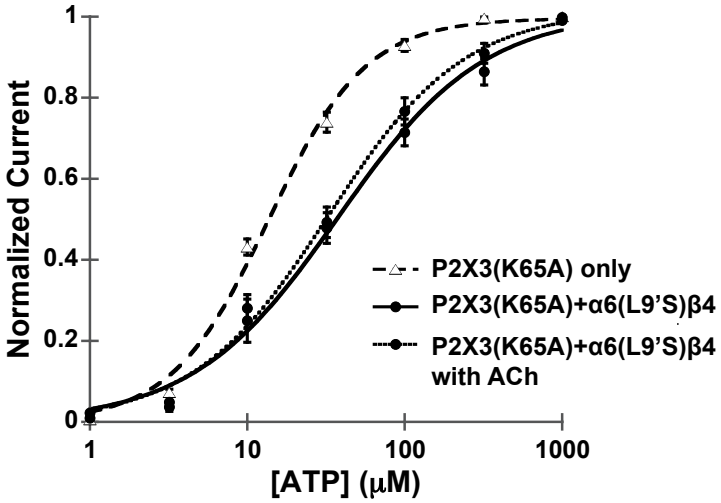

Figure 4.5. ATP dose-response curves for P2X3(K65A) oocytes (EC_{50} 13.6 ± 1.3 μM, Hill constant 1.4 ± 0.16, n = 12), P2X3(K65A)–α6(L9'S)β4 oocytes in the absence of ACh (37.8 ± 6.1 μM, Hill constant 0.94 ± 0.11, n = 14) and in the presence of 100 μM ACh (32.8 ± 5.0 μM, Hill constant 1.0 ± 0.12, n = 11)

Concerning with the accuracy of measuring the fast-desensitizing current, we sought a positive control. Having established that the wild-type P2X2 and the α6(L9'S)β4 receptors interact functionally, we performed parallel experiments on a fast-desensitizing P2X2(T18A) mutant receptor to confirm the validity of our measurement. This alanine mutation at Thr18, which is a phosphorylation site near the *N*-terminus of P2X2, was previously reported to drastically increase the rate of receptor desensitization, producing an apparently similar current trace to

the P2X3 current (*42–44*). Another previous study showed that the fast-desensitizing P2X2(T18A) receptor exhibited the cross-inhibition behavior with α3β4 nAChR similar to the wild-type P2X2 receptor (*41*), suggesting that the mutation did not interfere with the interaction between the P2X receptor and the nAChR.

At saturating concentrations of ATP (1 mM) and ACh (100 μM), we observed cross inhibition between α6(L9'S)β4 and P2X2(T18A), using the same protocol as the P2X3(K65A) experiment. The ATP-evoked current was 28% smaller in the presence of ACh (Figure 4.6A). We also found that the P2X2(T18A) receptor produced an ATP dose-response relation that is similar to the wild-type P2X2 receptor, despite very different desensitizing kinetics (Figure 4.6B). In contrast to what was seen with the P2X3(K65A), co-expressing the α6(L9'S)β4 receptor with the P2X2(T18A) receptor did not affect the ATP EC_{50} (Figure 4.6), which is consistent with the results from the wild-type P2X2 receptor shown in Table 4.1. The data confirm the validity of our protocol for probing fast-desensitizing current, and the rightward shift in the ATP dose-response curve is specific to the interaction between P2X3(K65A) and α6(L9'S)β4.

Overall, the results support the functional interaction between α6(L9'S)β4 and the P2X3(K65A) receptors. At saturated concentration of ATP, reduction in ATP-evoked current was observed in the presence of ACh, indicating a cross inhibition. We did not observe any cross inhibition when P2X3(K65A) was already desensitized. Moreover, oocytes co-expressing α6(L9'S)β4 and P2X3(K65A)

exhibited lower ATP sensitivity in relation to the oocytes expressing P2X3(K65A) alone, independent of α6(L9'S)β4 activation by ACh. In contrast, the interaction between α6β4β3(V13'S) and the P2X3(K65A), if it exists, is much weaker and is *not* firmly established by our data.

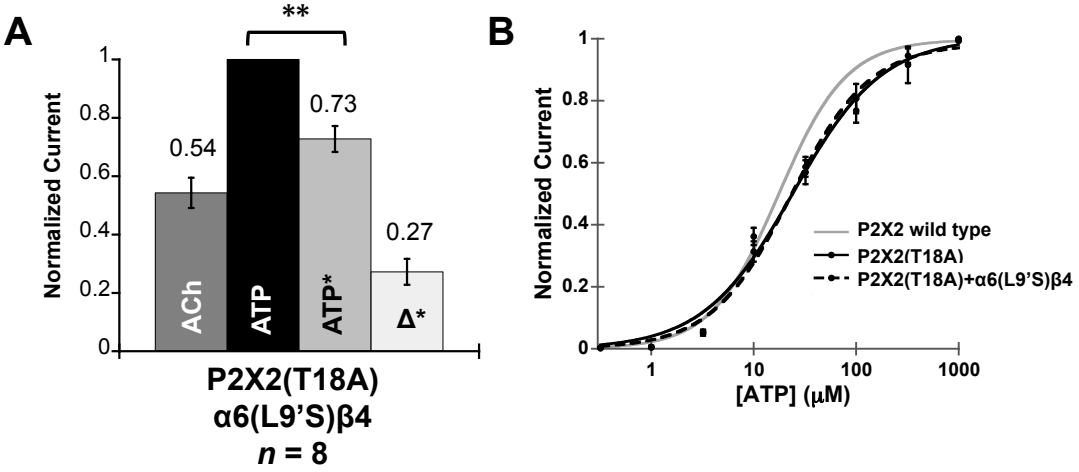

Figure 4.6. Functional interaction between P2X2(T18A) and α6(L9'S)β4. **(A)** Cross inhibition was observed between P2X2(T18A) and α6(L9'S)β4. Δ* is the difference between I_{ATP} and I_{ATP}*. Currents were normalized to I_{ATP} from the individual cell, and then averaged. **, $p < 0.005$. **(B)** ATP dose-response curves for wild-type P2X2 oocytes (EC_{50} 23.9 ± 1.5 μM, Hill constant 1.5 ± 0.10, n = 18), P2X2(T18A) oocytes (24.1 ± 4.8 μM, Hill constant 1.0 ± 0.15, n = 11), and P2X2(T18A)–α6(L9'S)β4 oocytes (22.9 ± 2.7 μM, Hill constant 1.1 ± 0.12, n = 11). Only the curve fit is shown for the wild-type P2X2 oocytes for clarity.

4.2.4. Cross inhibition between α6β4* and heteromeric P2X2/3 receptors

Co-injecting a mixture of P2X2 and P2X3 mRNA into oocytes is known to produce the heteromeric P2X2/3 receptor, along with the homomeric P2X2 and P2X3 receptors (*45*). To exclusively differentiate the P2X2/3 current, we used the

agonist α,β-methylene-ATP (αβmeATP), an ATP analog known to selectively activate the P2X3 and P2X2/3 receptor populations. We employed the wild-type P2X3 subunit, not the K65A mutant, to produce the heteromeric P2X2/3 receptor. The current signal from the homomeric P2X3 receptor was minimized by its intrinsically rapid desensitization. In oocytes co-injected with P2X2 and P2X3 mRNAs, αβmeATP-evoked current traces were distinct from what was seen for the P2X3 oocytes, displaying slower apparent desensitization kinetics. The mRNA injection ratio could be adjusted to favor more heteromeric P2X2/3 receptor expression relative to P2X3 (Figure 4.7C). Nearly pure αβmeATP-evoked current from the P2X2/3 receptors was obtained at the 1:10 P2X2:P2X3 injection ratio by mass; the fast-desensitizing current characteristic of P2X3 was absent (Figure 4.7). Therefore, this was the mRNA ratio used in all studies involving P2X2/3.

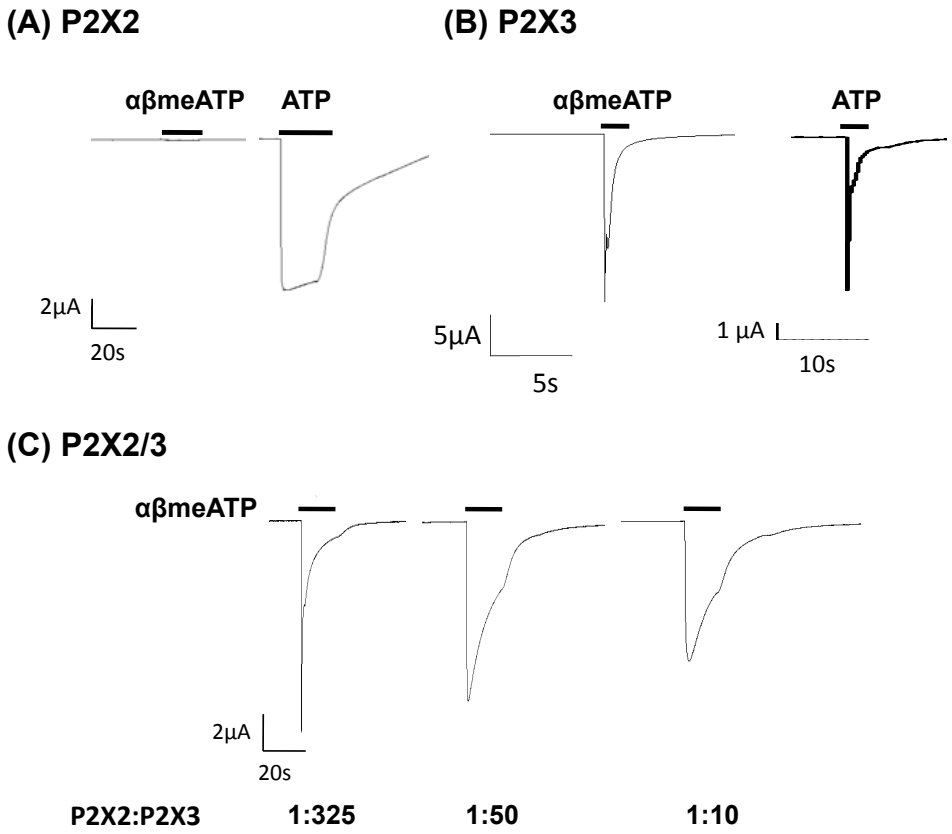

Figure 4.7. Representative current traces as a result of P2X receptor activation by αβmeATP. (A) αβmeATP application did not produce any current in oocytes expressing P2X2 alone. (B) αβmeATP activated the P2X3 receptor, and the current traces show rapid opening and desensitization similar to what was seen when the receptor was activated by ATP. (C) αβmeATP-evoked current traces from oocytes expressed with P2X2 and P2X3 at three different mRNA injection ratios are shown. The heteromeric P2X2/3 receptor desensitizes *less* than the homomeric P2X3 receptor. The P2X2:P2X3 mRNA ratios (by mass) are indicated below the traces.

The heteromeric P2X2/3 receptors produced current traces with a reasonably normal rate of desensitization, permitting us to investigate the cross interaction by simultaneous application of ACh and αβmeATP. Cross-inhibitory behavior was observed when P2X2/3 was co-expressed with α6(L9'S)β4 or α6β4β3(V13'S). In both cases, the current observed when 100 μM αβmeATP and

100 μM ACh were co-applied ($I_{ACh+\alpha\beta_{meATP}}$) was diminished by ≥ 20% compared to the predicted value based on the individual agonist applications (Figure 4.8). Control experiments showed that ACh did not activate or modulate the P2X2/3 receptors in oocytes without α6β4* nAChR. The results support the functional interaction between the α6β4* nAChRs and the heteromeric P2X2/3 receptor.

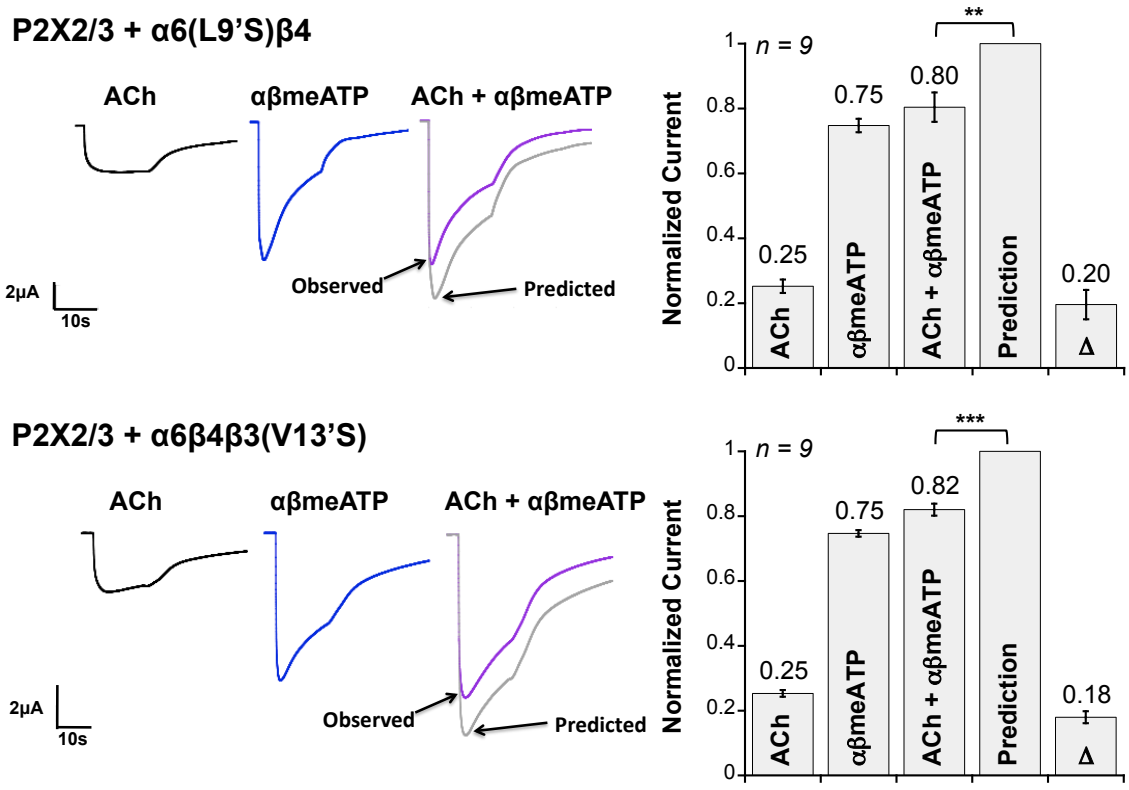

Figure 4.8. Functional interaction between α6β4* nAChRs and P2X2/3 receptor. Both P2X2/3–α6(L9'S)β4 oocytes (*top)* and P2X2/3–α6β4β3(V13'S) oocytes (*bottom)* show cross inhibition. Representative current traces from one cell in each case are shown. The predicted waveform is the point-by-point arithmetic sum of the $I_{\alpha\beta_{meATP}}$ and I_{ACh} waveforms. Mean normalized currents ± s.e.m. are shown on the right. Δ is the difference between the prediction and the observed $I_{ACh+\alpha\beta_{meATP}}$. Currents were normalized to the prediction from the individual cell, and then averaged. **, $p < 0.005$; ***, $p < 0.0001$.

4.2.5 Role of P2X *C*-terminal domains in the cross inhibition

The *C*-terminal domains of P2X2 and P2X3 were previously shown to be crucial for the cross interaction of P2X2 with 5-HT_{3A} receptor, α4β3 nAChR, or $GABA_C$ receptor (*4*, *6*, *7*). To investigate the importance of this domain in the interaction with α6β4* nAChRs, we removed the *C*-terminal tails from both P2X2 and P2X3(K65A) subunits (see materials and methods). The truncated P2X2 and P2X3(K65A) subunits are denoted as P2X2TR and P2X3(K65A)TR, respectively.

Similar to what was seen with the full-length P2X2 receptor, in both α6(L9'S)β4–P2X2TR oocytes and α6β4β3(V13'S)−P2X2TR oocytes, we observed the mean $I_{ACh+ATP}$ values that were ~ 20% smaller than the predicted values (Figure 4.9). These results suggest that the *C*-terminal tail of P2X2 is not required for the functional interaction between the P2X2 receptor and the α6β4* nAChRs.

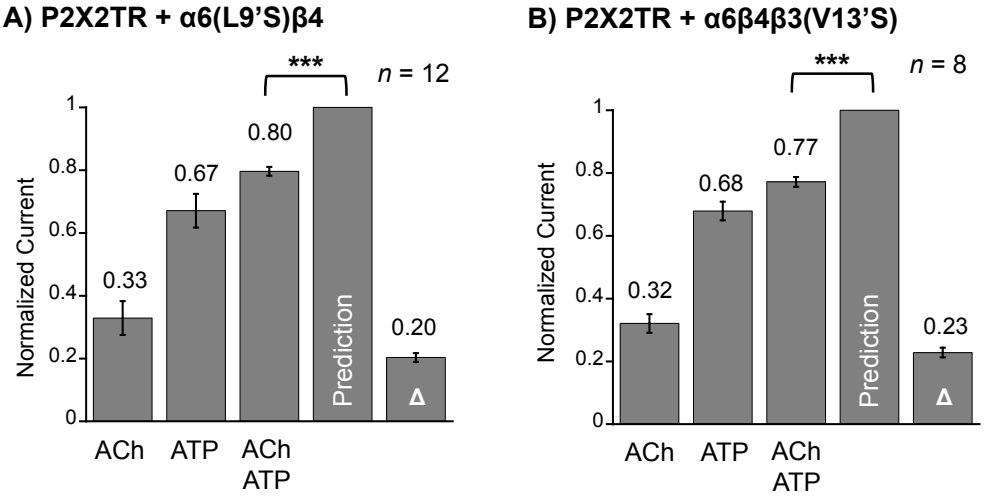

Figure 4.9. Functional interaction between α6β4* nAChRs and P2X2TR receptor. Cross inhibition was observed between the P2X2TR receptor and α6(L9'S)β4 nAChR **(A)**, as well as between the P2X2TR receptor and α6(L9'S)β4 nAChR α6β4β3(V13'S) **(B)**. Currents were normalized to the prediction from the individual cell, and then averaged. Δ is the difference between the prediction and the observed $I_{ACh+ATP}$. ***, $p < 0.0001$.

The P2X3(K65A)TR receptors had comparable ATP EC_{50} to the full-length P2X3(K65A) receptors. Parallel to what was seen with the full-length receptors, co-expression with α6(L9'S)β4 shifted the ATP dose-response curve to the right, increasing the ATP EC_{50} (Figure 4.10). However, we did not observe any cross inhibition between P2X3TR and α6(L9'S)β4 at a saturating ATP concentration (320 μM) (Figure 4.10).

The overall results suggest two distinct modes of cross inhibition between P2X3(K65A) receptors and α6(L9'S)β4: (*i*) a decrease in the maximal I_{ATP} response, which requires the *C*-terminal domain of P2X3 and (*ii*) a decrease in ATP sensitivity, which is independent of the *C*-terminal domain.

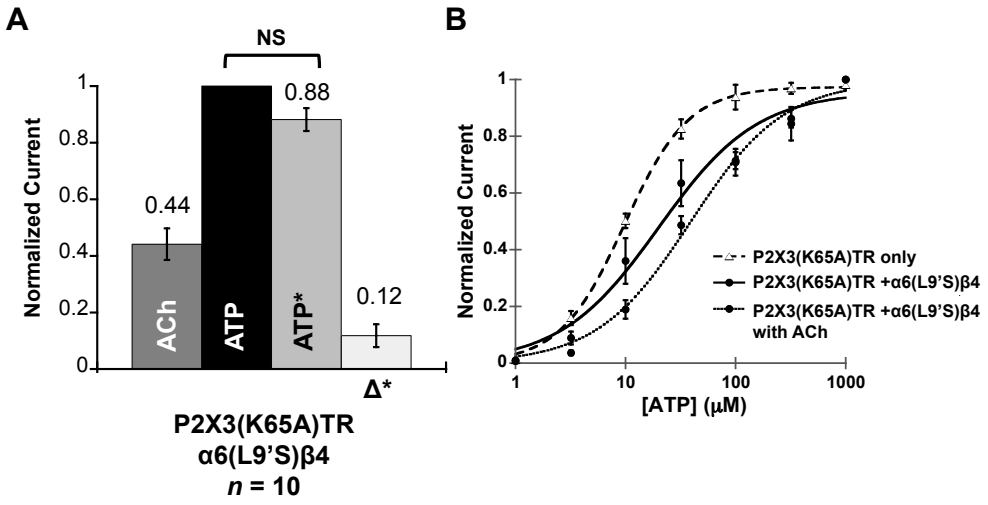

Figure 4.10. Functional interaction between P2X3(K65A)TR and α6(L9'S)β4. **(A)** Cross inhibition was not observed between P2X3(K65A)TR and α6(L9'S)β4. Δ* is the difference between I_{ATP} and I_{ATP*}. Currents were normalized to I_{ATP} from the individual cell, and then averaged. NS, not significant. **(B)** ATP dose-response curves for wild-type P2X3(K65A)TR oocytes (EC_{50} 9.73 ± 0.29 μM, Hill constant 1.5 ± 0.06, n = 6), P2X3(K65A)TR–α6(L9'S)β4 oocytes in an absence of ACh (20.1 ± 5.3 μM, Hill constant 0.97 ± 0.20, n = 7), and P2X3(K65A)TR–α6(L9'S)β4 oocytes in the presence of 100 μM ACh (39.0 ± 6.5 μM, Hill constant 1.0 ± 0.13, n = 8)

4.2.6 Investigation of current occlusion using mecamylamine

The cross-inhibitory behavior observed in oocytes expressing both α6β4* nAChR and P2X receptor during simultaneous application could be a result of an ion channel occlusion that occurred to a subpopulation of the receptors. We sought to use a selective open channel blocker of the nAChR to distinguish between the α6β4* and the P2X ion channel activities during the cross inhibition. (A selective open channel blocker of a P2X receptor has never been reported to our knowledge.) An open channel blocker is considered an uncompetitive antagonist, which only binds to its respective receptor within the open ion pore

following the receptor activation. The conformational change generated by agonist binding that leads to the ion channel opening is *not* affected by the presence of an open channel blocker. Unlike other classes of antagonists, an open channel blocker theoretically should not interfere with the mechanism of cross inhibition. When an α6β4* open channel blocker is applied together with ACh and ATP to an oocyte expressing α6β4* and P2X receptor, one should expect to see the current conducted through the P2X channel pore only. This observed current may or may not be identical to the current evoked by ATP alone on the same cell because of the cross-inhibitory effect when ACh is present. We therefore utilized this strategy to identify the occluded channel pore — either the α6β4* or the P2X.

We decided to experiment with mecamylamine (Mec), a known open channel blocker for several nAChR subtypes, based on the information from the heterologously expressed chimeric nAChRs containing the pore domain of the α6-subunit (*30*, *46*). We found that, in oocytes expressing α6(L9'S)β4 or α6β4β3(V13'S), Mec inhibited ACh-evoked current in a reversible manner, although pre-incubation with the antagonist was required as previously reported with other nAChR subtypes (*30*, *47*). Dose-response experiments were performed, and Mec IC_{50} was determined to be 9.1 ± 0.6 μM for α6(L9'S)β4 and 0.93 ± 0.13 μM for α6β4β3(V13'S). In both cell types, Mec blockade was voltage dependent, showing minimal block at positive potentials (data not shown), which suggests that Mec blocked the α6β4* receptors within the ion pore. In oocytes expressing α6(L9'S)β4 alone or oocytes co-expressing α6(L9'S)β4 and

P2X2, 500 μM Mec blocked > 95% of the ACh-evoked current and did not affect the ATP-evoked current. In oocytes expressing α6β4β3(V13'S) alone or co-expressing α6β4β3(V13'S) and P2X2, similarly, > 95% ACh-evoked current was blocked by 50 μM of Mec, while Mec did not affect the ATP-evoked current. Thus, mecamylamine served as a suitable open channel blocker for the purpose of this experiment. Furthermore, because Mec inhibited the ACh-evoked current nearly completely while leaving the ATP-evoked current unaffected, the data also indicate that the interaction between α6β4* and P2X2 receptors did not involve a cross activation of P2X2 receptor by ACh or a cross activation of α6β4* by ATP.

Co-application of ACh, ATP, and Mec produced an inward current ($I_{ACh+ATP+Mec}$) that was smaller than the current induced by ACh and ATP ($I_{ACh+ATP}$) on the same cells in both α6(L9'S)β4–P2X2 and α6β4β3(V13'S)−P2X2 oocytes. In the case of P2X2–α6(L9'S)β4 oocytes, $I_{ACh+ATP+Mec}$ was significantly smaller than I_{ATP}, and the blocked current, $I_{ACh+ATP+Mec} - I_{ACh+ATP}$ (I_{mec}), was essentially equal to I_{ACh} (Figure 4.11A). Because co-application ACh, ATP, and Mec only produced just the current flowing through P2X2 channels during the cross inhibition, the data suggest that a subpopulation of the P2X2 receptor was inhibited while the α6(L9'S)β4 receptor was fully open during the agonist co-application. In the case of P2X2–α6β4β3(V13'S) oocytes, $I_{ACh+ATP+Mec}$ was essentially the same as I_{ATP} (Figure 4.11B), suggesting that the P2X2 receptor was fully open, in contrast to what was seen with the P2X2–α6(L9'S)β4 oocytes. Moreover, I_{ACh} was essentially

equal to the sum of Δ and I_{Mec} (Figure 4.11), implying that the α6β4β3(V13'S) receptor was inhibited during the cross interaction.

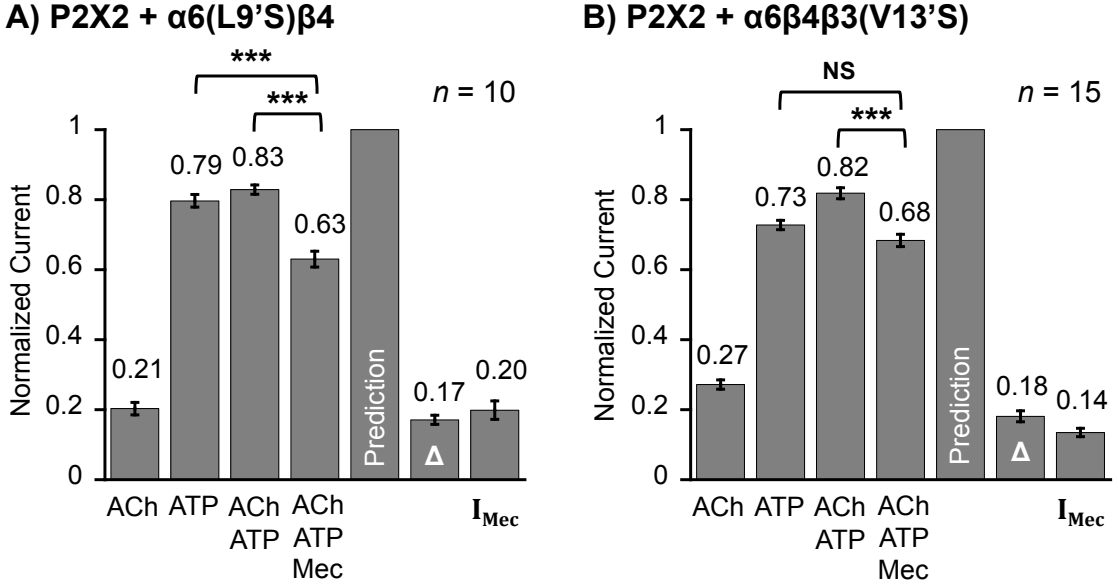

Figure 4.11. Inhibition of $I_{ACh+ATP}$ by mecamylamine in P2X2–α6β4* oocytes. Mean currents elicited by ACh, ATP, ACh+ATP, and ACh+ATP+Mec, respectively, are shown for oocytes expressed with P2X2–α6(L9'S)β4 **(A)** or P2X2–α6β4β3(V13'S) **(B).** Currents were normalized to the prediction from the individual cell, and then averaged. Δ is the difference between the prediction and the observed $I_{ACh+ATP}$. I_{Mec} is the difference between $I_{ACh+ATP+Mec}$ and $I_{ACh+ATP}$. **(A)** $I_{ACh+ATP+Mec} > I_{ATP}$ and $I_{ACh} \approx I_{Mec}$. **(B)** $I_{ACh+ATP+Mec} \approx I_{ATP}$ and $I_{ACh} \approx \Delta + I_{Mec}$. ***, $p <$ 0.0001. NS, not significant

In the case of the P2X2/3 receptor, we found that Mec did not affect $I_{\alpha\beta_{meATP}}$ in the oocytes expressing P2X2/3, regardless of the α6β4* presence. In the oocytes expressing P2X2/3 and α6(L9'S)β4, the current elicited by ACh+αβmeATP+Mec ($I_{ACh+\alpha\beta_{meATP+Mec}}$) was essentially identical to $I_{\alpha\beta_{meATP}}$ (Figure 4.12). The result suggests that the ion pore of the P2X2/3 receptor was fully

open, and thus, the observed inhibition occurred at the α6(L9'S)β4 channel. The oocytes expressing P2X2/3 and α6β4β3(V13'S) showed a slight difference in the amplitudes of $I_{ACh+\alpha\beta meATP+Mec}$ and $I_{\alpha\beta meATP}$, which was not statistically meaningful. Similar to the case of P2X2/3–α6(L9'S)β4, current occlusion did not occur at the P2X2/3 channel pore. Comparison between I_{ACh} and I_{Mec} is not meaningful here due to the mixed I_{ACh} signals arising from the α6β4*–P2X2, α6β4*–P2X3, and α6β4*–P2X2/3 interactions.

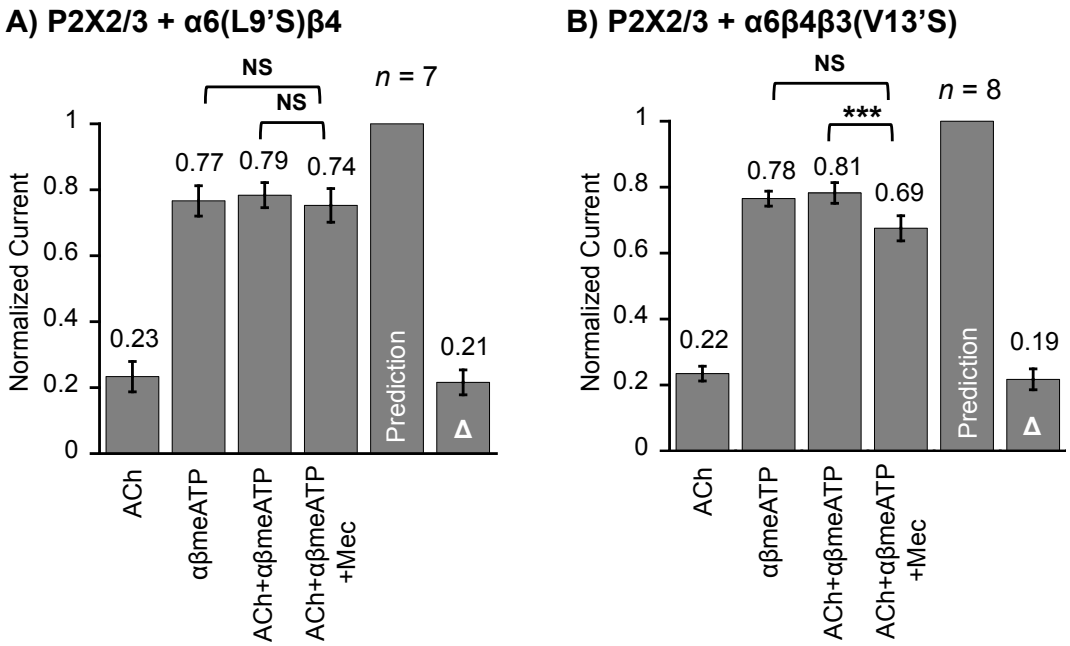

Figure 4.12. Inhibition of $I_{ACh+\alpha\beta meATP}$ by mecamylamine in P2X2/3–α6β4* oocytes. Currents elicited by ACh, αβmeATP, ACh+αβmeATP, and ACh+αβmeATP+Mec are shown for oocytes expressed with P2X2/3–α6(L9'S)β4 **(A)** and P2X2/3–α6β4β3(V13'S) **(B).** Currents were normalized to the prediction from the individual cell, and then averaged. Δ is the difference between the prediction and the observed $I_{ACh+\alpha\beta meATP}$. ***, $p < 0.0001$. NS, not significant

Even though we demonstrated from the mecamylamine block that the α6(L9′S)β4 receptor was fully open during the cross interaction with P2X2 receptor, we could not detect any effect of mecamylamine on the oocytes co-expressing α6(L9′S)β4 and the fast-desensitizing P2X2(T18A) (data not shown). The opening of the P2X2(T18A) receptor was likely too brief for the cross interaction to be probed by this type of experiment. We suspected that the insufficient opening lifetime would be the case for the P2X3 receptor as well, even in the presence of the K65A mutation. Therefore, only the data from the P2X2–α6β4* and P2X2/3–α6β4* oocytes are reported.

4.2.7 Role of P2X2 desensitized state in the cross interaction with α6(L9′S)β4 nAChR

The different ATP current traces between oocytes expressing P2X2 only and P2X2+α6(L9′S)β4 led us to speculate that P2X2 desensitization was involved in the cross inhibition (Figure 4.2). We, therefore, performed more detailed studies on oocytes co-expressing P2X2 and α6(L9′S)β4 for a better understanding of the role of P2X2 desensitization.

On oocytes expressing P2X2 alone and oocytes expressing P2X2–α6(L9′S)β4, we compared the observed current amplitudes as we applied consecutive doses of 1 mM ATP with a 3-minute interval between doses. The P2X2 oocytes showed minimal sign of desensitization upon repeating applications of 1 mM ATP. However, we observed a meaningful reduction in

current size with the P2X2–α6(L9′S)β4 oocytes even though they had never been pre-exposed to an agonist, i.e., the oocytes were *naïve* (Figure 4.13). Similar result was observed when the P2X2–α6(L9′S)β4 oocytes were pre-exposed to ACh. The lost ATP current signal was recoverable over time (data not shown), suggestive of a slow recovery from the desensitized state. However, after a pre-exposure to a mixture of ACh and ATP, repeating ATP doses did not display any reduction in current magnitude (Figure 4.13). This could suggest that the P2X2 receptors had already been desensitized since the application of ACh+ATP. We observed no sign of abnormal ACh desensitization upon repeating application of ACh in oocytes expressing α6(L9′S)β4 alone or co-expressing P2X2 and α6(L9′S)β4 (data not shown). The overall results imply that the P2X2 receptor exhibited a very slow recovery from the desensitized state in the presence of α6(L9′S)β4, regardless of the α6(L9′S)β4 activation by ACh. Thus, the interaction between P2X2 and α6(L9′S)β4 receptor exists prior to the ACh application.

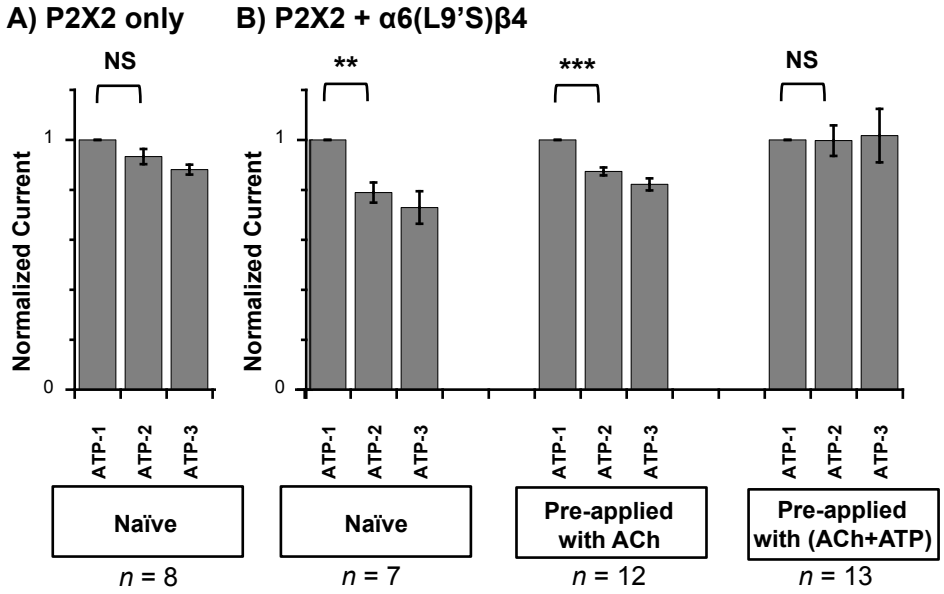

Figure 4.13. The effect of α6(L9'S)β4 on P2X2 desensitized state lifetime. Oocytes were exposed to 3 consecutive doses of 1 mM ATP with a 3-minute interval of wash between doses. Currents were normalized to the current amplitude of the first ATP application from the individual cell, and then averaged. **(A)** Current from P2X2 oocytes display a normal recovery from desensitization. **(B)** Current from naïve P2X2–α6(L9'S)β4 oocytes were only partially recovered after the first ATP dose (*left)*. Incomplete recovery of currents was also observed from oocytes that were exposed to ACh prior to the consecutive doses of ATP (*middle*). However, when oocytes were pre-exposed to an ACh+ATP mixture, no reduction in current amplitudes was observed upon repeating ATP application (*right*). **, $p < 0.005$; ***, $p < 0.0001$. NS, not significant

Next, we asked whether or not cross inhibition would occur between α6(L9'S)β4 and desensitized P2X2 receptors. We tested the P2X2–α6(L9'S)β4 oocytes with a series of agonists in the following order: ACh, four repeating doses of 1mM ATP, ACh+ATP. As expected, ATP-evoked current was smaller upon repeating ATP doses (Figure 4.14, ATP-1 to ATP-4), indicative of a subpopulation of P2X2 being desensitized. Ultimately, no cross inhibition was seen — $I_{ACh+ATP}$ was within error of the predicted sum of the ACh current and the

last ATP current (Figure 4.14). Therefore, the desensitized P2X2 did not functionally interact with the α6(L9′S)β4 nAChR, and the P2X2 desensitization alone could fully explain the cross-inhibitory behavior that we observed.

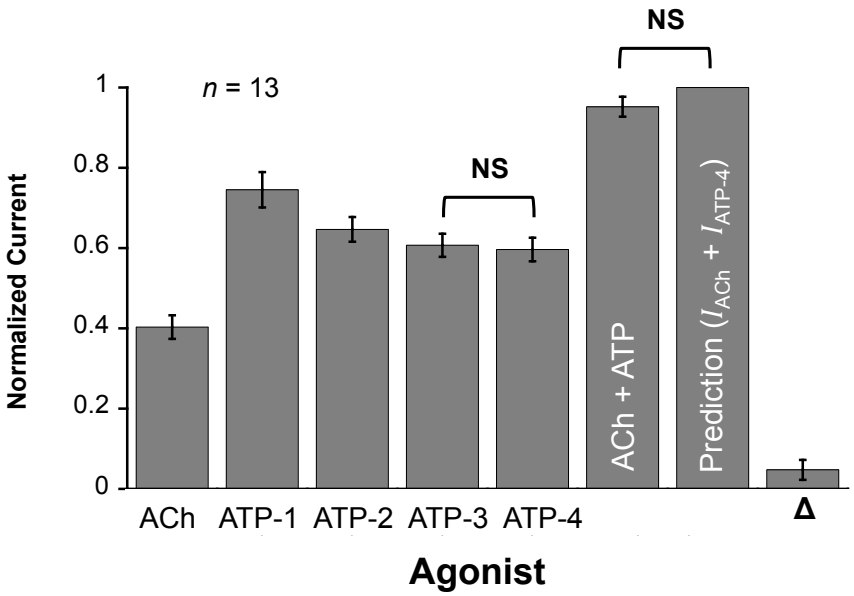

Figure 4.14. Cross inhibition was not observed between desensitized P2X2 and α6(L9′S)β4. P2X2–α6(L9′S)β4 oocytes were exposed to 100 μM ACh, 4 × 1 mM ATP, and (100 μM ACh + 1mM ATP), respectively, with a 3-minute interval of wash between agonist applications. Currents were normalized to the prediction from the individual cell (ACh + ATP-4), and then averaged. Δ is the difference between the prediction and the observed I_{ATP}. NS, not significant

In order to confirm the role of P2X2 desensitization in the functional cross interaction with α6(L9′S)β4, we switched the order of agonist applications in six different combinations. We observed cross inhibition in three out of six cases. In all of the cases that exhibited cross inhibition, ATP was applied before the mixture of ACh and ATP (Figure 4.15). The result is consistent with the notion that a subpopulation of P2X2 was desensitized after an exposure to ATP, causing the apparent cross inhibition.

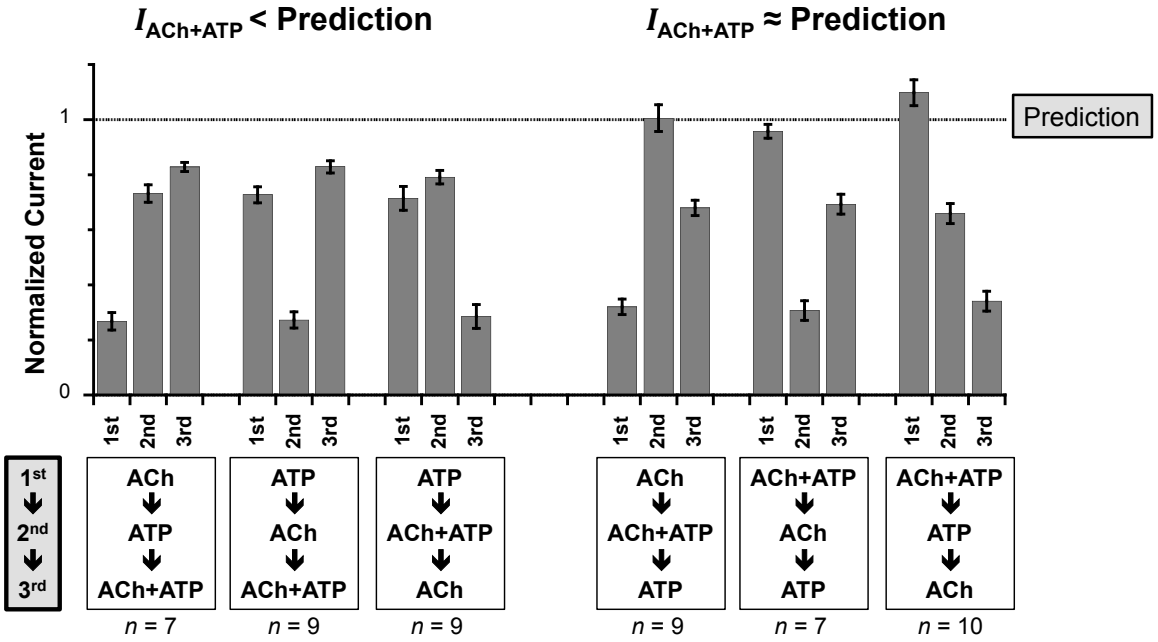

Figure 4.15. Varying sequences of agonist applications produced both non-additive currents (*left*) and additive currents (*right*) from P2X2–α6(L9′S)β4 oocytes. Sequences of agonist applications are indicated at the bottom. There is a 3-minute interval of wash between two agonist applications. Currents were normalized to the prediction from the individual cell, and then averaged.

If the prolonged desensitized state of P2X2 after an exposure to ATP were the sole mechanism underlying the cross inhibition, one would expect the sum of I_{ACh} and I_{ATP} to be smaller than the observed $I_{ACh+ATP}$ in all the cases that ATP was applied *after* the mixture of ACh and ATP. However, we observed current additivity in all these cases — the mean $I_{ACh+ATP}$ was, in fact, comparable to the sum of I_{ACh} and I_{ATP} (Figure 4.15). Considering that the α6(L9′S)β4-*free* P2X2 receptor population contributed to all of the observed I_{ATP} after being exposed to ACh+ATP (Figure 4.13), the additivity means a fraction of current from the α6(L9′S)β4–P2X2 receptor complex was also missing during the ACh+ATP application. Thus, the inhibition occurred instantaneously during the co-

application of ACh+ATP. Consistent with this new insight, we found that repeating application of ACh+ATP mixture to *naïve* oocytes did not produce traces with a substantial decrease in current amplitudes, lacking a sign of receptor desensitization. This could mean either (*i*) there is another different cross-inhibitory mechanism happening while ACh and ATP were co-applied or (*ii*) P2X2 desensitized instantaneously, as soon as the α6(L9'S)β4 was activated by ACh. To distinguish which ion channels were occluded during the co-application of ACh and ATP would be difficult due to the prolonged desensitized state of P2X2 receptor.

In summary, the results in this section suggest that (*i*) cross inhibition between P2X2 and α6(L9'S)β4 receptors was observed as a result of the prolonged desensitization of P2X2 receptor, (*ii*) the desensitized P2X2 receptor can no longer interact with α6(L9'S)β4 receptor, and (*iii*) cross inhibition also occurred while ACh and ATP were co-applied by an unknown mechanism. These observations are unique to the P2X2–α6(L9'S)β4 interacting pair — there is no obvious sign of prolonged desensitized state from the oocytes co-expressing the P2X2–α6β4β3(V13'S), P2X2/3–α6(L9'S)β4, or P2X2/3–α6β4β3(V13'S) combinations.

4.3 Discussion

Several neuronal cell types co-express nicotinic acetylcholine receptors and P2X receptors. Previous experiments from several laboratories show that the functions of these two ligand-gated ion channel subtypes are modulated by each other when they are activated simultaneously by their own neurotransmitters (*4–10*, *12–17*, *48*). Because these functional interactions have been established in several types of neurons as well as heterologous expression systems, the interaction is not a neuron-specific response and it does not require neuron-specific proteins or other molecules. We extended these studies to interactions between α6β4* nAChRs and P2X2, P2X3, or P2X2/3 receptors in *Xenopus* oocytes. All of these receptors are known to co-express in DRG neurons, where the expression of the α6-nAChR subunit is proposed to have a pain-protection effect through the presumed functional connection with the P2X receptors.

We studied functional interactions in six different combinations of P2X (P2X2, P2X3, and P2X2/3) and α6β4* (α6(L9'S)β4 and α6β4β3(V13'S)) receptors in *Xenopus* oocytes. We began our study by applying a series of agonists at their saturating doses. With five of the six combinations, we found functional interactions in the form of cross inhibition between these two classes of ligand-gated receptors. That is, when ACh and ATP were co-applied, the agonist-induced currents were less than the sum of individual currents. This pattern was observed with either type of α6β4* nAChR expressed with P2X2 (Figure 4.1) or with P2X2/3 receptors (Figure 4.8). When α6β4* nAChRs were expressed alone, ATP did not gate or modulate these receptors, and conversely, ACh did not gate

or modulate P2X receptors when they were expressed alone. Cross inhibition was also observed between α6(L9′S)β4 and P2X3(K65A) receptors (Figure 4.4). In this case, the distinctive waveform of the P2X3(K65A) response allows the direct observation that a fraction of current was inhibited when ATP was applied in the presence of ACh in relation to when it was applied alone.

While the expression of P2X receptors is robust in *Xenopus* oocytes, expression of α6-containing nAChRs in heterologous systems is known to be problematic (*28*, *30*, *49*). Even though we successfully expressed both the α6β4 and α6β4β3 subtypes by using a gain-of-function mutation in the pore region, the current produced by α6β4* nAChR was only a few μA, which was not nearly as large as the P2X current. The presumably limited density of the α6β4* nAChRs on the membrane was a concern for the receptor-receptor interaction to occur. Plasma membrane channel density was previously shown to be a determinant of interactions between α3β4 nAChR and P2X2 receptors in *Xenopus* oocytes (*41*). With the difficulty in α6β4* expression, oocytes co-expressed with α6β4* and P2X produced I_{ACh} that was only 20-50% of I_{ATP} in all of our experiments. We intentionally expressed an excess of the P2X receptors with respect to the α6β4* to gain sufficient receptor density for the receptor interaction. However, the substantial difference in the magnitude of I_{ACh} and I_{ATP} complicated the analysis of our cross-inhibition data. In most cases where cross inhibition was observed, the inhibited current was ~ 75–80% of the expected current; the difference between $I_{ACh+ATP}$ and the predicted value (Δ) never exceed ~ 25% of the prediction.

It is worth mentioning that the extent of current reduction (Δ or Δ*) did not accurately represent the degree of the cross inhibition because these values were also dependent on the density of the two receptors being expressed. Because the inhibited current, Δ or Δ*, was presumably constrained by the available number of the α6β4* population on the cell membrane, comparing Δ (or Δ*) to I_{ACh} provides an additional determination for the significance of the receptor interaction. Figure 4.16 shows that, in all the cases that displayed significant current reduction, the magnitude of the reduced current (Δ or Δ*) is greater than 50% of I_{ACh}. The inhibition was particularly substantial in the case of P2X2–α6(L9′S)β4 and P2X2/3–α6(L9′S)β4 pairs, in which the reduced current was 83% and 93% of I_{ACh}, respectively.

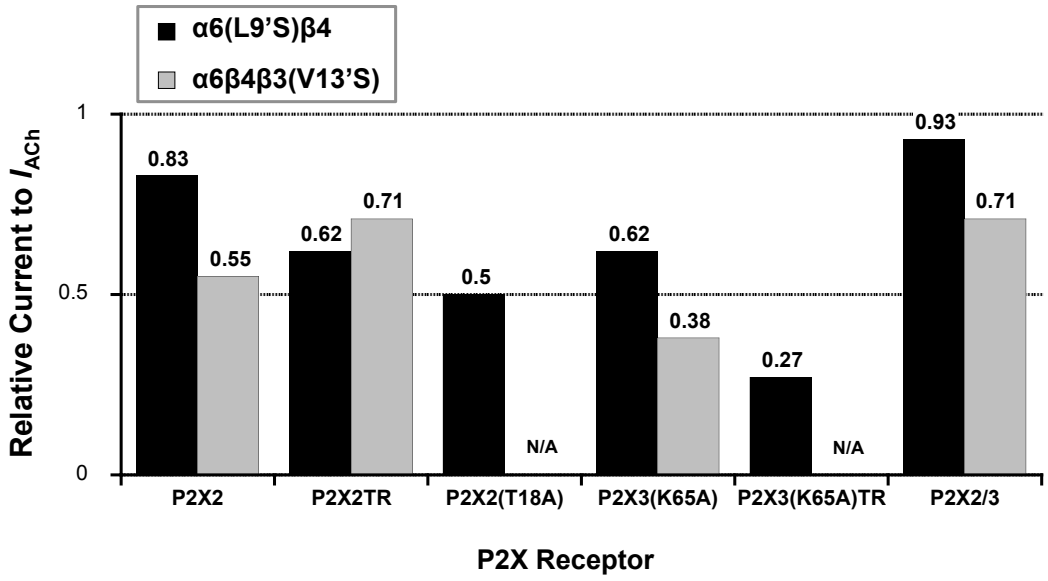

Figure 4.16. Comparison of Δ or Δ* with respect to I_{ACh} across all combinations of receptors. Δ or Δ* was normalized to I_{ACh}. The effect > 0.5 is deemed physiologically significant. N/A, data not available

The crosstalk between the P2X and the Cys-loop families of ligand-gated ion channels has been widely postulated to involve a physical occlusion of the ion channel pores during simultaneous agonist application (*4–7*, *9*, *11*, *13–17*, *50–52*). The proposed models commonly entail a general mechanism of state-dependent "conformational spread" from one receptor to the other. The concept of conformational spread, originally proposed for bacterial chemotaxis receptors, describes the propagation of allosteric states in large multi-protein complexes (*53*). Through this conformational spread, the motion triggered by the gating of one channel type is communicated to the other channels and induces their closure (*4*, *5*, *7*, *8*, *12*). A prerequisite for such a mechanism is the close proximity of receptors.

Physical interactions have been established between P2X2 or P2X3 receptors and α6β4 receptor in Neuro2a cells and cultured mouse cortical neurons by Förster resonance energy transfer (FRET), and moreover, the incorporation of β3 did not alter the binding fraction or the FRET efficiency.[2] Because FRET typically reveals interactions between fluorophores that are less than ~ 80 Å apart, these data imply that the P2X and the α6β4* receptors exist as a macromolecular complex. However, the number of P2X and α6β4* receptors in the protein complex is currently unknown. Previous works also demonstrated physical interactions between α4β2 and P2X2 receptors by FRET (*8*). Additionally, the 5-HT_3 and the $GABA_C$ receptors have been shown to co-precipitate and co-localize with P2X2 receptors by others (*6*, *7*). Evidences for physical interactions eliminate the

[2] Mona Alqazzaz, Christopher R. Richard, and Henry A. Lester, unpublished data

possibility of a major role for second messengers generated by endogenous and electrophysiologically silent metabotropic P2Y in the cross inhibition.

With the evidence for a physical interaction, we assume that *at least* three different populations of receptors existed on the plasma membrane of the oocytes in our experiments: free P2X receptor, free α6β4* receptor, and the α6β4*−P2X complex. We also assume that the free α6β4* population was minimal since the P2X receptors were expressed in excess. It is therefore intriguing that the oocytes expressing P2X2/3 and α6(L9'S)β4, which contained a mixture of P2X2−α6(L9'S)β4, P2X3−α6(L9'S)β4, and P2X2/3−α6(L9'S)β4 populations, exhibited > 90% current inhibition with respect to the ACh-evoked current (Figure 4.16). One possible explanation is that the heteromeric P2X2/3 has a higher affinity for the α6(L9'S)β4 than the homomeric receptors. Alternatively, the presence of multiple P2X receptors in a receptor complex provides another possible explanation; the density of P2X2/3 on the membrane could be so high that every α6(L9'S)β4 receptor had at least one P2X2/3 receptor present in the same complex. However, without a clear view of the cross-inhibitory mechanism of all the receptor combinations on the cells, the underlying cause of the extraordinarily potent cross inhibition between P2X2/3 and α6(L9'S)β4 is still a mystery.

In order to investigate the pore occlusion during the receptor co-activation by ACh and ATP, we used mecamylamine (Mec) for discriminating between the current flowing through α6β4* channel (I_α6) from the current flowing through

the P2X channel (I_P2X). We do *not* make the assumption that I_α6 is necessarily identical to I_{ACh} or I_P2X to I_{ATP} because the two families of proteins are evidently interacting. In oocytes co-expressing P2X2–α6β4*, we found that Mec inhibited > 95% of I_{ACh} without affecting I_{ATP}. This indeed verifies that all ACh-elicited current passed through the α6β4* channel pores exclusively, and the ATP-elicited current only passed through P2X channel pores. The result also suggests that the previous proposal of *channel overlap*, in which ATP activates a subpopulation of the nicotinic receptor channels, is not the case here (*10*). The voltage-dependent nature of the block confirms that Mec binds deep into the membrane and simply occludes channel pore. Hence, the pore blocker is not likely to interfere with the agonist binding, the opening of the pore, or the protein-protein interaction.

Our mecamylamine experiments show that, in three out of four cases, the P2X channel pores were not affected by the cross inhibition. In the case of P2X2–α6β4β3(V13'S), Δ and I_{Mec} also added up to I_{ACh}, providing an internal reference for the occlusion of the α6β4β3(V13'S) channel as both receptors were co-activated. The result from the case of P2X2–α6(L9'S)β4 differs from all other cases that include the β3(V13'S) subunit in the nAChR or the P2X3 subunit, suggesting that the mechanism of the cross inhibition is dependent on both nAChR and P2X receptor subunit compositions. In a previous study, co-activation of P2X2 and various subtypes of $GABA_A$ receptor leads to a functional cross inhibition that was dependent on the $GABA_A$ subunit composition (*5*). By distinguishing the ion conduction through the α6β4* from the P2X channel pores,

the data enable us to identify which receptor was inhibited in all the four combinations that we could test. The experiments, however, only captured a "snapshot" of the cross-inhibition event during the agonist co-application without providing any information regarding the states of the inhibiting or the inhibited receptors at the time of the snapshot.

The results from our investigation of P2X2–α6(L9'S)β4 desensitization clearly supported a role for P2X2 desensitization state in the receptor crosstalk. A subpopulation of the P2X2 receptors desensitized more rapidly and recovered very slowly from the desensitized state — a behavior that was only observed when P2X2 was co-expressed with the α6(L9'S)β4 receptor. The observation was independent of the α6(L9'S)β4 activation by ACh. When we applied a series of agonists in the order of ACh → ATP → ACh+ATP, incomplete recovery of this subpopulation of the receptor after an application of ATP led the apparent current reduction in the subsequent ACh+ATP application, i.e., the cross-inhibition phenomenon. Once desensitized, the P2X2 receptor could no longer functionally interact with the α6(L9'S)β4 receptor (Figure 4.14). We also found that the P2X2 receptors that were pre-exposed to ACh+ATP exhibited a normal recovery from desensitization during the subsequent applications of ATP, implying that all of the α6(L9'S)β4-bound P2X2 receptors had been desensitized during the ACh+ATP exposure (Figure 4.13). Furthermore, when ACh+ATP was applied before ATP, we did not observe any cross inhibition — $I_{ACh+ATP}$ was equal to the sum of the subsequent I_{ACh} and I_{ATP} in all three cases (Figure 4.15). The current additivity shown in Figure 4.15 *cannot* be explained by the absence of

receptor crosstalk. Instead, the apparent additivity of the system suggests that current inhibition had to occur concurrently as ACh+ATP was first applied. Taken together, these data revealed another hidden mode of cross inhibition that was previously obscured by the P2X2 desensitization. This mode of interaction is only detectable during the *first* co-application of ACh and ATP, before the interacting P2X2 population is desensitized. A series of drugs needed to be applied in order to evaluate the results in this type of experiment, and as such the prolonged desensitized state of the interacting P2X2 receptor population limits our ability to probe for the mechanism of the pore occlusion during co-activation of the P2X2–α6(L9′S)β4 complex. Our mecamylamine experiments on the P2X2–α6(L9′S)β4 oocytes were only able to probe the apparent cross inhibition when the interacting P2X2 receptor was already desensitized. The unique characteristic of the P2X2 desensitization was presumably modified simply by being associated with the α6(L9′S)β4 receptor without receptor activation.

Previous works have reported contradicting observations on the cross inhibition during desensitization. Our studies show that, for both P2X2–α6(L9′S)β4 and P2X3(K65A)–α6(L9′S)β4, the functional interaction was lost when the involved P2X receptor was desensitized, which is consistent with a previous study involving cross inhibition between ACh receptor and ATP receptor in rat sympathetic neurons (*10*). In contrast, another work reported that the desensitized P2X2(T18A) receptor could still inhibit α3β4 nAChR (*41*). This result is supported by a more recent study, finding that the α3β4 nAChR can interact with the P2X2, P2X3, and P2X4 receptors during their desensitized state,

although the extent of cross inhibition was not equivalent to that occurring when fully active, non-desensitized receptors were studied (*12*). Nevertheless, the cross-inhibitory mechanism is likely specific to the P2X and nAChR subtypes involved in the interaction.

The case of P2X2–α6(L9′S)β4 indicates that the activation of both interacting receptors is not necessarily required for the functional interaction to take place. Agonist EC_{50} is another convenient probe for receptor function, and a shift in EC_{50} values is suggestive of a gating modulation induced by the crosstalk. In most cases where we could study dose-response relations, we found only minor (< 2-fold) changes in the EC_{50} values for each agonist when we co-expressed these receptors (Table 4.1). An exception is the case with P2X3(K65A)–α6(L9′S)β4, in which the ATP EC_{50} of the P2X3(K65A) receptor was ~ 3-fold higher when the α6(L9′S)β4 receptor was present. These shifts did not depend on the presence of ACh (Figure 4.5). The response also showed a decreased apparent cooperativity, revealed by a reduced Hill coefficient (Figure 4.5). The result implies that cross inhibition also occurred at submaximal concentrations of ATP. The co-expression, however, did not change the EC_{50} for ACh. The presence of α6(L9′S)β4 did not affect the ATP EC_{50} for the fast-desensitizing P2X2(T18A) receptor, while the cross inhibition was still observed between this pair of receptors at the maximal ATP dose. The shift in dose-response relation in the presence of α6(L9′S)β4 is, therefore, a specific P2X3(K65A) character and is not a result of an error in measuring fast-desensitizing current.

The intracellular *C*-terminal domains of P2X2 and P2X3 have been shown to be necessary for the expression of their cross inhibition to some Cys-loop receptors, including α3β4 nAChR, $GABA_A$, $GABA_C$, and 5-HT_3 receptors (*4–7*, *13*). In the case of P2X2−α6β4*, removal of the P2X2 *C*-terminal domain did not affect the cross inhibition at the maximal doses of agonist, and the slow recovery from desensitization was still observed for the P2X2TR receptor co-expressed with α6(L9′S)β4 (data not shown). In the case of P2X3(K65A)–α6(L9′S)β4, we found that the *C*-terminus of P2X3(K65A) is responsible for the current occlusion at the maximal ATP dose but is not required for the rightward shift in the ATP dose-response relation.

The overall results indicate that the P2X−α6β4* interaction is inhibitory. Two distinct mechanisms are suggested to be involved in the functional coupling between these two families of ligand-gated ion channels, highlighted by the results from α6(L9′S)β4 interactions with P2X3(K65A), P2X2(T18A), and P2X3(K65A)TR. The first class takes the form of current occlusion: when both receptors are co-activated by ACh and ATP, the agonist-induced currents are less than the sum of individual currents. This type of mechanism is commonly observed between Cys-loop receptors and P2X receptors.

The interaction likely depends on the physical contact between the two receptors, enabling the activation of one receptor by its agonist to induce a conformational change that results in the pore occlusion of the other ion channel across the protein complex through an allosteric effect. This supports the previous proposal of the conformational spread mechanism. The intracellular *C*-

terminal domains of the P2X receptor possibly play a role in this type of interaction for some P2X–Cys-loop receptor pairs. The second class of P2X–α6β4* interaction is pre-organized. This type of mechanism is constitutive and does not require receptor activation. A change in P2X2 desensitization properties in the presence of α6(L9'S)β4 and a shift in P2X3(K65A) EC_{50} are the examples. The physiology of the ion channels is altered, possibly through physical interaction that possibly does not involve the P2X *C*-terminus. In other words, one receptor may act as a constitutive allosteric modulator of the other. This type of cross inhibition had only been reported for the P2X2–α3β4 nAChR pair, in the forms of constitutive current suppression and the shift in the dose-response relations (*13*). Also supporting this view, competition experiments have shown that expression of a minigene encoding the *C*-terminal domain of P2X2 could disrupt functional interaction but *not* physical interaction between the P2X2 and 5-HT_3 receptors, (*6*) although the constitutive functional interaction was not demonstrated in those experiments.

We have provided evidence supporting functional interactions between α6β4* nAChR and P2X2, P2X3, and P2X2/3 receptors. This could be a mechanism by which the α6-nAChR subunit is involved in the pain pathway. The α6β4* receptor may directly participate in pain sensation through this functional interaction with the P2X receptor. Alternatively, the α6β4* receptor may serve as a means for modulating the activity of P2X receptors through constitutive binding or regulating the interaction of P2X with other receptors. For example, binding of P2X3 receptors to α6β4* in the DRG neurons may compete with the

molecular interaction between the $GABA_A$ receptor and the P2X3 receptor, which has been proposed to play a role in nociceptive signal transmission as well (*4*, *11*). Nonetheless, crosstalk between two ligand-gated ion channels provides a fast and efficient way to adapt neurotransmitter signaling to changing functional needs through a mechanism that appears to be a complex process that is still poorly understood.

4.4 Materials and Methods

Molecular Biology

Rat α6 and mouse β3 nAChRs were in the pGEMhe vector, and rat β4 nAChR was in the pAMV vector. All P2X cDNAs were in the pcDNA3 vector. Site-directed mutagenesis was performed using the Stratagene QuikChange protocol. Truncated P2X2 and P2X3(K65A) subunits were made by engineering a TAA stop codon at the 3′ end of the sequence encoding the residue 373 of P2X2 or residue 385 of P2X3(K65A). Circular cDNA was linearized with NheI (for the pGEMhe vector), NotI (for the pAMV vector), or XhoI (for the pcDNA3 vector). After purification (Qiagen), linearized DNA was used as a template for runoff *in vitro* transcription using T7 mMessage mMachine kit (Ambion). The resulting mRNA was purified (RNAeasy Mini Kit, Qiagen) and quantified by UV-visible spectroscopy.

Expression of α6* nAChR in Xenopus oocytes

Stage V–VI *Xenopus laevis* oocytes were employed. Each oocyte was injected with 50 nL of mRNA solution. When α6β4* nAChR and P2X receptors are co-expressed, equal volume of corresponding mRNA solutions were mixed prior to the oocyte injection. To express the α6β4 combination, we used the hypersensitive α6 subunit containing a serine mutation at the leucine9′ on M2 (residue 279). The mRNA ratio used was 2:5 α6(L9′S):β4 by mass, and we injected 25–50 ng of total mRNA per cell. We used the wild-type α6 and β4 in combination with the hypersensitive β3 containing a serine mutation at the valine13′ on M2 (residue 283) to express the α6β4β3 combination. The wild-type α6β4 produced no detectable current signal, with or without co-injection of the P2X subunits. Cells were injected with a mixture of mRNA at the ratio of 2:2:5 α6:β4:β3(V13′S) at a total mRNA concentration of 5–20 ng per cell. The optimal mRNA concentration of P2X2 was 0.05 ng per cell when expressed alone and 0.1–0.3 ng per cell when co-expressed with α6β4* nAChR. To study P2X3, we used the K65A mutation, which enhanced the rate of recovery from desensitization. We injected 5ng of P2X3(K65A) mRNA per cell when expressed alone and 10–20 ng of mRNA when co-expressed with α6β4* nAChR. P2X2/3 was expressed by co-injection of 1:10 ratio of P2X2:P2X3 mRNA at 15–25 ng of total mRNA. 25–50 ng of mRNA per cell was required to express P2X2(T18A) and the truncated P2X subunits.

After mRNA injection, cells were incubated for 24–72 hours at 18 °C in culture media ($ND96^{+}$ with 5% horse serum).

Electrophysiology

Acetylcholine chloride was purchased from Sigma-Aldrich/RBI and stored as 1M stock solutions in Millipore water. ATP and α,β-methylene-ATP (αβmeATP) were purchased from Tocris Bioscience and were stored as 100 mM stock solutions in Millipore water. Mecamylamine hydrochloride (Mec) was purchased from Sigma and stored as 100 mM stock solutions. All stock solutions were stored at −80°C, and drug dilutions were prepared from the stock solution in calcium-free ND96 buffer within 24 hours prior to the electrophysiological recordings. The pH of all buffers and drug solutions was adjusted to 7.4.

Ion channel function in oocytes was assayed by current recording in two-electrode voltage-clamp mode using the OpusXpress 6000A (Axon Instruments). Up to eight oocytes were simultaneously voltage-clamped at −60 mV. All data were sampled at 125 Hz and filtered at 50 Hz.

For P2X2, α6(L9'S)β4, or α6β4β3(V13'S) dose-response experiments, 1 mL of total agonist solution was applied to cells, and 7-8 concentrations of agonist were used. Mixtures of ATP and ACh were prepared beforehand in cases of agonist co-application. Cells were perfused in calcium-free ND96 solution before agonist application for 30 seconds, followed by a 15-second agonist application and a 2-minute wash in calcium-free ND96 buffer. A similar protocol was used to investigate cross interaction between P2X2 and α6β4*, except that the wash was extended to 3 minutes. 100 μM of ACh and 1 mM of ATP were used in all cross interaction experiments. The order of application was ACh, ATP, and ACh

+ ATP, unless otherwise specified. 50 μM and 500 μM of mecamylamine were used to block α6β4β3(V13'S) and α6(L9'S)β4 receptors, respectively. In all experiments involving mecamylamine, oocytes were incubated with 0.25 mL of mecamylamine (or buffer) for ~ 20 seconds prior to an application of a pre-mixed solution of agonist(s) and mecamylamine (or just agonist(s)). The order of application was ACh, ATP, ACh + ATP, and ACh + ATP + Mec.

To ensure enough channel density, we only analyze data from cells that produced between 5–13 μA of ATP-evoked current (I_{ATP}) and > 1.5 μA of ACh-evoked current (I_{ACh}). Cells displaying larger currents were discarded to avoid the ambiguity associated with error of the measurement as well as other complications arising from extremely high density of receptors such as *pore dilation*, a phenomenon known to occur for P2X2 receptors at high receptor density (*54–58*).

For ATP dose-response experiments on the fast-desensitizing P2X receptors, including P2X3, P2X3(K65A), P2X3TR, and P2X2(T18A) receptors, ATP application was 2-second duration at the total volume of 0.5 mL, and the wash was 3.5 minutes. For ATP dose-response experiments in the presence of ACh, ACh was pre-applied for 15 seconds through pump B (0.6 mL), followed by a 2-second application of a mixture of ATP and ACh (0.5 mL), another 30-second of ACh application through pump B (1.5 mL), and a 164-second wash in calcium-free ND96. Cross interaction between these fast-desensitizing P2X receptors and α6β4* nAChRs was probed in an experiment that involved an alternate application of saturating ATP doses without ACh and with ACh, using the same

protocol as the dose-response experiments, except that the wash time used was 205-second duration. The concentration of ACh was 100 μM in all cross interaction experiments, and the concentrations of ATP were 100 μM for cells expressing P2X3(K65A) and α6β4β3(V13'S), 320 μM for P2X3(K65A) and α6(L9'S)β4, 320 μM for P2X3TR and α6(L9'S)β4, and 1 mM for P2X2(T18A) and α6(L9'S)β4. Peak currents from at least three traces were averaged from the same cell for data analysis. Data from cells displaying < 1.5 μA of I_{ACh}, < 5 μA or > 11 μA of I_{ATP}, or $I_{ACh} > I_{ATP}$ were excluded from all cross-interaction analysis.

To investigate cross interaction between P2X2/3 receptor and α6β4* nAChR, P2X2/3 receptor was activated by 100 μM αβmeATP, and α6β4* nAChR by 100 μM ACh. All agonist applications were 10-second duration at a volume of 0.5 mL, followed by an extra 5-second of incubation with the agonist(s) without fluid aspiration. Then the cells were washed for ~ 5 minutes. The order of application was αβmeATP, ACh, and αβmeATP+ACh, unless specified otherwise. A similar protocol was used for experiments with mecamylamine, and in addition, cells were pre-incubated in 0.25 mL of either buffer or mecamylamine solution prior to the application of the test doses, in the same manner as described above for P2X2–α6β4*. 50 μM and 500 μM of mecamylamine were used to block α6β4β3(V13'S) and α6(L9'S)β4 receptors, respectively. Only data from cells displaying $I_{\alpha\beta_{meATP}}$ between 5-13 μA, $I_{ACh} \geq 1.5$ μA, and $I_{\alpha\beta_{meATP}} > I_{ACh}$ were included in the analysis.

Data Analysis

All dose-response data were normalized to the maximal current (I_{max} = 1) of the same cell and then averaged. EC_{50} and Hill coefficient (n_H) were determined by fitting averaged, normalized dose-response relations to the Hill equation. Dose responses of individual oocytes were also examined and used to determine outliers.

For all cross interaction data involving P2X2 or P2X2/3, including data from the mecamylamine experiments, the predicted current from agonist co-application was calculated from the arithmetic sum of I_{ACh} and I_{ATP} (or $I_{\alpha\beta_{meATP}}$) from the same cell. The actual, observed current upon co-application of the agonists was subtracted from the prediction value of the same cell, and this difference was designated as the Δ. All current data and Δ were normalized to the prediction value of the same cell, and then the normalized data were averaged across at least 7 cells from at least 2 batches of oocytes.

For all cross interaction data involving the fast-desensitizing P2X receptors, including P2X3, P2X3(K65A), P2X3TR, and P2X2(T18A) receptors, averaged ATP-evoked peak current during ACh application (I_{ATP}*) was subtracted from averaged ATP-evoked current in the absence of ACh (I_{ATP}) from the same cell to obtain a Δ*. All current data and Δ* were normalized to (I_{ATP}) and averaged across at least 8 cells from at least 2 batches of oocytes.

All data are presented as mean ± s. e. m. (n = number of cells), with statistical significance assessed by paired Student's t test. A p value of < 0.01 was accepted as indicative of a statistically significant difference.

4.5 References

(1) Unwin, N. Refined structure of the nicotinic acetylcholine receptor at 4Å resolution. *J. Mol. Biol.* **2005**, *346*, 967–989.

(2) Millar, N. S.; Gotti, C. Diversity of vertebrate nicotinic acetylcholine receptors. *Neuropharmacology* **2009**, *56*, 237–246.

(3) Kawate, T.; Michel, J. C.; Birdsong, W. T.; Gouaux, E. Crystal structure of the ATP-gated $P2X_4$ ion channel in the closed state. *Nature* **2009**, *460*, 592–598.

(4) Toulmé, E.; Blais, D.; Léger, C.; Landry, M.; Garret, M.; Séguéla, P.; Boué-Grabot, E. An intracellular motif of $P2X_3$ receptors is required for functional cross-talk with $GABA_A$ receptors in nociceptive DRG neurons. *J. Neurochem.* **2007**, *102*, 1357–1368.

(5) Boué-Grabot, E.; Toulmé, E.; Emerit, M. B.; Garret, M. Subunit-specific coupling between gamma-aminobutyric acid type A and P2X2 receptor channels. *J. Biol. Chem.* **2004**, *279*, 52517–52525.

(6) Boué-Grabot, E.; Emerit, M. B.; Toulmé, E.; Séguéla, P.; Garret, M. Cross-talk and co-trafficking between rho1/GABA receptors and ATP-gated channels. *J. Biol. Chem.* **2004**, *279*, 6967–6975.

(7) Boué-Grabot, E.; Barajas-López, C.; Chakfe, Y.; Blais, D.; Bélanger, D.; Emerit, M. B.; Séguéla, P. Intracellular cross talk and physical interaction between two classes of neurotransmitter-gated channels. *J. Neurosci.* **2003**, *23*, 1246–1253.

(8) Khakh, B. S.; Fisher, J. A.; Nashmi, R.; Bowser, D. N.; Lester, H. A. An angstrom scale interaction between plasma membrane ATP-gated P2X2 and alpha4beta2 nicotinic channels measured with fluorescence resonance energy transfer and total internal reflection fluorescence microscopy. *J. Neurosci.* **2005**, *25*, 6911–6920.

(9) Khakh, B.; Zhou, X.; Sydes, J.; Galligan, J.; Lester, H. State-dependent cross-inhibition between transmitter-gated cation channels. *Nature* **2000**, *406*, 405–410.

(10) Nakazawa, K. ATP-activated current and its interaction with acetylcholine-activated current in rat sympathetic neurons. *J. Neurosci.* **1994**, *14*, 740–750.

(11) Sokolova, E.; Nistri, A.; Giniatullin, R. Negative cross talk between anionic GABAA and cationic P2X ionotropic receptors of rat dorsal root ganglion neurons. *J. Neurosci.* **2001**, *21*, 4958–4968.

(12) Decker, D. A.; Galligan, J. J. Cross-inhibition between nicotinic acetylcholine receptors and P2X receptors in myenteric neurons and HEK-293 cells. *Am. J. Physiol. Gastrointest. Liver Physiol.* **2009**, *296*, G1267–76.

(13) Decker, D. A.; Galligan, J. J. Molecular mechanisms of cross-inhibition between nicotinic acetylcholine receptors and P2X receptors in myenteric neurons and HEK-293 cells. *Neurogastroenterol. Motil.* **2010**, *22*, 901–8, e235.

(14) Karanjia, R.; García-Hernández, L. M.; Miranda-Morales, M.; Somani, N.; Espinosa-Luna, R.; Montaño, L. M.; Barajas-López, C. Cross-inhibitory interactions between $GABA_A$ and P2X channels in myenteric neurones. *Eur. J. Neurosci.* **2006**, *23*, 3259–3268.

(15) Barajas-López, C.; Montaño, L. M.; Espinosa-Luna, R. Inhibitory interactions between 5-HT_3 and P2X channels in submucosal neurons. *Am. J. Physiol. Gastrointest. Liver Physiol.* **2002**, *283*, G1238–48.

(16) Barajas-López, C.; Espinosa-Luna, R.; Zhu, Y. Functional interactions between nicotinic and P2X channels in short-term cultures of guinea-pig submucosal neurons. *J. Physiol. (London)* **1998**, *513 (Pt 3)*, 671–683.

(17) Zhou, X.; Galligan, J. J. Non-additive interaction between nicotinic cholinergic and P2X purine receptors in guinea-pig enteric neurons in culture. *J. Physiol. (London)* **1998**, *513 (Pt 3)*, 685–697.

(18) Galligan, J. J.; Bertrand, P. P. ATP mediates fast synaptic potentials in enteric neurons. *J. Neurosci.* **1994**, *14*, 7563–7571.

(19) Silinsky, E. M.; Redman, R. S. Synchronous release of ATP and neurotransmitter within milliseconds of a motor nerve impulse in the frog. *J. Physiol. (London)* **1996**.

(20) Redman, R. S.; Silinsky, E. M. ATP released together with acetylcholine as the mediator of neuromuscular depression at frog motor nerve endings. *J. Physiol. (London)* **1994**, *477 (Pt 1)*, 117–127.

(21) Genzen, J. R.; Van Cleve, W.; McGehee, D. S. Dorsal root ganglion neurons express multiple nicotinic acetylcholine receptor subtypes. *J. Neurophysiol.* **2001**, *86*, 1773–1782.

(22) Dubé, G. R.; Kohlhaas, K. L.; Rueter, L. E.; Surowy, C. S.; Meyer, M. D.; Briggs, C. A. Loss of functional neuronal nicotinic receptors in dorsal root ganglion neurons in a rat model of neuropathic pain. *Neurosci. Lett.* **2005**, *376*, 29–34.

(23) Fucile, S.; Sucapane, A.; Eusebi, F. Ca2+ permeability of nicotinic acetylcholine receptors from rat dorsal root ganglion neurones. *J. Physiol. (London)* **2005**, *565*, 219–228.

(24) Haberberger, R. V.; Bernardini, N.; Kress, M.; Hartmann, P.; Lips, K. S.; Kummer, W. Nicotinic acetylcholine receptor subtypes in nociceptive dorsal root ganglion neurons of the adult rat. *Auton. Neurosci.* **2004**, *113*, 32–42.

(25) Rau, K. K.; Johnson, R. D.; Cooper, B. Y. Nicotinic AChR in subclassified capsaicin-sensitive and -insensitive nociceptors of the rat DRG. *J. Neurophysiol.* **2005**, *93*, 1358–1371.

(26) Hone, A. J.; Meyer, E. L.; McIntyre, M.; McIntosh, J. M. Nicotinic acetylcholine receptors in dorsal root ganglion neurons include the α6β4* subtype. *FASEB J.* **2012**, *26*, 917–926.

(27) Wirkner, K.; Sperlagh, B.; Illes, P. P2X3 receptor involvement in pain states. *Mol. Neurobiol.* **2007**, *36*, 165–183.

(28) Kuryatov, A.; Olale, F.; Cooper, J.; Choi, C.; Lindstrom, J. Human alpha6 AChR subtypes: subunit composition, assembly, and pharmacological responses. *Neuropharmacology* **2000**, *39*, 2570–2590.

(29) Tumkosit, P.; Kuryatov, A.; Luo, J.; Lindstrom, J. Beta3 subunits promote expression and nicotine-induced up-regulation of human nicotinic alpha6* nicotinic acetylcholine receptors expressed in transfected cell lines. *Mol. Pharmacol.* **2006**, *70*, 1358–1368.

(30) Gerzanich, V.; Kuryatov, A.; Anand, R.; Lindstrom, J. "Orphan" alpha6 nicotinic AChR subunit can form a functional heteromeric acetylcholine receptor. *Mol. Pharmacol.* **1997**, *51*, 320–327.

(31) Drenan, R. M.; Nashmi, R.; Imoukhuede, P.; Just, H.; McKinney, S.; Lester, H. A. Subcellular trafficking, pentameric assembly, and subunit stoichiometry of neuronal nicotinic acetylcholine receptors containing fluorescently labeled alpha6 and beta3 subunits. *Mol. Pharmacol.* **2008**, *73*, 27–41.

(32) Broadbent, S.; Groot-Kormelink, P. J.; Krashia, P. A.; Harkness, P. C.; Millar, N. S.; Beato, M.; Sivilotti, L. G. Incorporation of the beta3 subunit has a dominant-negative effect on the function of recombinant central-type neuronal nicotinic receptors. *Mol. Pharmacol.* **2006**, *70*, 1350–1357.

(33) Xiao, C.; Srinivasan, R.; Drenan, R. M.; Mackey, E. D. W.; McIntosh, J. M.; Lester, H. A. Characterizing functional α6β2 nicotinic acetylcholine receptors in vitro: Mutant β2 subunits improve membrane expression, and fluorescent proteins reveal responsive cells. *Biochem. Pharmacol.* **2011**.

(34) Capelli, A. M.; Castelletti, L.; Chen, Y. H.; Van der Keyl, H.; Pucci, L.; Oliosi, B.; Salvagno, C.; Bertani, B.; Gotti, C.; Powell, A.; Mugnaini, M. Stable expression and functional characterization of a human nicotinic acetylcholine receptor with α6β2 properties: discovery of selective antagonists. *Br. J. Pharmacol.* **2011**, *163*, 313–329.

(35) Drenan, R.; Grady, S.; Whiteaker, P.; McClure-Begley, T.; McKinney, S.; Miwa, J.; Bupp, S.; Heintz, N.; McIntosh, J.; Bencherif, M. In Vivo Activation of Midbrain Dopamine Neurons via Sensitized, High-Affinity α6* Nicotinic Acetylcholine Receptors. *Neuron* **2008**, *60*, 123–136.

(36) Drenan, R.; Grady, S.; Steele, A.; McKinney, S.; Patzlaff, N.; McIntosh, J.; Marks, M.; Miwa, J.; Lester, H. Cholinergic Modulation of Locomotion and Striatal Dopamine Release Is Mediated by α6α4* Nicotinic Acetylcholine Receptors. *J. Neurosci.* **2010**, *30*, 9877.

(37) Cohen, B. N.; Mackey, E. D. W.; Grady, S. R.; McKinney, S.; Patzlaff, N. E.; Wageman, C. R.; McIntosh, J. M.; Marks, M. J.; Lester, H. A.; Drenan, R. M. Nicotinic cholinergic mechanisms causing elevated dopamine release and abnormal locomotor behavior. *Neuroscience* **2012**, *200*, 31–41.

(38) Dash, B.; Bhakta, M.; Chang, Y.; Lukas, R. J. Identification of N-terminal Extracellular Domain Determinants in Nicotinic Acetylcholine Receptor (nAChR) α6 Subunits That Influence Effects of Wild-type or Mutant β3 Subunits on Function of α6β2*- or α6β4*-nAChR. *J. Biol. Chem.* **2011**, *286*, 37976–37989.

(39) Fabbretti, E.; Sokolova, E.; Masten, L.; D'Arco, M.; Fabbro, A.; Nistri, A.; Giniatullin, R. Identification of negative residues in the P2X3 ATP receptor ectodomain as structural determinants for desensitization and the Ca^{2+}-sensing modulatory sites. *J. Biol. Chem.* **2004**, *279*, 53109–53115.

(40) Pratt, E. B.; Brink, T. S.; Bergson, P.; Voigt, M. M.; Cook, S. P. Use-dependent inhibition of P2X3 receptors by nanomolar agonist. *J. Neurosci.* **2005**, *25*, 7359–7365.

(41) Khakh, B. S.; Zhou, X.; Sydes, J.; Galligan, J. J.; Lester, H. A. State-dependent cross-inhibition between transmitter-gated cation channels. *Nature* **2000**, *406*, 405–410.

(42) Boue-Grabot, E. A Protein Kinase C Site Highly Conserved in P2X Subunits Controls the Desensitization Kinetics of P2X2 ATP-gated Channels. *J. Biol. Chem.* **2000**, *275*, 10190–10195.

(43) Brake, A. J.; Wagenbach, M. J.; Julius, D. New structural motif for ligand-gated ion channels defined by an ionotropic ATP receptor. *Nature* **1994**, *371*, 519–523.

(44) Khakh, B. S.; Bao, X. R.; Labarca, C.; Lester, H. A. Neuronal P2X transmitter-gated cation channels change their ion selectivity in seconds. *Nat. Neurosci.* **1999**, *2*, 322–330.

(45) Liu, M.; King, B. F.; Dunn, P. M.; Rong, W.; Townsend-Nicholson, A.; Burnstock, G. Coexpression of $P2X_3$ and $P2X_2$ receptor subunits in varying amounts generates heterogeneous populations of P2X receptors that evoke a spectrum of agonist responses comparable to that seen in sensory neurons. *J. Pharmacol. Exp. Ther.* **2001**, *296*, 1043–1050.

(46) Papke, R.; Dwoskin, L.; Crooks, P.; Zheng, G.; Zhang, Z.; McIntosh, J.; Stokes, C. Extending the analysis of nicotinic receptor antagonists with the study of α6 nicotinic receptor subunit chimeras. *Neuropharmacology* **2008**, *54*, 1189–1200.

(47) Papke, R. L.; Sanberg, P. R.; Shytle, R. D. Analysis of mecamylamine stereoisomers on human nicotinic receptor subtypes. *J. Pharmacol. Exp. Ther.* **2001**, *297*, 646–656.

(48) Sokolova, E.; Nistri, A.; Giniatullin, R. Negative cross talk between anionic $GABA_A$ and cationic P2X ionotropic receptors of rat dorsal root ganglion neurons. *J. Neurosci.* **2001**, *21*, 4958–4968.

(49) Kuryatov, A.; Lindstrom, J. Expression of Functional Human α6 β2α3* Acetylcholine Receptors in *Xenopus laevis* Oocytes Achieved through Subunit Chimeras and Concatamers. *Mol. Pharmacol.* **2011**, *79*, 126–140.

(50) Searl, T. J.; Redman, R. S.; Silinsky, E. M. Mutual occlusion of P2X ATP receptors and nicotinic receptors on sympathetic neurons of the guinea-pig. *J. Physiol. (London)* **1998**, *510 (Pt 3)*, 783–791.

(51) Jiang, L.-H. Identification of Amino Acid Residues Contributing to the ATP-binding Site of a Purinergic P2X Receptor. *J. Biol. Chem.* **2000**, *275*, 34190–34196.

(52) Shakirzyanova, A. V.; Bukharaeva, E. A.; Nikolsky, E. E.; Giniatullin, R. A. Negative cross-talk between presynaptic adenosine and acetylcholine receptors. *Eur. J. Neurosci.* **2006**, *24*, 105–115.

(53) Bray, D.; Duke, T. Conformational spread: the propagation of allosteric states in large multiprotein complexes. *Annu. Rev. Biophys. Biomol. Struct.* **2004**, *33*, 53–73.

(54) Jarvis, M. F.; Khakh, B. S. ATP-gated P2X cation-channels. *Neuropharmacology* **2009**, *56*, 208–215.

(55) Egan, T. M.; Samways, D. S. K.; Li, Z. Biophysics of P2X receptors. *Pflugers Arch. EJP* **2006**, *452*, 501–512.

(56) Fujiwara, Y.; Kubo, Y. Density-dependent changes of the pore properties of the P2X2 receptor channel. *J. Physiol. (London)* **2004**, *558*, 31–43.

(57) Vial, C.; Roberts, J. A.; Evans, R. J. Molecular properties of ATP-gated P2X receptor ion channels. *Trends Pharmacol. Sci.* **2004**, *25*, 487–493.

(58) Eickhorst, A. N.; Berson, A.; Cockayne, D.; Lester, H. A.; Khakh, B. S. Control of $P2X_2$ channel permeability by the cytosolic domain. *J. Gen. Physiol.* **2002**, *120*, 119–131.

Appendix 1

Studies of a Conserved Proline Residue Near the Agonist-Binding Sites of the Muscle-Type Nicotinic Acetylcholine Receptor

A1.1 Introduction

The adult-form of the muscle-type nicotinic acetylcholine receptor (nAChR) is composed of 5 subunits, α-ε-α-δ-β, arranged around a central ion pore. Binding of acetylcholine (ACh) at the ligand-binding sites on the interfaces between the α/γ and α/ε subunits triggers a series of conformational changes that ultimately lead to ion conduction (Figure 1.1).

A genetic mutation Pro121Leu near the binding site on the ε subunit has been associated with a loss of function myasthenic syndrome (*1*), implicating an important role of this residue in the receptor function. εPro121 is located at the *C*-terminus of loop E, only two residues in sequence after Leu119 that has been identified as part of the *complementary* component of the binding site (Figure A1.1) (*2*, *3*). This places the proline within a Van der Waals contact of αTrp149,

the key binding residue that forms a cation-π interaction with ACh, on the *primary* binding site across the interface (*4*)

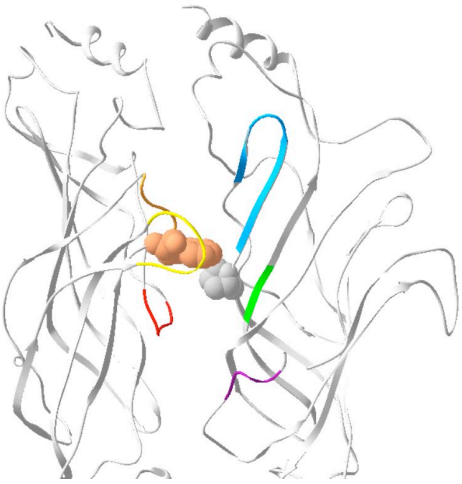

Figure A1.1. Ligand-binding domains of nAChR α- and γ-subunits (Protein Data Bank code 2BG9). On the α-subunit, loop A (α92-α98, *Torpedo* numbering) is highlighted in red, loop B (α149-α154) in orange, and loop C (α189-α196) in yellow. On the γ-subunit, loop D (γ53-γ55), loop E (γ108-γ118), and loop F (γ173-γ177) are highlighted in green, blue, and purple, respectively. αTrp149 is shown in orange and γPro120 in grey.

Pro121 is the second proline of the Pro-Pro pair that is highly conserved among nAChR subunits. (There is no equivalent proline in any of the acetylcholine-binding protein (AChBP) isoforms.) An analysis of protein structures shows that 87% of *cis* peptide bonds are preceding Pro residues, of which a Pro-Pro bond has the highest frequency (11.2%) to be in the *cis* form (*5*). As such, we speculated that *cis-trans* isomerization may occur at the amide bond between these Pro-Pro residues. We performed conventional and unnatural mutagenesis studies at this residue, and the function of the mutant receptors was

probed using electrophysiology. We find that subtle mutations at this site resulted in substantial functional perturbations, although it is unlikely that *cis-trans* isomerization was involved at this proline.

A1.2 Results and Discussion

The Dougherty Lab conventionally employs the embryonic form of the muscle-type nAChR, with the γ-subunit instead of the ε-subunit of the adult form. Likewise, the present mutagenesis studies were performed on the embryonic α-γ-α-δ-β nAChR. We made mutations on both the γ- and δ-subunit at the same time to avoid any ambiguity that could possibly arise from asymmetric binding sites (*6-9*), unless otherwise specified. εPro121 is equivalent to γPro120 and δPro123 in the mouse muscle nAChR, and all these equivalent residues are referred to as Pro121 throughout this chapter for simplicity.

Incorporation of unnatural amino acid analogs of proline at γ,δPro121

To examine the role of *cis-trans* isomerization at Pro121 in receptor function, we first substituted this residue with a number of unnatural amino acid analogs of proline with varying preferences for the *cis* conformer via the *in vivo* nonsense-suppression methods (Figure A1.2). Most of these unnatural amino acids were used in previous studies (*10*, *11*). If the *cis* conformer of Pro121 contributed to the receptor function, a linear energy correlation between the *cis-*

trans energy gap and the energy of channel activation would be expected, similar to the correlation seen in Ref. (*11*).

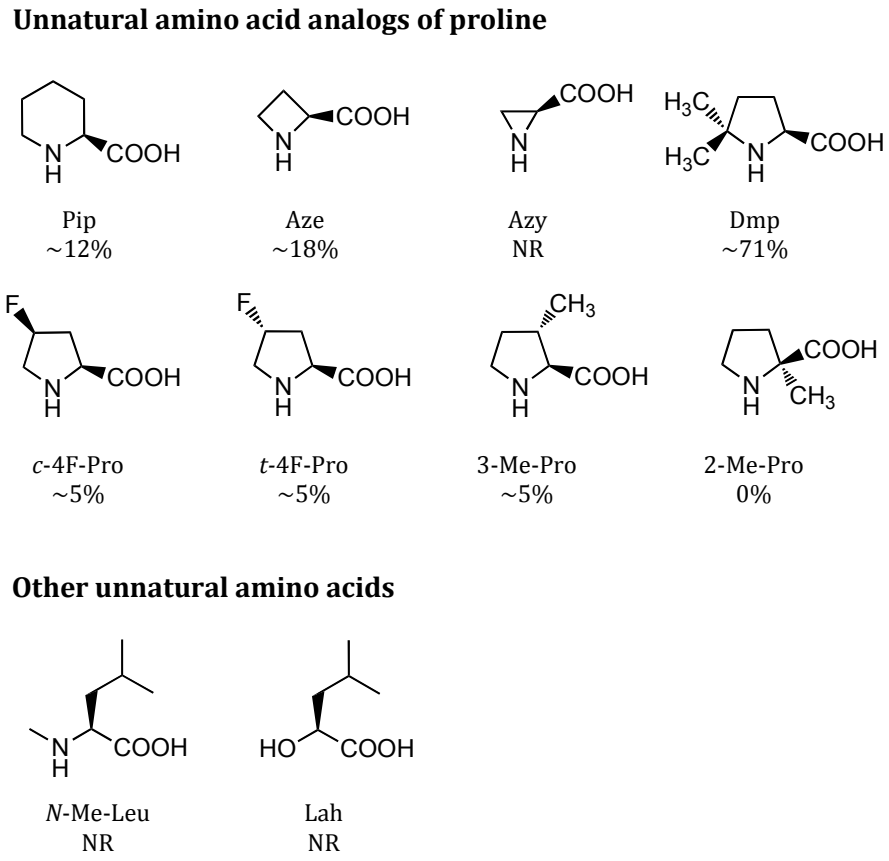

Figure A1.2. Structures of unnatural amino acids studied at the position 121 with the reported percent *cis* (*11*, *12*). Proline is set to 5%, which is the value obtained from statistical surveys of protein structures. NR, percent *cis* not reported

As a positive control, the first nonsense-suppression experiment was the "wild-type recovery," in which the suppressor tRNA was charged with proline. When function of this wild-type rescue receptor was evaluated in comparison to the true wild type, the full phenotype of the wild-type receptor was successfully

recovered, including the EC_{50} value, the Hill constant, and the current traces (data not shown).

We used EC_{50} as a measurement of the receptor function. We found that the EC_{50} values of these mutant receptors displayed no correlation with the *cis*-*trans* energy gaps of the proline analogs (Table A1.1). Incorporation of Pip, which has 12% preference for the *cis* conformer, produced a receptor with a 10-fold decrease in EC_{50} from the wild-type value, whereas, incorporation of Aze, which has 18% preference, resulted in a 14-fold increase in EC_{50}. These data suggest that *cis*-*trans* isomerization at Pro121 is not involved in the receptor function.

Because both Pip and Aze, which were considered subtle mutations, had substantial effects on the EC_{50} values, it would be worthwhile to explore the significance of this proline residue further by incorporating additional unnatural proline analogs. Substituting Pro121 with *c*-4F-Pro or *t*-4F-Pro produced a receptor with an EC_{50} value comparable to the wild type. The results indicate that the ring conformation of this side chain is not important, as these two unnatural amino acids prefer different pyrrolidine-ring puckers (*13*). In addition, both Pro121(3-Me-Pro) and Pro121(2-Me-Pro) mutations also produced a near wild-type EC_{50}. With the 2-Me-Pro being strongly *trans*-biased, the result of the 2-Me-Pro mutation confirms that the *cis* conformer of Pro121 does not play a role in the receptor activation. Many attempts were made to incorporate Dmp at this site, but no signal above the background level was observed.

Table A1.1. ACh EC_{50} and Hill constants of mutant receptors containing unnatural amino acid analogs of proline at the residue 121 in both γ- and δ-subunits

γ,δ P121	EC_{50}	Hill Constant	*n*	EC_{50}(mutant)/EC_{50}(wild type)
	(μM)			
Wild type	21.5 ± 0.72	1.53 ± 0.07	8	1.0
Pip	1.89 ± 0.05	1.38 ± 0.04	12	0.1
Aze	299 ± 13	1.60 ± 0.09	6	14
c-4F-Pro	28.6 ± 0.63	1.51 ± 0.04	8	1.3
t-4F-Pro	15.8 ± 0.40	1.67 ± 0.06	7	0.7
3-Me-Pro	19.3 ± 0.54	1.49 ± 0.05	8	0.9
2-Me-Pro	23.2 ± 0.90	1.56 ± 0.08	5	1.1

A trend in receptor function is seen with the ring sizes at the side chain at the residue 121. Mutating this residue to Aze, with a 4-membered ring, increased the EC_{50} from the wild type, while the mutation to Pip, with a 6-membered ring, decreased the EC_{50}. All other proline analogs contain a 5-membered ring, and the corresponding mutant receptors exhibited activities similar to the wild type. As such, we considered obtaining an additional data point from another different ring size. Neither a 3-membered ring (aziridine) nor a 7-membered ring (azepine) had previously been utilized in unnatural amino acid mutagenesis in the Dougherty Lab or elsewhere. With the 7-membered ring, we were concerned about ring flexibility that could obscure the analysis, and therefore, we decided to incorporate aziridine (Azy) at residue 121. The preparation of tRNA-Azy is described in **Appendix 2**. Many attempts were made to express a mutant nAChR containing Azy at this site. However, no valid data could be obtained from the Azy-mutant receptor.

Unsuccessful experiments with Dmp and Azy at the Pro121 site were possibly a result of (*i*) intrinsic difficulties of Dmp or Azy expression in *Xenopus* oocytes and (*ii*) the highly permissive nature of the Pro121 site which allowed incorporation of other endogenous amino acids via the *read-through* and/or the *reacylation* mechanisms (*14*). The structural constraints of Dmp and Azy possibly reduced the efficiencies of protein translation on the ribosome, protein folding, and/or subunit assembly.

Conventional mutagenesis at γ,δPro121

Conventional mutagenesis studies were performed at Pro121 to further investigate receptor function in response to different sizes of side chains at this position. The selected side chains included Leu, which causes the congenital myasthenic syndrome, as well as Trp and Gly, which, respectively, bear the largest and the smallest side chains among the 20-natural amino acids. In addition, we tested Ala and Ser, which are present at the equivalent position of the AChBPs.

All of the conventional mutations at position 121 had impaired receptor activities as suggested by the increase in EC_{50} values (Table A1.2). Surprisingly, the effect of the leucine mutation was the smallest of all, causing only a 5-fold increase in EC_{50} from the wild-type value. The EC_{50} of the receptor with Pro121Ala was greater than that of Pro121Leu, following the size trend. However, the EC_{50} of the serine mutant, which was expected to fall between those of Leu and Ala, was in fact larger than both values. This can possibly be explained by the polarity

effect of the serine side chain. Mutations of Pro121 to Trp or Gly severely disrupted receptor function, raising the EC_{50} greater than 20-fold. Overall, these results suggest that position 121 requires a hydrophobic side chain with a proper size and shape for the receptor to function normally.

Table A1.2. EC_{50} values and Hill constants of conventional mutant nAChR at the residue 121 in both γ- and δ-subunits in response to ACh

γ,δ P121	**EC_{50}**	**Hill Constant**	***n***	**EC_{50}(mutant)/EC_{50}(wild type)**
	(μM)			
Leu	154.3 ± 7.8	1.38 ± 0.08	5	7.2
Ala	244.5 ± 3.6	1.52 ± 0.03	11	11.4
Gly	537.2 ± 12.2	1.48 ± 0.04	11	25.0
Ser	349.5 ± 10.2	1.41 ± 0.05	6	16.2
Trp	449.3 ± 18.2	1.43 ± 0.06	5	20.9

Incorporation of unnatural analogs of leucine at γ,δPro121

Another unique property of proline among all natural amino acids is that proline cannot act as a hydrogen-bond donor because the amino group of proline is alkylated within the ring. To investigate the importance of this special feature at position 121, we incorporated two unnatural analogs of leucine, Lah and *N*-Me-Leu (Figure A1.2). The resulting mutant receptor functions would be evaluated in comparison to the Pro121Leu mutant, not the wild-type receptor. Both *N*-Me-Leu and Lah cannot donate a hydrogen bond; *N*-Me-Leu contains a methyl group on the backbone amide nitrogen, and Lah has a hydroxy group

replacing the amino group of leucine. The EC_{50} values resulting from the Pro121Lah and Pro121(*N*-Me-Leu) mutations were comparable to the EC_{50} of the Leu mutant (Table A1.3). Therefore, neither the hydrogen-bond donating ability nor the *N*-alkylation is important at this residue.

Table A1.3. ACh EC_{50} and Hill constants of mutant receptors containing unnatural analogs of leucine at the residue 121 in both γ- and δ-subunits

γ,δ P121	**EC_{50}**	**Hill Constant**	***n***	**EC_{50}(mutant)/EC_{50}(wild type)**
	(μM)			
N-Me-Leu	103 ± 2.1	1.37 ± 0.03	6	4.8
Lah	132 ± 4.6	1.34 ± 0.05	7	6.1

Current traces of nAChR containing mutations at γ,δPro121

Even though the two-electrode voltage-clamp method records macroscopic current and does not allow a direct measurement of kinetic parameters, the waveform of the current traces still provides useful information on the gating kinetics. Normally, the muscle-type nAChR ion channel opens fast, followed by some level of desensitization (Figure A1.3, *left*). When Pro121 was mutated to a non-proline residue, the receptor lost the rapid opening. The most striking case was that of the glycine mutation, which produced receptors that opened extremely slowly (Figure A1.3, *right*). Some other mutations, including Aze, resulted in receptors that desensitized significantly less (Figure A1.3, *middle*) compared to the wild type. A remarkable change in the gating mechanism is

implicated here. However, detailed examination of ion channel kinetics requires single channel experiments and is beyond the scope of this study.

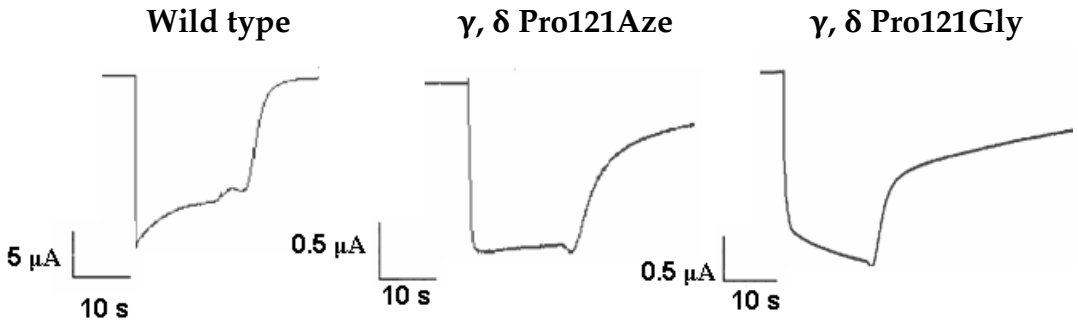

Figure A1.3. Representative current traces recorded at a saturating dose of ACh for the wild-type and the mutant nAChRs expressing Aze or Gly at the position 121 in the γ- and δ-subunits

Mutational studies at Pro121 in a single subunit

We performed mutational studies at position 121 on each subunit separately to gain a better insight into its role in receptor gating. γPro121Pip and δPro121Pip mutations produced comparable EC_{50} values, as did the Aze mutations, suggesting that both complementary subunits responded to these mutations in parallel (Table A1.4). For both Pip and Aze, the single mutations in γ and δ produced effects that were roughly half of what was seen with the double mutations (Table A1.1 and A1.5), suggesting that the effect of the single mutations at Pro121 on the complementary subunits are additive.

Since Pro121 is highly conserved among the nAChR subunits, we also tested whether or not the large effect on the EC_{50} was specific to the mutations on the complementary subunits. When we mutated Pro121 on the α-subunits to leucine, the mutant receptor had a comparable EC_{50} to the wild type. The result suggests that only the Pro121 in the complementary subunits, not the principal subunits, are functionally important in the gating mechanism.

Table A1.4. EC_{50} values and Hill coefficients of Pro121 mutations in a single nAChR subunit

Subunits	Residue 121	EC_{50}	Hill Constant	*n*	EC_{50}(mutant)/EC_{50}(wild type)
		(μM)			
α	Leu	30.7 ± 0.61	1.35 ± 0.03	7	1.4
γ	Pip	5.9 ± 0.14	1.44 ± 0.04	13	0.3
γ	Aze	117 ± 5	1.35 ± 0.06	6	5.4
δ	Pip	5.4 ± 0.14	1.47 ± 0.05	9	0.2
δ	Aze	175 ± 9	1.46 ± 0.09	5	8.1

Summary

A number of conventional and unnatural amino acids were incorporated at residue Pro121 in the complementary γ and δ subunits of the muscle-type nAChR. A number of these mutations resulted in a dramatic shift in the ACh EC_{50}. These EC_{50} values do not demonstrate any correlation between the functions of the mutant receptors and the *cis* preferences of the amino acids, and therefore, *cis-trans* isomerization is not involved at this site. A cyclic side chain is

required at this position for the fast channel opening, as suggested qualitatively by the current traces. Structure and volume of side chains were found to be important to the proper function of the receptor, although their precise roles cannot be inferred from these types of experiments. Furthermore, the analogous mutation on the principal α-subunits did not affect receptor function, implicating that the importance of this residue is limited to the complementary components of the binding sites.

A1.3 Materials and Methods

Molecular biology

Subunits of mouse muscle nAChR were expressed in pAMV vectors and site-directed mutagenesis was performed using a standard Stratagene QuikChange protocol. Circular cDNA was linearized with NotI or KpnI. After purification (Qiagen), linearized DNA was used as a template for runoff in vitro transcription using T7 mMessage mMachine kit (Ambion). The resulting mRNA was purified (RNAeasy Mini Kit, Qiagen) and quantified by UV-visible spectroscopy. Wild-type subunits were subjected to the same linearization and transcription steps to give mRNA for all subunits.

THG73 (*14*) was used as amber suppressor tRNA for unnatural amino acid (uAA) incorporation. Conjugated dCA-uAA was ligated to 74 nucleotide tRNA as previously reported (*15*). Crude tRNA product was used without desalting, and the product was confirmed by MALDI-TOF MS on 3-

hydroxypicolinic acid (3-HPA) matrix. Deprotection of tRNA-uAA was carried out immediately prior to injection by 5-minute photolysis (NVOC protection). No deprotection was required for α-hydroxy uAA.

nAChR expression

For wild-type receptor and receptors containing conventional mutation, quantified mRNA of all subunits were mixed in a ratio of α:β:γ:δ = 2:1:1:1 by mass, according to the subunit stoichiometry of the receptor. The ratio of subunits in the mRNA was 5-fold biased toward the subunit containing the site for unnatural amino acid. For example, if an unnatural amino acid was to be incorporated into the γ-subunit, the stoichiometry of mix mRNA will be α:β:γ:δ = 2:1:5:1 by mass. Typically, total mRNA concentrations used were 0.01–0.05 μg/μL for wild-type receptor, 0.1–1.0 μg/μL for conventional mutations, and 0.5–2.5 μg/μL for suppression mutations. Prior to injection, equal volumes of the mRNA mixture and unprotected tRNA-uAA were mixed thoroughly. Each oocyte was injected with 50 nL of RNA solution, and cells were incubated for 18–72 hours at 18 °C in culture media ($ND96^+$ with 5% horse serum.)

Electrophysiological Recordings

Acetylcholine chloride was purchased from Sigma/Aldrich/RBI (St. Louis, MO). ACh was prepared as 1M stock solution in sterile, distilled, deionized water and stored at −20 °C. All drug dilutions were prepared in the calcium-free ND96 buffer from stock solutions.

Ion channel function in oocytes was assayed by current recording in two-electrode voltage-clamp mode using the OpusXpress 6000A (Axon Instruments). Cells were perfused in calcium-free ND96 solution at flow rates of 1 and 4 mL/min during agonist application and 3 mL/min during wash. Oocytes were typically clamped at −60 mV, but the holding potential was adjusted to −40 mV or −80 mV if the observed current was too large or too small, respectively. Drug application was 15 seconds in duration. For dose-response experiments, 1mL of each drug solution was applied to the cells, and between 12 and 16 concentrations of drug were used. All dose-response data were obtained from at least 5 cells and at least two batches of oocytes.

Data analysis

Data obtained from dose-response experiments were normalized ($I_{max} = 1$) and averaged. EC_{50} and Hill coefficient (n_H) were determined by fitting averaged, normalized dose-response relations to the Hill equation: $y = m/(1+(EC_{50}/x)^{n_H})$. Dose response of individual oocytes was also examined and used to determine outliers. For nAChR, individual dose-response data with $n_H > 2$ or $n_H < 1$ was discarded.

A1.4 References

(1) Ohno, K.; Wang, H. L.; Milone, M.; Bren, N.; Brengman, J. M.; Nakano, S.; Quiram, P.; Pruitt, J. N.; Sine, S. M.; Engel, A. G. Congenital myasthenic syndrome caused by decreased agonist binding affinity due to a mutation in the acetylcholine receptor epsilon subunit. *Neuron* **1996**, *17*, 157–170.

(2) Celie, P. H. N.; van Rossum-Fikkert, S. E.; van Dijk, W. J.; Brejc, K.; Smit, A. B.; Sixma, T. K. Nicotine and carbamylcholine binding to nicotinic acetylcholine receptors as studied in AChBP crystal structures. *Neuron* **2004**, *41*, 907–914.

(3) Blum, A. P.; Lester, H. A.; Dougherty, D. A. Nicotinic pharmacophore: the pyridine N of nicotine and carbonyl of acetylcholine hydrogen bond across a subunit interface to a backbone NH. *Proc. Natl. Acad. Sci. U.S.A.* **2010**, *107*, 13206–13211.

(4) Zhong, W.; Gallivan, J. P.; Zhang, Y.; Li, L.; Lester, H. A.; Dougherty, D. A. From ab initio quantum mechanics to molecular neurobiology: A cation- binding site in the nicotinic receptor. *Proc. Natl. Acad. Sci. U.S.A.* **1998**, *95*, 12088–12093.

(5) Pal, D.; Chakrabarti, P. Cis peptide bonds in proteins: residues involved, their conformations, interactions and locations. *J. Mol. Biol.* **1999**, *294*, 271–288.

(6) Prince, R. J.; Sine, S. M. Epibatidine activates muscle acetylcholine receptors with unique site selectivity. *Biophys. J.* **1998**, *75*, 1817–1827.

(7) Prince, R. J.; Sine, S. M. Epibatidine binds with unique site and state selectivity to muscle nicotinic acetylcholine receptors. *J. Biol. Chem.* **1998**, *273*, 7843–7849.

(8) Prince, R. J.; Sine, S. M. Molecular dissection of subunit interfaces in the acetylcholine receptor. Identification of residues that determine agonist selectivity. *J. Biol. Chem.* **1996**, *271*, 25770–25777.

(9) Jackson, M. B. Perfection of a synaptic receptor: kinetics and energetics of the acetylcholine receptor. *Proc. Natl. Acad. Sci. U.S.A.* **1989**, *86*, 2199–2203.

(10) Dang, H.; England, P. M.; Farivar, S. S.; Dougherty, D. A.; Lester, H. A. Probing the role of a conserved M1 proline residue in 5-hydroxytryptamine$_3$ receptor gating. *Mol. Pharmacol.* **2000**, *57*, 1114–1122.

(11) Lummis, S. C.; Beene, D. L.; Lee, L. W.; Lester, H. A.; Broadhurst, R. W.; Dougherty, D. A. Cis-trans isomerization at a proline opens the pore of a neurotransmitter-gated ion channel. *Nature* **2005**, *438*, 248–252.

(12) Dugave, C.; Demange, L. Cis-trans isomerization of organic molecules and biomolecules: implications and applications. *Chem. Rev.* **2003**, *103*, 2475–2532.

(13) Kim, W.; Hardcastle, K. I.; Conticello, V. P. Fluoroproline flip-flop: regiochemical reversal of a stereoelectronic effect on peptide and protein structures. *Angew. Chem., Int. Ed.* **2006**, *45*, 8141–8145.

(14) Saks, M. E.; Sampson, J. R.; Nowak, M. W.; Kearney, P. C.; Du, F.; Abelson, J. N.; Lester, H. A.; Dougherty, D. A. An engineered Tetrahymena tRNAGln for in vivo incorporation of unnatural amino acids into proteins by nonsense suppression. *J. Biol. Chem.* **1996**, *271*, 23169–23175.

(15) Dougherty, D. A. Unnatural amino acids as probes of protein structure and function. *Curr. Opin. Chem. Biol.* **2000**, *4*, 645–652.

Appendix 2

Preparation and Incorporation of Aziridine, a Novel Unnatural Amino Acid, into Cys-Loop Receptors

A2.1 Introduction

Aziridine carboxylate (Azy) is a 3-membered ring analog of proline. The results of our studies on nAChR Pro121 (**Appendix 1**) led to the aspiration to have a proline analog with a smaller ring size than what was already available. Aside from being the smallest cyclic amino acid possible, Azy also has several unique structural features with respect to other amino acids because of the steric constraint posted by the small ring size. For example, the hybridization of the aziridine nitrogen is altered to an sp^3-like structure to accommodate the ring strain (*1*). The conjugation is maintained but is weaker than a normal amide bond. As a result, the rotational barriers are so small that the energy gap between the '*cis*-like' and the '*trans*-like' structures cannot be accessed experimentally by means of dynamic NMR methods (*2*, *3*).

A procedure for preparation of tRNA-Azy was previously unavailable. As such, this chapter focuses on the synthesis of dCA-Azy. The amino acid was

incorporated into the 5-HT_{3A} receptor via the *in vivo* nonsense-suppression methodology to demonstrate the viability of this new unnatural amino acid.

A2.2 Results and Discussion

Synthesis of dCA-Azy

Like the first step of any other unnatural amino acid incorporation, dCA-Azy must be synthesized. Starting from the commercially available aziridine-2-carboxylic acid methyl ester, the amine was first protected as 4-pentenoyl (4-PO), using 4-pentenoic anhydride in the presence of DIPEA (Figure A2.1) (*4*, *5*). Saponification of the methyl ester with potassium trimethylsilanolate was expected to produce carboxylate **(III)**. Although aziridine carboxylate was found to be stable without the methyl ester, the *N*-protected aziridine-2-carboxylate **(III)** decomposed instantaneously. This suggested an incompatibility between the *N*-protected aziridine and the carboxylate group. The 4-PO group was utilized as a protecting group for the amine instead of the standard nitroveratryloxycarbonyl (NVOC) group because we found that the 4-PO protected aziridine carboxylate was less unstable than the NVOC-protected molecule. The crude product **(III)** was used *immediately* in the next reaction.

The carboxylate was activated as a cyanomethyl ester, following the established procedure (*5*), for coupling to the dCA dinucleotide. The described synthesis route yielded a sufficient amount of the cyanomethyl ester **(IV)** for this purpose. The purified product was characterized by ^{1}H NMR, ^{13}C NMR, and

high-resolution mass spectrometry. Following the standard protocols previously reported by others in the Dougherty group, dCA-Azy and tRNA-Azy were successfully prepared and characterized (*5*, *6*).

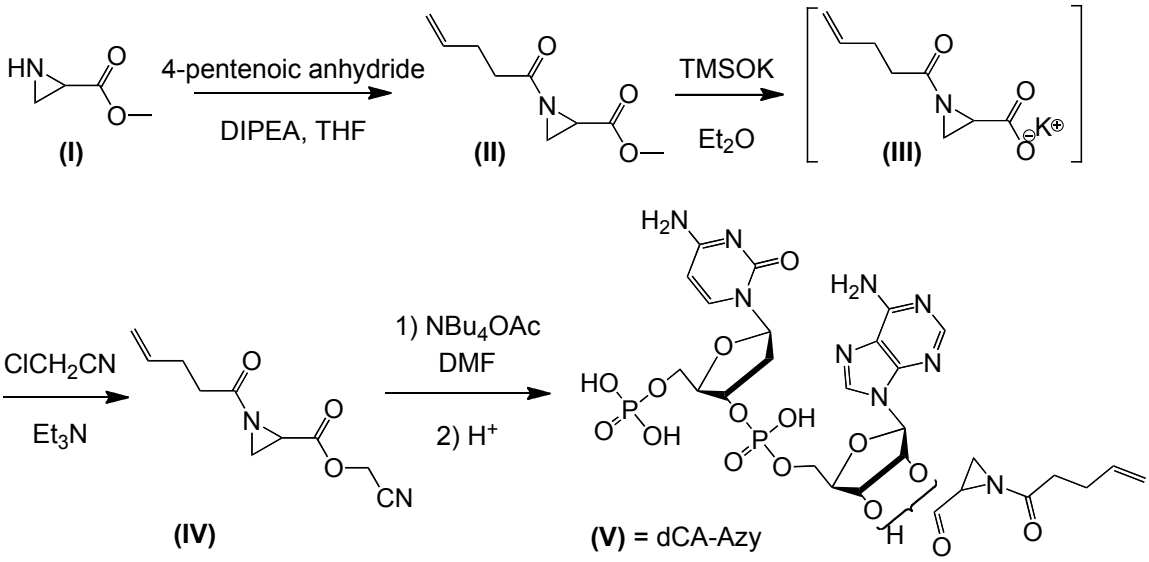

Figure A2.1. A scheme for dCA-Azy synthesis

Incorporation of Azy into a functional Cys-loop receptor

The mechanism for the 4-PO deprotection by I_2 requires delocalization of the amide nitrogen π-electron onto the C–N bond. Therefore, removal of the 4-PO protecting group from aziridine was expected to be difficult due to the sp^3-like structure that weakens the π conjugation. Analysis of model deprotection reactions by ^{1}H NMR or MALDI-TOF mass spectrometry confirmed the inefficiency of the reaction. Because the I_2 deprotection of the 4-PO-Azy was not as efficient as typical amides, special care was required. The 4-PO protecting

group was removed from the tRNA-Azy immediately prior to oocyte injection by treatment with a freshly made saturated I_2 solution in water (*4*, *5*). Pre-made I_2 solution was found to be ineffective. The mixture was incubated at room temperature for 15 minutes or more, longer than the standard procedure for 4-PO deprotection.

Expression of Azy-containing Cys-loop receptor

Initial attempts to incorporate Azy at the Pro121 sites on the γ,δ-subunits of nAChR resulted in inconsistent EC_{50} values and a low Hill constant, suggesting a mix receptor population. The source of this problem was later recognized to be the read-through and/or the reacylation process. In order to prove that Azy could be incorporated into a functional protein via the nonsense-suppression methodology, we sought a non-promiscuous site where no unwanted endogenous amino acid could produce a functional receptor. The proline 8* in the M2-M3 loop of the 5-HT_{3A} serotonin receptor was an excellent candidate, because only proline analogs that could undergo *cis-trans* isomerization functioned at this site (*7*). We decided to incorporate Azy at this position, and we found the resulting current level to be very low but still measurable, with $I_{max} \approx 100$ nA.

The oocytes expressing the mutant 5-HT_{3A} receptor suppressed with Azy displayed an EC_{50} that was 2-fold lower than the wild-type oocytes (Table A2.1). Previous work by Lummis, *et al.* demonstrated a linear correlation in energy between the intrinsic *cis-trans* energy gap of the proline analog and the activation of the receptor (*7*). Therefore, with the observed gain-of-function effect, the

observed current likely came from the Azy-containing mutant receptors, not a product of unwanted read-through or reacylation.

Table A2.1. EC_{50} and Hill coefficients of wild-type and Pro308Azy mutant 5-HT_{3A} receptors in response to 5-HT (serotonin)

Residue 308	EC_{50}	Hill Constant	*n*	EC_{50}(mutant)/EC_{50}(wild type)
	μM			
Pro	1.38 ± 0.05	2.76 ± 0.24	10	1.0
Azy	0.73 ± 0.02	3.06 ± 0.22	6	0.5

While the wild-type 5-HT_{3A} receptor typically opens and desensitizes slowly, the Azy-mutant receptor exhibited current traces that were both fast opening and fast desensitizing (Figure A2.2). In the case of Azy, desensitization probably occurred before the maximal current was attained, and this likely instigated some error in the EC_{50} measurement. The low rotational barrier of the Azy amide bond was perhaps the underlying cause of the altered kinetic behavior — the rapid conformational change at the Azy backbone amide facilitated the rapid movement of the M2 helix containing the gate that opened and closed the ion pore.

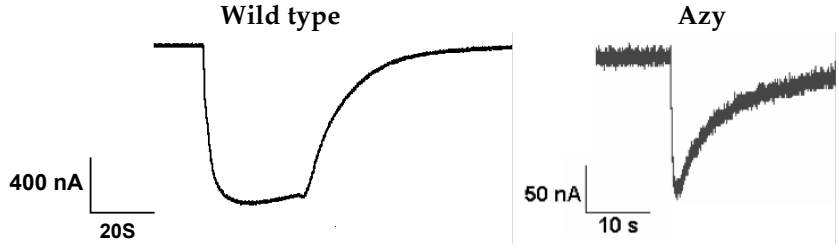

Figure A2.2. Whole cell current traces at saturating concentration of serotonin from *Xenopus* oocytes expressed with wild-type 5-HT_{3A} receptor (*left)* or mutant 5-HT_{3A} receptor contaning Azy at the residue 308 (*right*).

Concluding Remarks

We have demonstrated that the novel unnatural amino acid, Azy, could be prepared and incorporated into a functional 5-HT_{3A} receptor via the nonsense-suppression method. However, the current observed was small. The unique structure of the residue posed several challenges in chemical synthesis, as previously mentioned, and also in protein expression. Because of the shape of the ring, the carbonyl carbon became more susceptible to hydrolysis, which could deplete the tRNA-Azy population. The unusual structure might not allow the amino acid to interact properly to the ribosome during the translation. Moreover, the Azy-containing peptide might be difficult to fold properly because the Azy amide bond did not have the preferred sp^2 hybridization. Nevertheless, this experiment has shown that the Azy-containing receptors could be produced and transported to the cell membrane successfully. To our knowledge, Azy was the first unnatural amino acid with a twisted amide bond that had been incorporated into a functional protein *in vivo*.

A2.3 Materials and Methods

Chemical Synthesis

***N*-4-pentenoyl-aziridine-2-carboxylic acid methyl ester (II).** *N, N*-diisopropylethylamine (DIPEA, 0.61 mL, 3.32 mmole, 1.2 eq) and aziridine-2-carboxylic acid methyl ester (1, 0.25 mL, 2.77 mmole, 1.0 eq) were dissolved in 27 mL of anhydrous THF. To the stirring reaction, solution of pentenoic anhydride

(0.61 mL, 3.32 mmole, 1.2 eq) in 1 mL anhydrous THF was added, and the vial was rinsed with additional anhydrous THF (2 × 1 mL) to ensure qualitative transfer of the reagent. The reaction was monitored by TLC (7:3 hexanes/ethyl acetate, R_f = 0.28). The reaction was stirred ambient temperature for 6 hours. The THF was removed under reduced pressure. Crude product was purified by silica gel flash chromatography (8:2 hexanes/ethyl acetate, and 95:5 toluene/acetone, R_f = 0.3 in separate columns).

^{1}H NMR (300 MHz, $CDCl_3$) δ ppm: 2.40–2.61 (6H, m), 3.15 (1H, dd), 3.80 (3H, s), 4.99–5.11 (2H, m), 5.77–5.90 (1H, m). ^{13}C NMR (75 MHz, $CDCl_3$) δ ppm: 28.55, 30.57, 34.05, 35.86, 52.71, 115.58, 136.73, 168.80, 182.51.

ESI MS: calcd for $[M+Na]^+$ m/z = 206.1, found 205.9.

***N*-4-pentenoyl-aziridine-2-carboxylate, potassium salt (III).** Potassium trimethylsilylnolate (0.2818 g, 2.20 mmole) was azeotroped 3 times in toluene. To the dried solid, 20 mL of anhydrous diethyl ether was added. The temperature was dropped to −78 °C. Solution of **(II)** (0.4129 g, 2.25 mmole) in 5 mL of diethyl ether was added to the stirred reaction while cold. The reaction was stirred at −78 °C for 4 hours and let stand at −80 °C overnight (~ 11 hours). The temperature was raised to room temperature. The mixture was sonicated and diluted with 50 mL of diethyl ether. Crude product was collected in a crude frit and washed excessively with either. Then the product was transferred into a flask using methanol, and the solvent was removed under reduced pressure. Toluene was added to the solution to ensure complete removal of solvents.

Crude product was immediately used in the next step without any purification or characterization.

***N*-4-pentenoyl-aziridine-2-carboxylic acid cyanomethyl ester (IV).** Crude mixture containing **(III)** from the previous step was azeotroped with toluene 3 times. Chloroacetonitrile (2 mL, 31.6 mmole) was added to the dried solid. The reaction was sonicated, followed by addition of triethylamine (1 mL, 7.2 mmole). The reaction was monitored by TLC (1:1 hexanes/ethylacetate, R_f = 0.53). After the reaction had been stirred at room temperature for 2 hours, diethyl ether was added to dilute the reaction. The mixture was washed with 2 × water and brine and dried over Na_2SO_4. Solvents were removed under reduced pressure, and crude product was purified by silica gel flash chromatography (gradient of 9:1 hexanes/ethylacetate and 1:1 hexanes/ethylacetate).

^{1}H NMR (300 MHz, $CDCl_3$) δ ppm: 2.40–2.67 (6H, m), 3.23 (1H, dd), 4.83 (2H, d), 5.00–5.12 (2H, m), 5.76–5.90 (1H, m).

^{13}C NMR (75 MHz, $CDCl_3$) δ ppm: 28.63, 31.45, 33.34, 35.98, 49.43, 113.85, 116.04, 136.61, 167.26, 182.34.

ESI MS: calcd for m/z = 209.0926, found 209.0921.

Coupling to dCA. dCA was synthesized as previously reported (52). dCA•TBA (13.1 mg, 0.020 mmole, 1 eq) was transferred into a tared 1-g vial. The vial was purged with argon 3 times. Under inert atmosphere, DMF was added, followed by addition of **(IV)** (11.4 mg, 0.055 mmole, 2.7 eq). The reaction was kept under

inert atmosphere and stirred overnight at room temperature. The reaction was monitored by analytical reversed phase HPLC. The reaction was quenched with 1:1 acetonitrile/water. The product was purified by reversed-phase HPLC (95:5 to 0:100 water/acetonitrile at 20 mL/min over 15 min). Fourteen fractions were collected, and solvents were removed by lyophilization. 10 mM acetic acid (~ 2 mL) was added to the dry solid, and the solvent was removed again by lyophilization. This process was repeated three times to ensure that the products were free from ammonium ion. The desired product was confirmed by ESI-TOF MS. R_t = 3.88 min and 4.17 min. calcd for $[M-H]^-$ m/z = 786.16, found 786.3.

Ligation of tRNA-Azy

Conjugated dCA-Azy was ligated to 74 nucleotide tRNA (THG73) as previously reported (*8*). Crude tRNA product was used without desalting, and the product was confirmed by MALDI-TOF MS on 3-hydroxypicolinic acid (3-HPA) matrix.

Expression of 5-HT_{3A} receptor

The 5-HT_{3A} receptor construct was in the pGEMhe vector. The mRNA encoding the wild-type 5-HT_{3A} receptor was kindly provided by K.S. Bower, and the mRNA containing a TAG-mutation at Pro308 was made by D.L. Beene. Deprotection of tRNA-Azy was carried out immediately prior to injection by 15-minute incubation with freshly made saturated I_2/water (tRNA-Azy: I_2/water = 1:1 by volume.) The ratio of subunits in the mRNA was 5-fold biased toward the subunit containing the site for unnatural amino acid. Final concentration of

wild-type 5-HT_{3A} receptor mRNA was 0.033 μg/μL. Prior to injection, equal volumes of the mRNA mixture and unprotected tRNA-Azy were mixed thoroughly. Each *Xenopus* oocyte was injected with 50 nL of RNA solution, and cells were incubated for 18–72 hours at 18 °C in culture media ($ND96^+$ with 5% horse serum).

Electrophysiological recordings

Ion channel function in *Xenopus* oocytes was assayed by current recording in two-electrode voltage-clamp mode using the OpusXpress 6000A (Axon Instruments). Cells were perfused in calcium-free ND96 solution at flow rates of 1 and 4 mL/min during agonist application and 3 mL/min during wash. The holding potential was set to −60 mV. 5-Hydroxytryptamine (5-HT) was kindly provided by K.S. Bower as a 25 mM stock solution. All drug dilutions were prepared in the calcium-free ND96 buffer from the stock solution. For dose-response experiments, 1mL of each drug solution was applied to the cells, and between 12 and 16 concentrations of drug were used. Drug application was 30 seconds in duration. All dose-response data were obtained from at least 5 cells and at least two batches of oocytes.

A2.4 References

(1) Shao, H.; Jiang, X.; Gantzel, P.; Goodman, M. Tilted amides in amino acid and peptide derivatives. *Chem. Biol.* **1994**, *1*, 231–234.

(2) Boggs, G. R.; Gerig, J. T. Nitrogen inversion in N-benzoylaziridines. *J. Org. Chem.* **1969**, *34*, 1484–1486.

(3) Anet, F. A. L.; Osyany, J. M. Nuclear Magnetic Resonance Spectra and Nitrogen Inversion in 1-Acylaziridines. *J. Am. Chem. Soc.* **1967**, *89*, 352–356.

(4) England, P. M.; Lester, H. A.; Davidson, N.; Dougherty, D. A. Site-specific, photochemical proteolysis applied to ion channels in vivo. *Proc. Natl. Acad. Sci. U.S.A.* **1997**, *94*, 11025–11030.

(5) Rothman, D.; Petersson, E.; Vazquez, M.; Brandt, G.; Dougherty, D.; Imperiali, B. Caged phosphoproteins. *J. Am. Chem. Soc.* **2005**, *127*, 846–847.

(6) Saks, M. E.; Sampson, J. R.; Nowak, M. W.; Kearney, P. C.; Du, F.; Abelson, J. N.; Lester, H. A.; Dougherty, D. A. An engineered Tetrahymena tRNAGln for in vivo incorporation of unnatural amino acids into proteins by nonsense suppression. *J. Biol. Chem.* **1996**, *271*, 23169–23175.

(7) Lummis, S. C.; Beene, D. L.; Lee, L. W.; Lester, H. A.; Broadhurst, R. W.; Dougherty, D. A. Cis-trans isomerization at a proline opens the pore of a neurotransmitter-gated ion channel. *Nature* **2005**, *438*, 248–252.

(8) Dougherty, D. A. Unnatural amino acids as probes of protein structure and function. *Curr. Opin. Chem. Biol.* **2000**, *4*, 645–652.

Appendix 3

Roles of the Conserved Phe233 in the Voltage Sensor of the Potassium Channels[1]

A3.1 Introduction

Voltage-sensitive ion channels are membrane proteins whose ion pores are open in response to the voltage differences across the cell membrane. These proteins play important roles in many cellular processes; voltage-dependent K^+ (Kv) and Na^+ (Nav) channels produce nerve impulses, and voltage-dependent Ca^{2+} (Cav) channels initiate muscle contraction. Voltage sensor domains are common components of these ion channels. For example, Kv channels consist of a central ion conduction pore surrounded by four voltage sensors (*1*–*4*). The voltage difference across the membrane is sensed through positively charged residues, mostly arginine but occasionally lysine, located on the fourth membrane-spanning helix (S4) of the voltage sensor domain (Figure A3.1A) (*5*, *6*). Movement of these charges in response to the change in the membrane

[1] The work described herein was done in collaboration with Xiao Tao, Alice Lee, and Professor Roderick MacKinnon at Rockefeller University, New York. This chapter is adapted in part from Tao, X.; Lee, A.; Limapichat, W.; Dougherty, D. A.; Mackinnon, R. A gating charge transfer center in voltage sensors. *Science* **2010**, *328*, 67–73.

potential leads to a global conformational change of the voltage sensor domain, and these conformational changes ultimately regulate the ion channel opening.

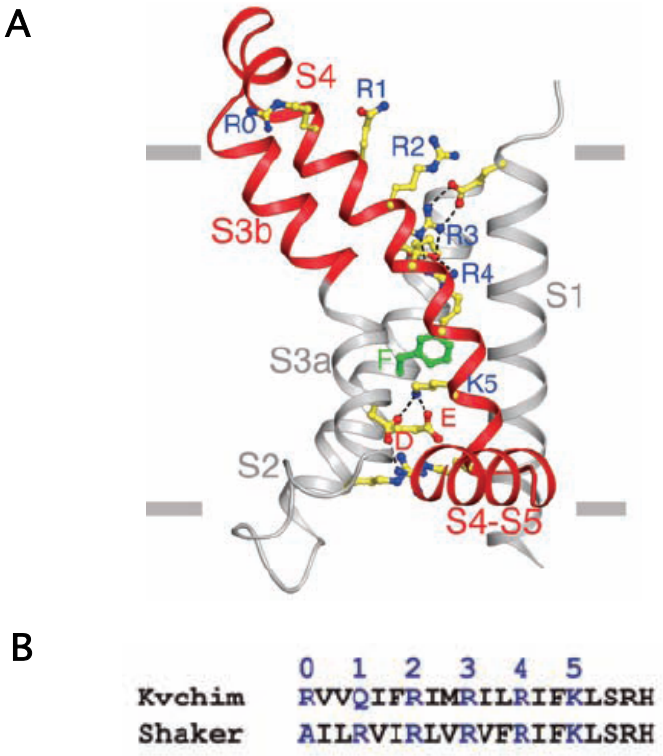

Figure A3.1. Topology of the positively charged residues R0–R4 and K5 on S4. **(A)** The voltage sensor and S4-S5 linker helix of the Kvchim in the open conformation. The conserved Phe233 is shown in green. **(B)** Sequence alignment of the S4 segment of Kvchim and *Shaker* Kv. The positively charged residues are colored blue.

In the crystal structure of an open-pore Kv2.1 paddle–Kv1.2 chimera channel tetramer (Kvchim, Protein Data Bank code 2R9R), positively charged amino acids are labeled 0 to 5, according to their position on S4 from outside to inside (Figure A3.1B). R0–R4 are in or near an extracellular surface-exposed environment. The next positively charged amino acid, K5, is different because it is isolated from the

external aqueous surface by the side chain of Phe233 (Figure A3.1, green side chain). The Phe is highly conserved across the voltage sensors from many different voltage-sensitive proteins, including Kv, Nav, Cav, voltage-dependent H^+ (Hv) channels and voltage-dependent phosphatase (VSP) enzymes (*7*).

This work was aimed to understand the role of Phe233 in the conformational change of the voltage sensor. This Phe had been suggested, based on structural data, to assist S4 movement (*4*). Particularly, an aromatic side chain could catalyze the transmembrane passage of S4 charges via a cation–π interaction, a noncovalent molecular interaction between the face of an electron-rich π system and an adjacent cation (*8*, *9*). As such, the enticing possibility that the cation–π interaction is involved in this system, i.e., between the side chain of Phe233 and the positively charged side chains on S4, was the main focus of this investigation. Conventional and unnatural amino acid mutagenesis was performed at this site, and the voltage-dependent activation of the mutant Kv channels was probed in the two-electrode voltage-clamp recordings. We find that a rigid cyclic side chain is important at Phe233, but aromaticity is not required.

A3.2 Results and Discussion

The following experiments were carried out on the *Shaker* K^+ channel instead of the paddle chimera channel. *Shaker* expresses to high levels in *Xenopus* oocytes, and it is the most extensively studied Kv channel with respect to gating

function (*10–13*). Even though the crystal structure of the *Shaker* K^+ channel has not been determined, the paddle chimera channel shares high sequence identity and therefore should serve as an accurate model for designing and analyzing experiments on the *Shaker* channel.

First, Phe233 was mutated to 19 other amino acids. The mutants fall into four groups according to the level of expressed current and the midpoint voltage (V_m) of the activation curve (Figure A3.2). Only two substitutions, Tyr and Trp, produced currents near wild-type levels with negative V_m. Only the three amino acids, Phe, Tyr, and Trp with a rigid cyclic side chain and aromaticity, support the highest current levels and negative V_m. This observation could stem from the unique size and shape of these side chains or the presence of the aromaticity. However, the results from conventional mutagenesis could not distinguish between these two cases.

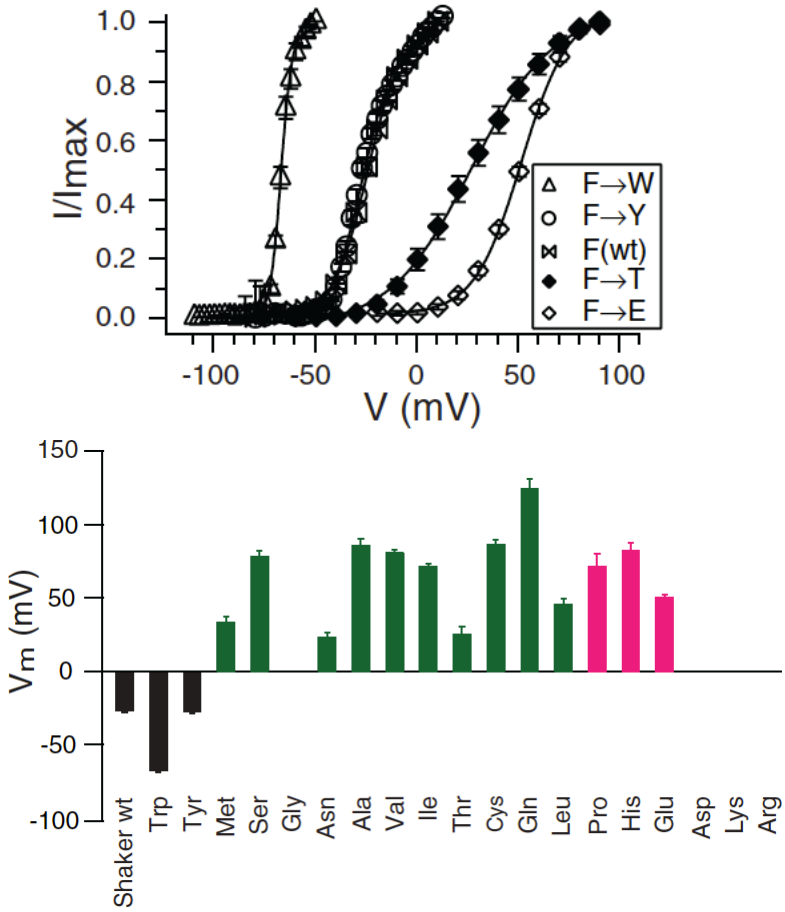

Figure A3.2. Voltage-dependent channel activation of the conventional Phe233 mutants. Representative voltage activation curves of *Shaker* wild type and mutants containing Trp, Tyr, Thr, or Glu at the position 233 (*top*). The fraction of the maximum activatable current (I/I_{max}, mean ± s.e.m.) is plotted as a function of the depolarization voltage (I–V plot) and fitted with the two-state Boltzmann function. (Wild type, $n = 11$; F→W, $n = 9$; F→Y , $n = 7$; F→T, $n = 4$; and F→E, $n = 9$) The V_m of *Shaker* wild type channel and *Shaker* channels with Phe233 mutated to other 19 natural amino acids (*bottom*). The mutants are grouped into four categories on the basis of expressed current level (indicated by the bar color: black, high current level; green, medium current level; magenta: low current level) and the value of V_m (indicated by the bar height). Oocytes expressing the Lys or Arg mutants did not produce any Agitoxin2-sensitive current. The expressed current level of the Asp mutant was too low to generate a usable I–V plot. V_m of the Gly mutant was not determined as its I–V plot cannot be fitted with the two-state Boltzmann function.

To test the possible existence of a cation–π interaction, we substituted Phe233 with a variety of unnatural amino acid analogues of Phe, including 3,5-F-Phe (F_2Phe), 4-methyl-Phe (MePhe), 4-cyano-Phe (CNPhe), 4-bromo-Phe (BrPhe) If the cation–π interaction exists, addition of an electron-withdrawing group on the aromatic ring is expected to produce a rightward shift in the voltage activation curves. However, our data revealed that all the unnatural Phe analogs consistently produced negative V_m values. Therefore, we did not observe any correlation between the mutant channel activities and the negative electrostatic potential on the surface of the aromatic ring (Figure A3.3 *top*).

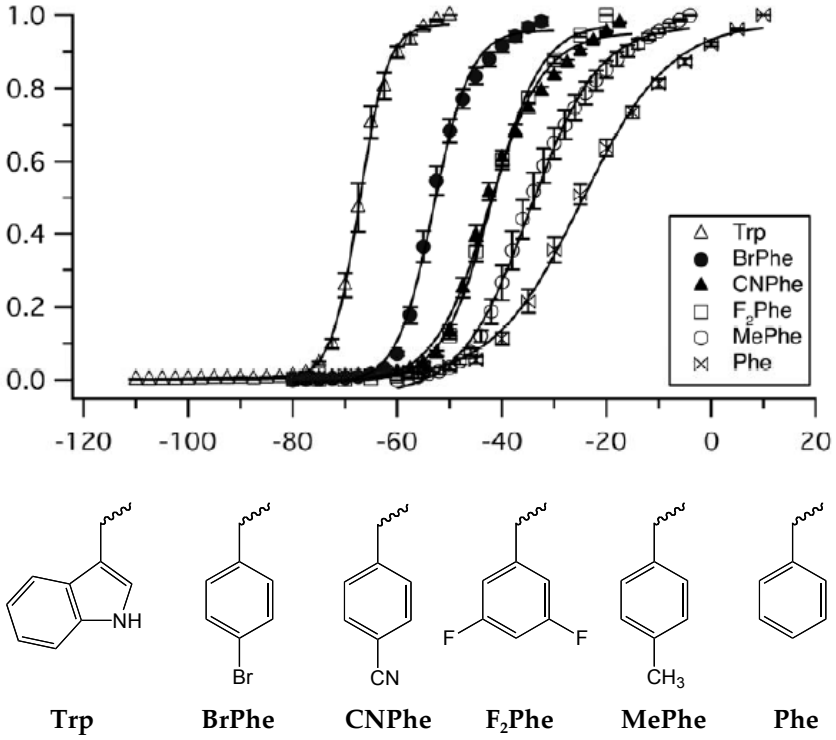

Figure A3.3. The voltage-dependent channel activation curves for Phe (*Shaker* wild type) and Phe to 3,5-F-Phe (F_2Phe), 4-bromo-Phe (BrPhe), 4-cyano-Phe (CNPhe), 4-methyl-Phe (MePhe), Trp mutants. Fraction of the maximal current (I/I_{max}, mean ± s.e.m.) is plotted as a function of the depolarization voltage and fitted with the two-state Boltzmann function (see methods, Phe, $n = 11$; F_2Phe, $n = 14$; BrPhe, $n = 10$; CNPhe, $n = 5$; MePhe, $n = 6$ and Trp, $n = 9$) The cation–π binding energy in kcal/mol: Trp −32.6, MePhe −28.5, BrPhe −27.6, Phe −27.1, F_2Phe −17.1 and CNPhe −15.7 (*9*). More negative binding energy means stronger cation–π interaction. Chemical structures of the side chains are shown below the I–V plot.

Furthermore, we tested the importance of aromaticity by substituting Phe233 with cyclohexylalanine (Cha), which has a rigid cyclic side chain but is not aromatic. The result yielded functional channels with a negative V_m, much like channels with Phe, Tyr, and Trp (Figure A3.4). Altogether, these results suggest that a rigid cyclic side chain is important at this position but aromaticity is not, and there is no evidence for the existence of the proposed cation–π interaction.

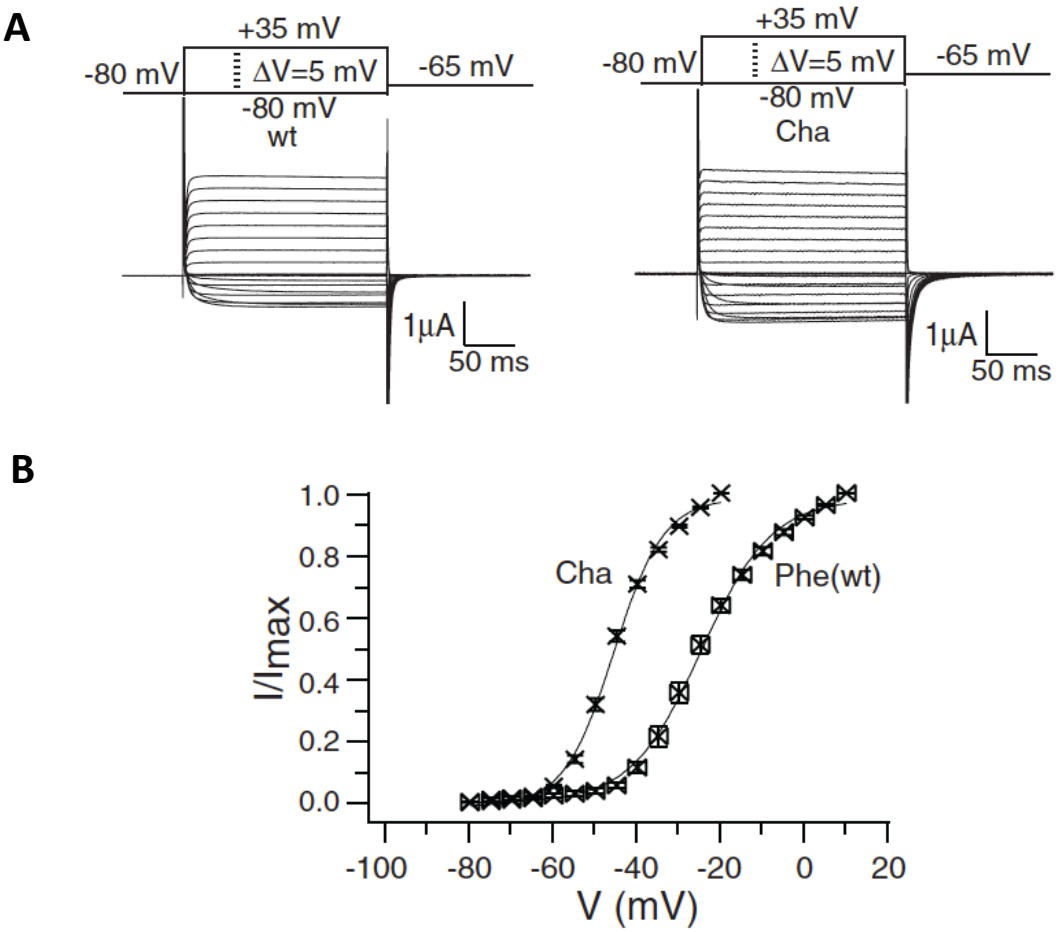

Figure A3.4. Voltage-dependent activation of the wild-type (Phe) and the cyclohexylalanine (Cha) mutant *Shaker* channels. **(A)** A representative current trace of the wild-type *Shaker* (left) and Cha mutant (right) recorded with a voltage-pulse protocol shown above. **(B)** The voltage activation curves of *Shaker* wt and the Cha mutant. The curves are fitted with the two-state Boltzmann function. (Wild type, $n = 11$; Cha, $n = 15$)

Another group later proposed that the F233W mutation could evoke a cation–π interaction between the Trp side chain and the gating charges (*14*). Their data showed a correlation between the V_m and the electronegative surface potential of tryptophan and fluorinated analogs of tryptophan, suggestive of a contribution of the cation–π interaction in the gating mechanism. They also

found that mutating K5 to Arg, which has a more diffuse positive charge than the Lys, weakened this cation–π interaction. Their results are consistent with our findings that K5R displayed a substantial increase in the V_m in the presence of the F233W background mutation (Figure A3.5). The Trp side chain likely preferred to form a cation–π interaction with the Lys than the Arg to stabilize the open state of the channel. Additionally, we found that the Lys mutation at R1, with the F233W background mutation, drastically increased the V_m of activation (Figure A3.5). The Lys was presumed to strengthen the cation–π interaction compared to the wild-type Arg. Therefore, the shift of the I–V curve to the right suggests that the R1K mutation perhaps stabilized the close state of the channel through the cation–π interaction.

The overall results are consistent with the presence of the cation–π interaction between the Trp side chain at residue 233 and the gating charges. The fact that the parallel cation–π effect was not observed with the wild-type Phe was really intriguing. Because the Phe233Cha mutant produced a lower V_m than the wild type (Figure A3.4), it is clear that the voltage sensor does not need an aromatic side chain at the position 233 to function. The wild-type Phe side chain can perhaps interact with the gating charges through a different type of interaction other than the cation–π.

In summary, we found that a rigid cyclic side chain at the position of Phe233 is crucial for the channel gating while aromaticity is not required. The F233W displayed a substantial increase in voltage sensitivity. This observation is consistent with the model proposed by another group, in which the tryptophan

side chain at this position enhances the favorable interaction to the gating charges through the cation–π interaction.

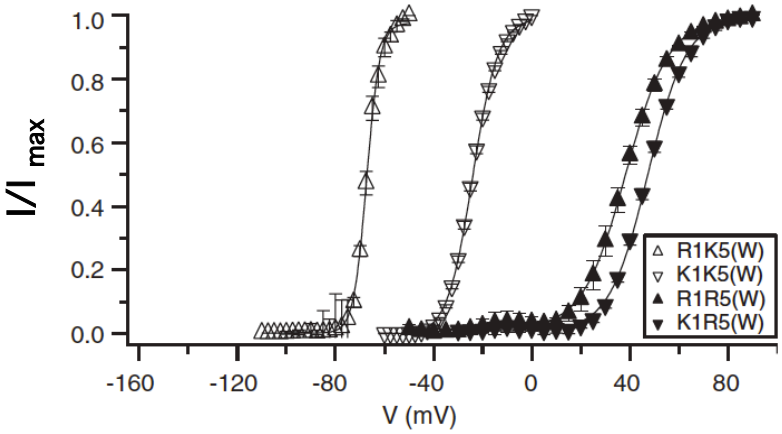

Figure A3.5. Lys at positions 1 and 5 stabilizes the voltage sensor in its closed and open conformation, respectively, in the presence of Trp. The voltage activation curves of R1K5(W), K1K5(W), R1R5(W), and K1R5(W). Fraction of the maximal current (I/I_{max}, means ± s.e.m.) is plotted as a function of the depolarization voltage and fitted with the two-state Boltzmann function. (R1K5(W), $n = 9$; K1K5(W), $n = 11$; R1R5(W), $n = 5$; and K1R5(W), $n = 7$)

A3.3 Materials and Methods

Shaker K⁺ channel expression

The *Shaker* H4 (inactivation removed) construct in a BlueScript vector was used for *Shaker* K^+ channel expression in *Xenopus* oocytes (7). The *N*-type inactivation gate (corresponding to amino acids 6–46) was not included in the construct (8). cRNA was prepared from HindIII linearized plasmid using T7 RNA polymerase (Promega).

Xenopus oocytes were harvested from mature female *Xenopus laevis* and defolliculated by collagenase treatment for 1–2 hours. Oocytes were then rinsed thoroughly and stored in ND96 solution (96 mM NaCl, 2 mM KCl, 1.8 mM $CaCl_2$, 1.0 mM $MgCl_2$, 5 mM HEPES, 50 μg/ml gentamycin, pH 7.6 with NaOH). Defolliculated oocytes were selected 2–4 hours after collagenase treatment and injected with cRNA the next day. The injected oocytes were incubated in ND96 solution before recording. All oocytes were stored in an incubator at 18 °C. Recordings of ionic current measurements were performed 1–2 days post-injection.

Unnatural amino acid incorporation

Unnatural amino acids were incorporated into the *Shaker* K^+ channel using the nonsense-suppression method (*1*). THG73 was used as the amber suppressor tRNA (*15*). The preparations of amino acids coupled to the dinucleotide (dCA) and the ligation of the conjugated dCA-amino acid have been described previously (*16*). Crude tRNA-amino acid product was used without desalting, and the product was confirmed by MALDI-TOF MS on 3-hydroxypicolinic acid (3-HPA) matrix. Deprotection of the NVOC group on tRNA-amino acid was carried out by 10-minute photolysis immediately prior to injection. Equal volumes of the *Shaker* cRNA (in which the codon for Phe was replaced by the amber stop codon) and unprotected tRNA-amino acid were mixed prior to injection. Approximately 15 ng of tRNA was used per oocytes. As a negative control, 76-nucleotide tRNA (dCA ligated to 74-nucleotide tRNA) was co-injected with cRNA in the same manner as fully charged tRNA.

Electrophysiological recordings

All recordings were performed at room temperature in two-electrode voltage-clamp configuration with an oocyte clamp amplifier (OC-725C, Warner Instrument Corp.), Digidata 1440A analog-to-digital converter interfaced with a computer, and pClamp10.1 software (Axon Instruments, Inc.) for controlling membrane voltage and data acquisition. The recorded signal was filtered at 1 kHz and sampled at 10 kHz.

To investigate voltage-dependent channel activation, oocytes were held at −80 mV (*Shaker* wild type and most of the mutants) or −110 mV [F→W, i.e., R1K5(W) mutant] with pulse potential starting from holding potential ending between +30 mV and +180 mV in 10 mV, 5 mV or 2.5 mV increments. The repolarization potentials were either more negative to the voltage at which channel starts to open (for most mutants) or slightly positive to that voltage (for mutants with very fast closure rate). Recording solution contained 98 mM KCl, 0.3 mM $CaCl_2$, 1 mM $MgCl_2$, and 5 mM HEPES pH 7.6.

Data analysis

All statistical fits and figure plotting were done using Clampfit 10.1 (Axon Instruments, Inc.). No leak or capacitive current was subtracted from the current traces of voltage-dependent channel activation. For voltage-dependent channel activation recordings, the amount of current at the repolarization step, typically measured 4–5 ms after the depolarization step when most of the capacitive current has relaxed, was normalized against the maximal current (I/I_{max}) and

plotted as a function of the depolarization voltage (I–V plot). This voltage-dependent activation plot was fitted with the two-state Boltzmann function (Equation 1).

$$I/I_{max} = 1/[1+\exp\{(-ZF/RT)\times(V-V_m)\}] \quad \text{(Eq. 1)}$$

I/I_{max} is the fraction of the maximal current. V is the depolarization voltage to open the channels. V_m is the voltage at which the channels have reached 50% of their maximal current. F is the Faraday's constant. R is the gas constant. T is the absolute temperature, and Z is the apparent valence of voltage dependence. Note that I/I_{max} does not represent the true open probability (P_o) of the channel, given that the maximum P_o of *Shaker* wild-type channel in whole oocytes is less than 1.0 (*17*).

A3.4 References

(1) Jiang, Y.; Ruta, V.; Chen, J.; Lee, A.; Mackinnon, R. The principle of gating charge movement in a voltage-dependent K^+ channel. *Nature* **2003**, *423*, 42–48.

(2) Long, S. B.; Campbell, E. B.; Mackinnon, R. Crystal structure of a mammalian voltage-dependent Shaker family K^+ channel. *Science* **2005**, *309*, 897–903.

(3) Long, S. B.; Campbell, E. B.; Mackinnon, R. Voltage sensor of Kv1.2: structural basis of electromechanical coupling. *Science* **2005**, *309*, 903–908.

(4) Long, S. B.; Tao, X.; Campbell, E. B.; Mackinnon, R. Atomic structure of a voltage-dependent K^+ channel in a lipid membrane-like environment. *Nature* **2007**, *450*, 376.

(5) Aggarwal, S. K.; MacKinnon, R. Contribution of the S4 segment to gating charge in the Shaker K^+ channel. *Neuron* **1996**, *16*, 1169–1177.

(6) Seoh, S. A.; Sigg, D.; Papazian, D. M.; Bezanilla, F. Voltage-sensing residues in the S2 and S4 segments of the Shaker K^+ channel. *Neuron* **1996**, *16*, 1159–1167.

(7) Ramsey, I. S.; Moran, M. M.; Chong, J. A.; Clapham, D. E. A voltage-gated proton-selective channel lacking the pore domain. *Nature* **2006**, *440*, 1213–1216.

(8) Mecozzi, S.; West, A. P., Jr; Dougherty, D. A. Cation–π interactions in simple aromatics: electrostatics provide a predictive tool. *J. Am. Chem. Soc.* **1996**, *118*, 2307–2308.

(9) Mecozzi, S.; West, A. P.; Dougherty, D. A. Cation–π interactions in aromatics of biological and medicinal interest: electrostatic potential surfaces as a useful qualitative guide. *Proc. Natl. Acad. Sci. U.S.A.* **1996**, *93*, 10566–10571.

(10) Sasaki, M.; Takagi, M.; Okamura, Y. A voltage sensor-domain protein is a voltage-gated proton channel. *Science* **2006**, *312*, 589–592.

(11) Schoppa, N. E.; Sigworth, F. J. Activation of Shaker potassium channels. III. An activation gating model for wild-type and V2 mutant channels. *J. Gen. Physiol.* **1998**, *111*, 313–342.

(12) Islas, L. D.; Sigworth, F. J. Voltage sensitivity and gating charge in Shaker and Shab family potassium channels. *J. Gen. Physiol.* **1999**, *114*, 723–742.

(13) Zagotta, W. N.; Hoshi, T.; Aldrich, R. W. Shaker potassium channel gating. III: Evaluation of kinetic models for activation. *J. Gen. Physiol.* **1994**, *103*, 321–362.

(14) Pless, S. A.; Galpin, J. D.; Niciforovic, A. P.; Ahern, C. A. Contributions of counter-charge in a potassium channel voltage-sensor domain. *Nat. Chem. Biol.* **2011**, *7*, 617–623.

(15) Saks, M. E.; Sampson, J. R.; Nowak, M. W.; Kearney, P. C.; Du, F.; Abelson, J. N.; Lester, H. A.; Dougherty, D. A. An engineered Tetrahymena tRNAGln for in vivo incorporation of unnatural amino acids into proteins by nonsense suppression. *J. Biol. Chem.* **1996**, *271*, 23169–23175.

(16) Nowak, M. W.; Gallivan, J. P.; Silverman, S. K.; Labarca, C. G.; Dougherty, D. A.; Lester, H. A. In vivo incorporation of unnatural amino acids into ion channels in Xenopus oocyte expression system. *Methods Enzymol.* **1998**, *293*, 504–529.

(17) Schmidt, D.; Mackinnon, R. Voltage-dependent K^+ channel gating and voltage sensor toxin sensitivity depend on the mechanical state of the lipid membrane. *Proc. Natl. Acad. Sci. U.S.A.* **2008**, *105*, 19276–19281.

Appendix 4

Site-Specific Unnatural Amino Acid Incorporation of Small-Molecule Donor and Acceptor Fluorophores for Single-Receptor FRET Measurement

A4.1 Introduction

Efforts to probe the structure and function of proteins by site-specific incorporation of fluorescent amino acids via unnatural amino acid mutagenesis have been made for over a decade (*1*). Previously, the Dougherty lab and the Lester lab have also incorporated the unnatural amino acid lysine-BODIPY-FL into the muscle-type nAChR in *Xenopus* oocytes via the nonsense-suppression methodology (*2*). These ion channels were visualized at the single-receptor level using total internal reflection fluorescence microscopy (TIRFM). In this project, we aimed to extend this approach by incorporating two unnatural amino acids into one assembled receptor. We hoped to observe Förster resonance energy transfer (FRET) within the same receptor and ultimately apply this method for studying ion channel function.

A4.2 Key Progress

We selected BODIPY-FL and BODIPY-558/560 as the FRET donor and FRET acceptor, respectively. BODIPY dyes have an advantage over other fluorophores because of their small size and hydrophobicity, which are favored for unnatural amino acid incorporation via the nonsense-suppression method. Energy transfer between these two BODIPY fluorophores has previously been demonstrated for protein in solution (*3*). Their fluorescent properties, as reported on the Life Technologies™ website, are shown in Table A4.1.

Table A4.1. Fluorescent Properties of BODIPY[1]

FRET Pair	Donor: BODIPY-FL	Acceptor: BODIPY558/560
λ_{max}	502–505 nm	558 nm
Emission wavelength	510–511 nm	568 nm
ε	82000–91000 $cm^{-1}M^{-1}$	97000 $cm^{-1}M^{-1}$
	R_0 = 59.6 Å	

Revised scheme for dCA-LysBODIPY synthesis

Unlike the previously described procedure, in which BODIPY *N*-succinimidyl ester was coupled to the (NVOC)lysine-cyanomethyl ester prior to the final dCA coupling reaction, we first linked the N^{ε}-protected (NVOC)lysine-cyanomethyl ester to the dCA before the dCA-(NVOC)lysine was coupled to the BODIPY (Scheme A4.1). The ligation of BODIPY was normally complete within 4 hours, and the final product could be obtained in a higher yield compared to

[1] Molecular Probes® Handbook

the reported protocol. We made dCA-LysBODIPY-564/580 in addition to the FRET pair — dCA-LysBODIPY-FL and dCA-LysBODIPY-558/568.

Scheme A4.1. Synthesis of dCA-LysBODIPY

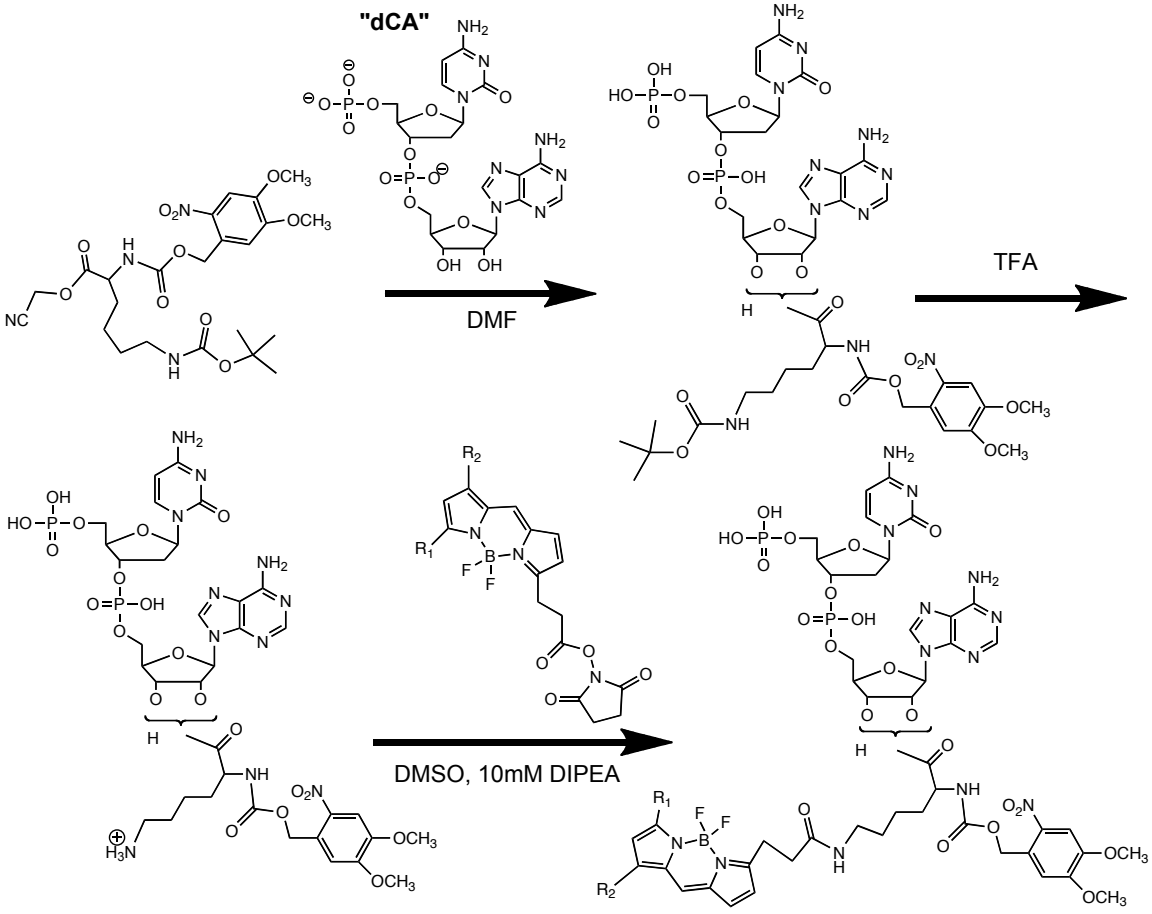

	$-R_1$	$-R_2$
BODIPY-FL	$-CH_3$	$-CH_3$
BODIPY-558/568		-H
BODIPY-564/570	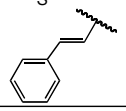	-H

Characterization of dCA-LysBODIPY and tRNA-LysBODIPY

When the fluorescence emission of dCA-coupled Lys(NVOC)BODIPY-564/570 was measured on a fluorometer, we found that the fluorescent signal was completely lost after a 10-minute exposure to the UV on the arc lamp (data not shown). Instability of the styrene on the BODIPY-564/570 was not likely the reason because similar loss of fluorescent signal was later seen for the tRNA-(NVOC)LysBODIPY-558/568 as well. We speculated that the fluorophore was photo-bleached under the UV light, *or* that the deprotection of the NVOC group generated a side product that acted as a quencher to the BODIPY fluorophore. Quenching of a fluorophore in solution is concentration dependent. To see the effect of concentration, after tRNA-Lys(NVOC)BODIPY-558/568 was irradiated with UV light, we made serial dilutions of this tRNA solution as well as the unirradiated sample of tRNA-Lys(NVOC)BODIPY-558/568 as controls. The fluorescence emission was measured on a fluorometer pre- and post-UV exposure. We found that dilution of the tRNA solution did not affect the loss of fluorescent signal (Figure A4.1), which eliminates the possibility that BODIPY was quenched by a byproduct of the NVOC deprotection reaction. Photo-bleaching of the BODIPY fluorophores, therefore, was the underlying reason for the loss of fluorescent signal.

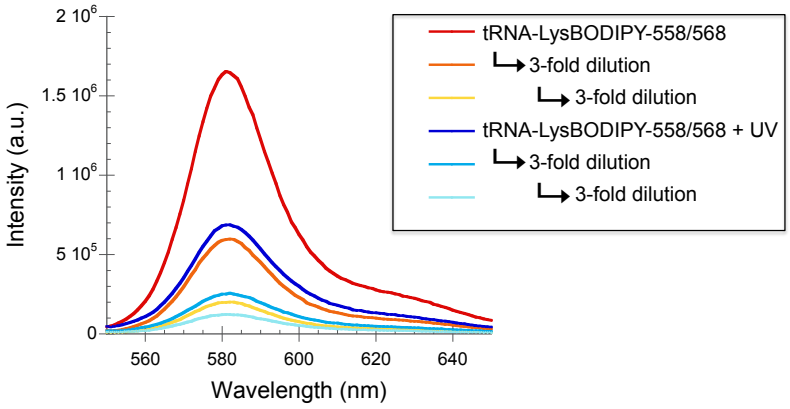

Figure A4.1. Fluorescent emission spectra showing the effect of UV irradiation on (NVOC)LysBODIPY-558/568 ligated to TQAS. A decrease in fluorescence intensity was observed after an exposure to UV light. Serial dilutions of the tRNA solutions show a comparable drop in the fluorescence intensity.

In a model reaction, dCA-(NVOC)Lys was deprotected on a UV lamp, and the lifetime of the unprotected dCA-Lys was found to be only ~ 2 hours in solution, as indicated by the results from MALDI MS. Because the NVOC protecting group is needed to keep the unnatural amino acid stable in solution, the photo-bleaching would cause a significant loss in fluorescent signal. We then considered different options other than the NVOC protecting group.

α-Hydroxy lysine, p-amino phenylalanine, and p-amino phenyl hydroxy acid as linkers for BODIPY unnatural amino acid incorporation

4-Pentenoyl (4-PO) is another common protecting group utilized in the nonsense suppression methodology. However, iodine, which is a known quencher for several fluorescent dyes, is needed for removing the 4-PO

protecting group from the unnatural amino acid (prior to oocyte injection), and thus, we were hesitant to co-inject an iodine solution with BODIPY into the oocytes, as imaging BODIPY fluorescence was our goal.

We then considered using a lysine α-hydroxy (LysOH) as a linker instead of lysine, such that a protecting group would not be needed at all. N^{ε}-Boc-*L*-LysOH was synthesized following a published procedure for α-hydroxy acid synthesis (*4*). A TDBMS group was installed on the hydroxy for ease of HPLC purification in a later step (Scheme A4.2).

Surprisingly, we found that tRNA-BODIPY558/568 was not bleached after 5 minutes under UV when we used LysOH as the linker, unlike what was seen with the Lys-NVOC linker (Figure A4.2). The result suggests that the NVOC protecting group was involved in the photo-bleaching of BODIPY558/568 through an unknown mechanism.

Unfortunately, when we tried to incorporate this residue into the muscle-type nAChR, no current was observed above the background. We hypothesized that harsh treatment with TFA to remove the Boc and TDBMS groups may have caused an isomerization at the C^{α} stereocenter, from *L* to *D* amino acid. Treatment with TFA, which is commonly used in peptide synthesis and is compatible with amino acids, has never been used in the synthesis involving an α-hydroxy acid to our knowledge. Since MALDI MS was the only characterization available for dCA-coupled molecules, the characterization did not provide useful information on the stereochemistry of the compound.

Products from model reactions were characterized on a polarimeter, but no reliable result was obtained. Attempts were made to synthesize dCA-LysOH-BODIPY using different protecting groups, but the desired products have never been achieved.

Scheme A4.2. Synthesis of dCA-LysOH-BODIPY

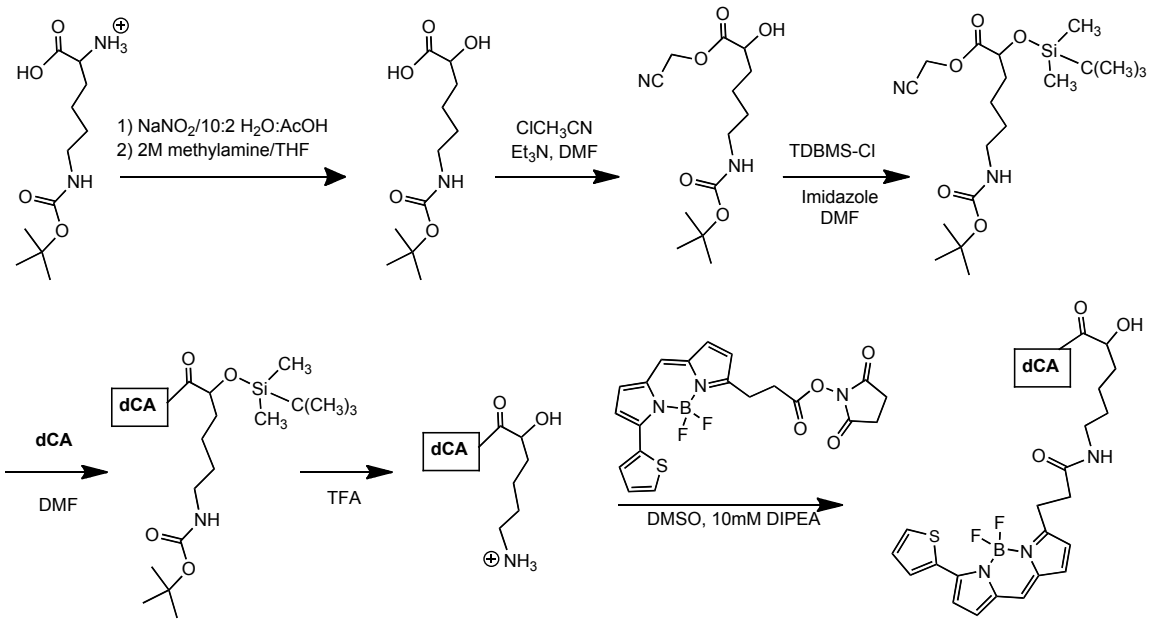

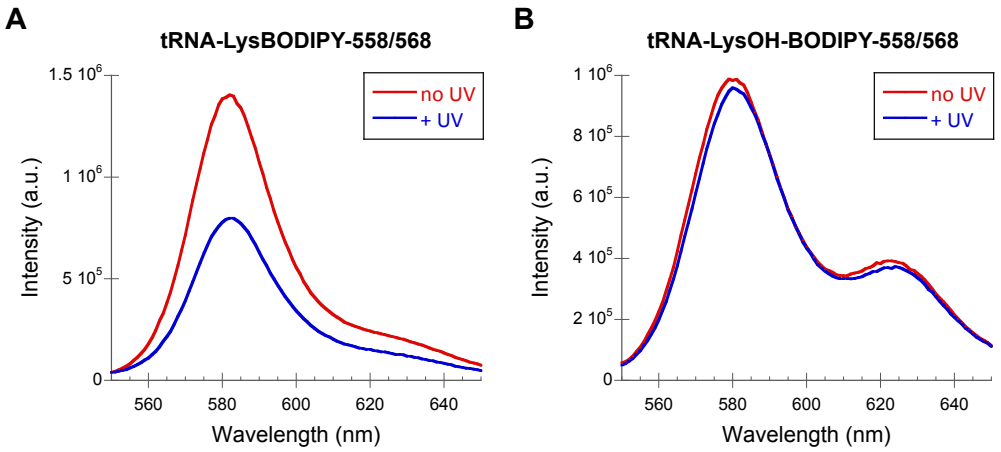

Figure A4.2. Fluorescent emission spectra showing the effect of UV irradiation on BODIPY558/568. **(A)** Fluorescent intensity of LysBODIPY558/568 ligated to TQOpS' was dropped after a 5-minute exposure to UV light. **(B)** UV irradiation did not affect fluorescent emission of LysOH-BODIPY558/568 ligated toTQOpS'.

p-Aminophenylalanine and p-aminophenyllactic acid as linkers for BODIPY unnatural amino acid incorporation

Previous work has utilized *p*-aminophenylalanine and *p*-aminophenyllactic acid to incorporate BODIPY fluorophores into proteins or peptides (*3*, *5*). The α-amino groups of these molecules were unprotected in the reported studies. The aniline group on the phenyl ring has a lower pK_a than the α-amino group, and the pH of the reaction could be tuned such that the amide coupling to the BODIPY succinimidyl ester could theoretically occur almost exclusively at the aniline on the side chain. Thus, we hoped to apply their approach to our system. However, the amide coupling between BODIPY succinimidyl ester and the aniline moiety on the phenyl side chain did not proceed to yield any product (Scheme A4.3), presumably due to a weaker

nucleophilicity of the aniline compared to the amine on the lysine side chain. Several conditions were tested, including different bases, pH, and temperatures.

Scheme A4.3. No reactivity between the side-chain aniline of *p*-aminophenylalanine or *p*-aminophenyllactic acid with the BODIPY558/568 succinimidyl ester

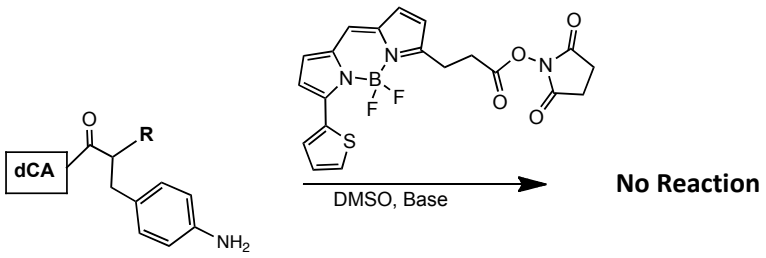

$R = \overset{\oplus}{N}H_3$ *p*-amino phenylalanine

R = OH *p*-amino phenyllactic acid

Optimized NVOC deprotection condition

We finally decided to continue using lysine as the linker for incorporating BODIPY into a receptor via unnatural amino acid mutagenesis. NVOC deprotection condition needed optimization to minimize the loss of LysBODIPY fluorescent signal by photo-bleaching on the UV lamp.

dCA-coupled to Lys(NVOC)Biocytin was used as a model compound for optimizing NVOC deprotection conditions on the UV lamp. UV deprotection was performed on 1 μL of 0.05 mM of dCA-Lys(NVOC)Biocytin for 1–6 minutes at room temperature, and the resulting solutions were characterized by MALDI

MS. (1 μg/μL of tRNA-coupled unnatural amino acid was estimated to be ~ 0.04 mM.) Although mass spectroscopy is not quantitative, we did observe a smaller peak for the NVOC-containing compound and larger peak for the unprotected compound upon increasing UV irradiation time. Resulting spectra from 4-minute and 5-minute deprotection reactions showed similar ratio between the starting material and the product peaks, and so we conclude that 4-minute irradiation is sufficient for the NVOC deprotection.

Incorporation of donor and acceptor BODIPY fluorophores into nAChR

One of the major challenges in this project was the incorporation of two unnatural amino acids with bulky side chains into the same protein using two different suppressor tRNAs recognizing two different stop codons. Herein, we aimed to simultaneously express the LysBODIPY FRET donor and acceptor in the muscle-type nAChR. Because permissive sites were needed to incorporate unnatural amino acids with bulky side chains, we tested the α70 residue where biocytin had previously been incorporated (*6*), as well as the equivalent positions on the β, γ, and δ subunits. (We referred to these sites using α-numbering, e.g. β70, γ70, and δ70). Single LysBODIPY incorporation at any of these positions produced large current, although the reacylation background was also high, especially with THG73 as the suppressor tRNA. Using the TQAS and TQOpS' suppressor tRNA, the current obtained from LysBODIPY suppression was clearly higher than the background signal. We also incorporated these BODIPY-

containing unnatural amino acids at position 71 in all individual subunits, but smaller current was observed compared to the mutation at the position 70.

Sufficient protein expression (producing currents of 500 nA – 1 μA in two-electrode voltage-clamp mode) was achieved when the donor was incorporated at the β70 position by amber suppression with TQAS and the acceptor at the γ70 position by opal suppression with TQOpS'. (500 nA of muscle-nAChR current is ideal for TIRF imaging on oocytes.) Slightly smaller current was observed when we moved the acceptor to the δ70 position. The distances between the adjacent subunits, i.e., β–δ, is ~ 30 Å, and between non-adjacent subunits, i.e., β–γ, is ~ 55 Å, based on the electron microscopy structure of *Torpedo* nAChR (Protein Data Bank code 2BG9).

Preliminary TIRF Image

Figure A4.3 shows a single-receptor TIRF image of nAChR labeled with LysBODIPY-564/570. Another member of the lab successfully imaged nAChR labeled with either LysBODIPY-FL or LysBODIPY-558/568. However, simultaneous TIRF imaging of two BODIPY fluorophores on oocytes has not been possible at the single-receptor level. Both TIRF imaging and the FRET measurement of these BODIPY unnatural amino acids are still ongoing in the lab.

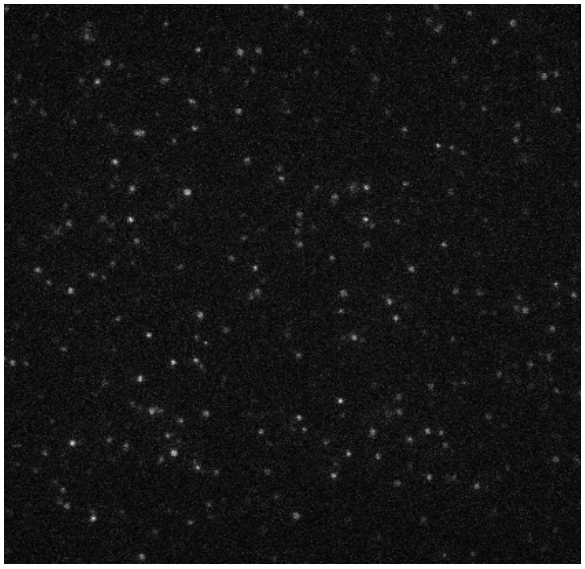

Figure A4.3. A single-receptor TIRF image of an oocyte expressing muscle-type nAChR labeled with LysBODIPY-564/570 at position α70 through unnatural amino acid incorporation

A4.4 Materials and Methods

A general procedure for deprotection of Boc group from Boc-protected dCA-(NVOC)lysine and dCA-LysOH

An ampoule of neat TFA (Aldrich) was added to the powder of dCA-*N*ε-Boc-(NVOC)Lysine or dCA-*N*ε-Boc-(TDBMS)LysOH in a small flask, and the solution was mixed until all solid was dissolved. After 5–10 minutes, TFA was removed *in vacuo* till dryness. The crude product was redissolved in ethanol, and the solvent was removed on a rotary evaporator to get rid of trace TFA. Then diethyl ether was added to the dry solid, which was insoluble in either. The mixture was sonicated briefly, and the white precipitate was collected on a

syringe filter unit (Acrodisc® CR 25 mm, 0.45 μm). Approximately 3 mL of ether was passed through the wheel filter at least twice, and the filter was dried by pushing air through 5 times. The product was eluted with 1:1 acetic acid:acetonitrile (~ 9 mL). Further purification was not required. This compound generally had poor retention on HPLC. Solvents were removed on a lyophilizer resulting in dry powdery solid of dCA-(NVOC)Lys and dCA-LysOH.

General procedure for coupling of BODIPY to dCA-(NVOC)Lys and dCA-LysOH

BODIPY-FL C_3 succinimidyl ester, BODIPY 558/568 C_3 succinimidyl ester, and BODIPY 564/570 C_3 succinimidyl ester were purchased from Life Technologies Corporation (Molecular Probes®).

~ 1.5 mg of BODIPY succinimidyl ester was added to a vial containing the powder of dCA-(NVOC)Lys or dCA-LysOH and a stir bar. The vial was purged with argon 3–5 times. In a separate vial, also dried under argon, 10 μL of *N*,*N*-diisopropylethylamine (DIPEA, Aldrich) was injected into ~ 4 mL of DMSO anhydrous (Aldrich), and 300 μL of this solution was transferred to the vial containing the dCA-lysine and the BODIPY. The reaction was stirred at room temperature under argon and protected from light. A color change was normally observed after 5–10 minutes (e.g., neon pink to deep purple for BODIPY 558/568 and bright orange to bright green for BODIPY-FL). The reaction was monitored by analytical HPLC, and was typically complete within ~ 4 hours. ~ 3 mL of 1:1 water:acetonitrile was added to dilute the reaction before the reaction was purified on a reversed-phase HPLC for 20 minutes at a flow rate

of 20 mL/min. Combined fractions were characterized by MALDI MS. The fractions that contained product were dried on a lyophilizer.

An opened bottle of BODIPY succinimidyl ester was stored under argon at −20 °C in the presence of Drierite® and protected from light.

Coupling dCA-LysBODIPY to tRNA

We used the standard protocol for ligating the dCA-BODIPY onto the tRNA as described in **Chapter 2**, except that ~ 45–60 minute reaction time was needed. The product was purified following the standard procedure and characterized by MALDI MS. A spin column was required to get rid of all the dCA-BODIPY. The reaction was quite inefficient; 74-mer tRNA was normally present. tRNA-BODIPY was quantified by UV-visible spectroscopy based on the absorption peak of the BODIPY fluorophore.

A4.5 References

(1) Turcatti, G.; Nemeth, K.; Edgerton, M. D.; Meseth, U.; Talabot, F.; Peitsch, M.; Knowles, J.; Vogel, H.; Chollet, A. Probing the structure and function of the tachykinin neurokinin-2 receptor through biosynthetic incorporation of fluorescent amino acids at specific sites. *J. Biol. Chem.* **1996**, *271*, 19991–19998.

(2) Pantoja, R.; Rodriguez, E. A.; Dibas, M. I.; Dougherty, D. A.; Lester, H. A. Single-molecule imaging of a fluorescent unnatural amino acid incorporated into nicotinic receptors. *Biophys. J.* **2009**, *96*, 226–237.

(3) Kajihara, D.; Abe, R.; Iijima, I.; Komiyama, C.; Sisido, M.; Hohsaka, T. FRET analysis of protein conformational change through position-specific incorporation of fluorescent amino acids. *Nat. Methods* **2006**, *3*, 923–929.

(4) Deechongkit, S.; You, S.; Kelly, J. Synthesis of all nineteen appropriately protected chiral α-hydroxy acid equivalents of the α-amino acids for Boc solid-phase depsi-peptide synthesis. *Org. Lett.* **2004**, *6*, 497–500.

(5) Watanabe, T.; Miyata, Y.; Abe, R.; Muranaka, N.; Hohsaka, T. N-Terminal specific fluorescence labeling of proteins through incorporation of fluorescent hydroxy acid and subsequent ester cleavage. *ChemBioChem* **2008**, *9*, 1235–1242.

(6) Gallivan, J.; Lester, H.; Dougherty, D. Site-specific incorporation of biotinylated amino acids to identify surface-exposed residues in integral membrane proteins. *Chem. Biol.* **1997**.

Appendix 5

Interaction Between Nicotinic Acetylcholine Receptors and the Modulator Protein Lynx1[1]

A5.1 Introduction

Nicotinic acetylcholine receptors (nAChRs) are ligand-gated ion channels expressed throughout the brain and at neuromuscular junctions. These receptors are homo- or hetero-pentameric with homologous subunits arranged around a central ion pore (*1*). Members of the lynx family of proteins have been shown to physically associate with nAChRs and are expressed in brain areas heavily involved in nicotinic function (*2*). Lynx modulators are thought to support proper nAChR function *in vivo* (*3*).

Lynx1, the first protein discovered of the family, is a small protein containing 72 amino acids with a *C*-terminal glycophosphoinositide-linked (GPI-linked) sequence (*4*). Lynx's cysteine-rich motif is characteristic of the class of elapid snake venom neurotoxins such as α-bungarotoxin (αBtx) and cobratoxin, which are known competitive antagonists of specific nAChR subtypes (*5*). The GPI-linked motif would topologically allow the lynx proteins to bind in a similar

[1] This work was done in collaboration with Dr. Julie M. Miwa and Professor Henry A. Lester.

fashion to αBtx at the intersubunit interface on nAChRs (*6*). However, the antagonistic effect, as seen with the toxins, has not been demonstrated with lynx binding. This raises the possibility that lynx binds to the non-agonist interfaces of the receptor that are allosterically important to gating (*7*).

We aim to determine whether or not lynx1 binds to nAChR at the agonist-binding interfaces (as αBtx does) and to identify the number of lynx1 binding sites per receptor. Once the broad regions of the binding site are located, we hope to focus further on specific binding residues using site-directed mutagenesis.

A5.2 Progress

Western blot analysis of separate membranes from *Xenopus* oocytes injected with lynx1 with an *N*-terminal HA tag showed that lynx1 was expressed on the membrane on the oocytes. There is no direct readout on the expression level or the function of lynx1, which makes this project very challenging. Many different constructs of both lynx1 and α4β2 nAChR were tested. Both pDH and pGEMhe were used as expression vectors for lynx1. The expression efficiency of the pGEMhe was presumed to be significantly higher than the pDH. We experimented with rat wild-type α4β2, rat α4(L9′A)β2, and chick wild-type α4β2 at numerous α4:β2 mRNA ratios in conditions with and without calcium ions, with and without atropine. Results from electrophysiological experiments indicated that lynx1 did not significantly affect the function of the α1β1γδ

(muscle-type) or the α7 (neuronal) nAChRs, while it affected the stoichiometry of the α4β2 neuronal subtypes, as indicated by ACh dose-response curves. However, oocytes expressing α4β2 and lynx1 showed α4β2 stoichiometry preferences similar to those of oocytes expressing α4β2 and a control peptide — 72 random amino acids with a *C*-terminal GPI-signal sequence.

A5.3 Future Direction

Due to the small size of the lynx protein, it is possible that too much lynx1 mRNA was injected into oocytes, overwhelming the translation machinery in a non-specific manner. This could explain the similar effect observed between lynx1 and the control protein on the α4β2 stoichiometry preferences. One could possibly experiment with 10-100 fold less mRNA. It would definitely be wise to probe for the lynx-binding site on nAChRs (or other Cys-loop receptors) with a fixed stoichiometry.

A5.4 Methods

The molecular biology and electrophysiology protocols used in these studies can be found in **Chapter 2**.

A5.5 References

(1) Unwin, N. Refined structure of the nicotinic acetylcholine receptor at 4Å resolution. *J. Mol. Biol.* **2005**, *346*, 967–989.

(2) Ibañez-Tallon, I.; Miwa, J.; Wang, H.; Adams, N. Novel modulation of neuronal nicotinic acetylcholine receptors by association with the endogenous prototoxin lynx1. *Neuron* **2002**.

(3) Miwa, J.; Stevens, T.; King, S.; Caldarone, B.; Ibanez-Tallon, I.; Xiao, C.; Fitzsimonds, R. M.; Pavlides, C.; Lester, H. A.; Picciotto, M. R.; Heintz, N., I. The prototoxin lynx1 acts on nicotinic acetylcholine receptors to balance neuronal activity and survival in vivo. *Neuron* **2006**.

(4) Sali, A.; Role, L.; Heintz, N. lynx1, an endogenous toxin-like modulator of nicotinic acetylcholine receptors in the mammalian CNS. *Neuron* **1999**.

(5) Lyukmanova, E.; Shenkarev, Z.; Shulepko, M.; Mineev, K.; D'hoedt, D.; Kasheverov, I.; Filkin, S.; Krivolapova, A.; Janickova, H.; Dolezal, V. NMR Structure and Action on Nicotinic Acetylcholine Receptors of Water-soluble Domain of Human LYNX1. *J. Biol. Chem.* **2011**.

(6) Ibañez-Tallon, I.; Wen, H.; Miwa, J. M.; Xing, J.; Tekinay, A. B.; Ono, F.; Brehm, P.; Heintz, N. Tethering naturally occurring peptide toxins for cell-autonomous modulation of ion channels and receptors in vivo. *Neuron* **2004**, *43*, 305–311.

(7) Hansen, S. B.; Taylor, P. Galanthamine and non-competitive inhibitor binding to ACh-binding protein: evidence for a binding site on non-alpha-subunit interfaces of heteromeric neuronal nicotinic receptors. *J. Mol. Biol.* **2007**, *369*, 895–901.